EVOLUTION OF MAGMATIC VOLATILES DURING DRILLING INTO A MAGMA BODY, KRAFLA ICELAND

A thesis submitted in partial fulfilment of the requirements for the

Degree

of Master of Science in Geology

in the University of Canterbury

by

Tamiko Watson

2018

Acknowledgements

First and foremost, I would like to thank my primary supervisor, Alex Nichols. I have learned so much from you, both about science and how to be a scientist, and I am lucky to have had your support and guidance along the way.

I would also like to thank my other supervisor Ben Kennedy for your support and giving me an opportunity to take on this project.

I would also like to thank Ian Schipper for you time and help at the Australian Synchrotron and allowing me to use the EPMA .

A special thanks to Mark Tobin, Pimm Vongsvivut and the rest of the staff at the Australian Synchrotron for their help at the IR-beamline at the Australian Synchrtron. The Australian Synchrotron and the New Zealand Synchrotron Group for granting beamtime and travel funds. [1 SEP]

I would also acknowledge Mason fund for providing funds to go to Wellington. I would also like to thank my friend Lars for allowing me to stay while I was in Wellington (Sorry for kicking you out of your bed for a week!)

Special thanks to Rob and Paul for a quick crash course on rock polishing!

A very special thanks to my flat mates, Sam and Jack, Sorry for not cleaning my dishes for the month of my thesis!!

Lastly, I must express my very profound gratitude to my dad for providing me with continuous encouragement and financial support throughout my years of study.

Abstract

In 2009, the Iceland Deep Drilling Project IDDP-1 borehole unexpectedly intercepted a silicic magma body beneath Krafla volcano at a depth of approximately 2.1 km. Glass samples quenched in the drilling mud were directly sampled at ~15 minute intervals during drill circulation following magma interception at 15:17, providing a unique record of the changing state of the magmatic system over this period. The nature of the glass cuttings varied through time, with a decrease in the proportion of vesicular cuttings and an increase in dense glassy cuttings. The recovered glass cuttings provide a unique opportunity to investigate the magmatic response to a sudden decompression event, and in particular the response of magmatic volatiles over time. During decompression, volatiles diffuse through the magma and exsolve into growing bubbles. Conversely, pressure increases or temperature decreases can cause volatile species to diffuse back from bubbles into the surrounding melt. These processes create distinct diffusion gradients in magmatic glass surrounding the bubbles, and hence the time-dependent volatile response to magmatic decompression is uniquely preserved by the quenched IDDP-1 fragments.

For this project an Electron Probe Micro-anaylser was used to determine the major element compositions of each sample, while Fourier transform infrared spectroscopy (FTIR) was used to generate maps of H_2O and CO_2 absorbance across broad areas. Average H_2O and CO_2 concentrations determined from the volatile maps are used to reconstruct the time-dependent evolution of magmatic H_2O and CO_2 at the magma interface. In addition, transects around bubbles were extracted to examine whether H_2O and/or CO_2 diffusion profiles developed, and if so how they responded with time.

Results from the major element analyses suggest that the clear glass represents the boundary layer between the magma body and it's surrounding rock, some of which appears to have been assimilated at the magma-rock interface. The brown

glass cuttings (Melt-1b) appear to more closely represent the main magma body. Volatile results show that the concentration of total H_2O did not change over time; however, OH/H_2O_m and CO_2 both increase over time after initial intersection. These results are consistent with an increase in temperature that is interpreted to reflect deeper hotter magma rising into the borehole. The volatile distributions around bubbles show both resorption and bubble growth characteristics. This differs from an expected simple decompression (i.e. producing bubble growth) and suggests that the magma maintained a somewhat heterogeneous condition prior to quenching. This may reflect the relatively small borehole size, and together with the fact that no eruption was triggered suggests that very small decompression events can be moderated by melt immediately surrounding the region of low pressure.

Table of Contents

List of Figures

Chapter 2: Geothermal drilling and Krafla, Iceland

Chapter 3: H_2O, CO_2 and silicate melts

Chapter 4: Analytical methods and data production

Chapter 5: Glass composition and volatile distribution

Chapter 6: Implications from the magmatic volatile evolution

Appendix 2: Volatile distribution transects

List of Tables

Details of Personal Communications (pers. Comm.)

Elodie Saubin – provided information on time of glass recovery in other studies

Department of geological sciences
University of Canterbury
PO Box 4800
Christchurch 8140
New Zealand

Rebecca Joyce - provided additional FTIR data of the IDDP-1 glass cuttings

Department of geological sciences
University of Canterbury
PO Box 4800
Christchurch 8140
New Zealand

Chapter 1: Introduction

1.1 Project background

In 2009, the Iceland Deep Drilling Project (IDDP-1) borehole unexpectedly intersected a silicic (76.5 % SiO_2) magma body at a depth of 2104 m below the surface (Elders et al. 2011; Zierenberg et al. 2013; Trewick et al. 2016). When IDDP-1 drilled into the magma body there was no eruption, although magma did apparently rise up the borehole. The lack of eruptions provides research opportunities for future geothermal energy development (Fridleifsson & Elders, 2014) and raise the possibility of drilling directly into magma bodies to efficiently generate cheap geothermal energy. However, engineering, safety and geological studies need to be fully explored. During the drilling the magma was sampled directly as glass fragments that quenched in the drilling mud. These were collected at regular intervals over the time that the magma was being drilled into. These time-series samples have now been made available for further study.

For this project, the evolution of magmatic volatiles (H_2O and CO_2) concentration over time have been measured and the volatile concentration around bubbles in the volcanic fragments have also been mapped. With addition of major element glass chemistry, the quench temperature, H_2O-CO_2 saturation pressure and viscosity over time of the Krafla glass cuttings were calculated. The results from this project will help understand how rhyolitic magmas evolve in response to a sudden change in pressure. Volatile contents were calculated using synchrotron radiation Fourier-transform infrared spectroscopy (SR-FTIR) and Focal plane array detectors Fourier-transform infrared spectroscopy (FPA-FTIR), from the glass that quenched in the IDDP-1 borehole. Volatile distributions around bubbles in the quenched magma were mapped by SR-FTIR thereby allowing the H_2O and CO_2 species distribution around bubbles over a time-series to be quantified at a high spatial resolution and their evolution to be assessed.

1.2 Project objectives

The main goals for this project were to understand how the magma responded to the sudden change of pressure and understand why IDDP-1 borehole at Krafla did not erupt. To reach these goals the following objectives were set out:

1. Determine any changes in magmatic volatile concentration through time.
2. Map the distribution of H_2O species and CO_2 around bubbles in the samples from the time-series set of samples collected during drilling into the Krafla magma body.
3. Determine the magmatic degassing history of the Krafla magma body in response to a sudden loss of pressure as a result of intersection by the drilling.
4. Use the degassing history to make implications on quench timing and viscosity.
5. Investigate the implications of why the Krafla magma did not erupt while it was being drilled.

1.3 Thesis format

The thesis is organised as follows:

Chapter 2 provides a detailed background on the geological setting, the IDDP-1 drilling project and the recovered glass cuttings. Previous studies on these glass cuttings will also be discussed.

Chapter 3 provides a detailed background on the behaviour of H_2O and CO_2 in silicate melts that are required to interpret the results, including H_2O and CO_2 solubilities and diffusivities and the transition between silicate melt and glass.

Chapter 4 presents the details on of sample preparation and analytical methodologies, including discussion of errors and limitations.

Chapter 5 presents the results from synchrotron radiation Fourier-transfrom infrared spectroscopy (SR-FTIR) and electron probe microanlysis (EPMA).

Chapter 6 discusses the results and interprets the evolution of magmatic volatiles in the intersected magma body over the time the samples were collected, why no eruption occurred during decompression. A framework for future investigation will also be presented in this chapter.

Chapter 7 concludes a summary of the findings of the thesis.

Chapter 2: Geothermal drilling and Krafla, Iceland

2.1 Introduction

This chapter provides background on geothermal drilling and an insight into the IDDP-1 drilling at Krafla central volcano. It is important to concisely summarise the components and process of drilling to interpret the effect of drilling on the H_2O and CO_2 content of the magma. Details of the IDDP-1 drilling project and the events leading to the magma drilling are also presented in this chapter. Insight into the chemistry and glass water content of the obsidian chips recovered during drilling will also be presented in this chapter.

2.2 Geothermal drilling

Drilling is the most important and expensive part of geothermal exploration, development, and utilisation (Huenges 2010, Glassley 2015). The aim for geothermal drilling is to access the target reservoir in a safe and cost effective way. Drilling involves exerting forces on the rock to be drilled using a multi-toothed drill bit. Rotary drilling is the standard method used in geothermal exploration, in which a string of drill pipe is hung from a derrick and turned by a motor (DiPippo 2008).

2.2.1 Drilling equipment and techniques

2.2.1.1 Drillstrings

The drillstring consist of the bottomhole assembly and the drillpipe. The drill-string serves several general purposes, including:

- Feeding drilling fluid to the drill bit.
- Imparting rotary motion to the drill bit.

- Providing and allowing down force to be set on the bit.
- Lowering and raising the bit.

2.2.1.2 Bottom hole assembly (BHA)

The bottomhole assembly is the lower portion of the drill-string, consisting of the following:

- The drills bits that are used to excavate the rock/formation.
- Rollercorne bits which are used to crush rocks. These consist of three conical rollers, which are equipped with either steel teeth or with special inserts made of tungsten carbide.
- Drill collars (DC) are thick-walled pipes which generate the "weight on bit" (WOB) to assure the drill bit can drill into the formation.
- Jar, a device that produces high kinetic shock energy onto a stuck drill-string section below the jar.
- Shock sub, designed to dampen axial vibrations of the drill-string induced by the drill bit.
- Heavy weight drillpipe (HWDP) is an "intermediate" between the heavy DC and the drillpipe.
- Mud motor, which is a positive displacement drilling motor which uses hydraulic forces of the drilling fluid to drive the drill bit.

2.2.1.3 Drilling fluids

The drilling fluid serves many essential drilling functions including:

- Cooling the drill bit.
- Transporting cuttings to the surface.
- Preventing cuttings to settle when circulation has stopped.
- Reduce friction between the drill-string and borehole wall.
- Stabilisation of the borehole wall.
- Exertion of hydraulic pressure to prevent gas or fluids from entering the borehole.

- Transport information in the formation of gases, cuttings and fluid, drilled to the surface.

The exact nature of the drill fluid is designed to preform specific tasks. Clay particles are blended into a solution to achieve desired properties (DiPippo 2008). A drilling fluid is pumped down the centre of the drill pipe to the bit and passes through nozzles that accelerate and direct it onto the rock beneath the bit. The drilling fluid captures rock fragments formed by the drill bit and transports them to the surface, through the annulus between the well wall and the drill string (Huenges 2010). When the drilling fluid, which includes rock fragments reaches the surface, it flows over a screen and shaker to separate the rock fragments for examination. The drilling fluid is then returned to the bottom by a mud pump where the cycle is repeated.

2.2.1.4 Casing and cementation

Casing strings are used to secure the walls of drilled hole and isolate fresh water zones to prevent contamination of groundwater during drilling. Fig 2.1 shows a standard method of cement casings. When the hole has been dug to a desired depth the casing is lowered into the hole (Fig 2.1a). A cement mix is then forced down between the inside of the hole and the outside of the casing with a plug, using the drilling fluid (Fig 2.1b). Direct displacement of the cement should lead to the complete filling of the annulus with cement by the time the plug comes to rest on the float collar (Fig 2.1c). Cementing the casing is successful when the excess cement returns to the surface.

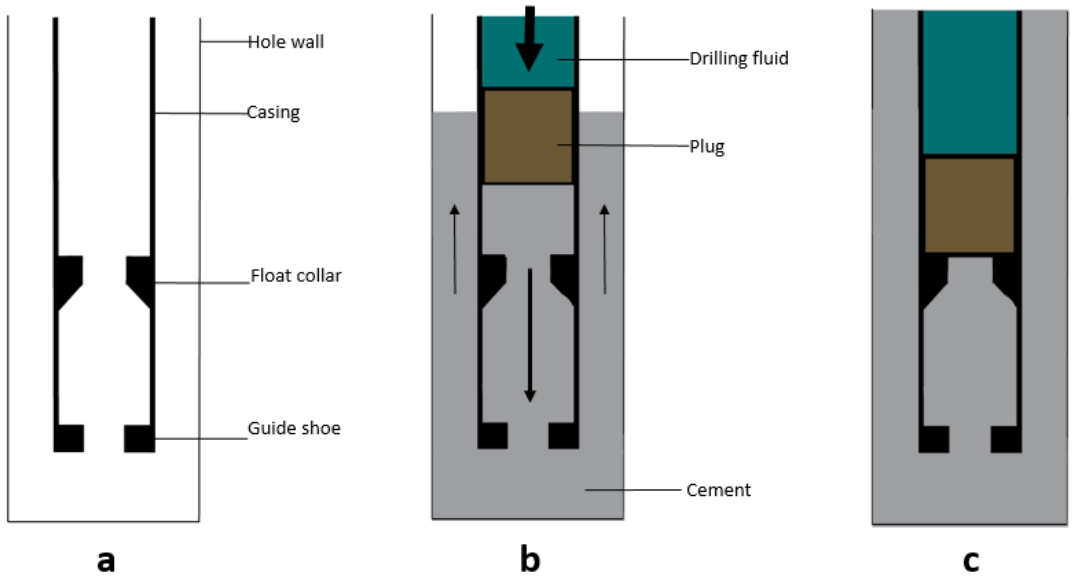

Figure 2.1: Schematic diagram of cementing casing pipes.

2.2.2 Technical risk

2.2.2.1 Loss of circulation

The most common drilling problem in geothermal wells is loss of circulation which occurs when a bit encounters a highly permeable zone. The drilling fluid may be absorbed by the formation and therefore not return to the surface (Huenges 2010). "Total loss" is when the loss is great enough to prevent any return. Loss of circulation is desirable when the well is in the production zone as it indicates that the formation has high permeability (Glassley 2015). However, when loss of circulation occurs in shallow zones, it can be an issue as drilling fluids provide well cooling, lubrication, and removal of cuttings. One way to overcome loss of circulation is by pumping down loss circulating material (LCM) pills. LCM pills are made from fibrous, flaky, and granular materials which create a viscous layer onto the porous formation or cracks, enabling drilling fluids to return to the surface (Huenges 2010; Glassley 2015).

2.2.2.2 Blowout prevention

Fluids in geothermal reservoirs can be very hot and under high pressure. To prevent the unintentional and rapid release of such fluids, blowout prevention

(BOP) equipment is installed. BOPs are a set of fast-acting ram-type valves attached to the surface casing that can be used to release the pressure in the hole.

2.2.2.3 Stuck pipes or tools

Stuck pipes occur when drill strings cannot be pulled out of the hole, however, circulation may still occur (Devereux 2012). Causes of stuck pipes down well can be associated to; 1) the geometry of the borehole, 2) solid particles which restrict or prevent mud circulation, and 3) mud overbalances over permeable formations which induce differential sticking of the drilling apparatus (Devereux, 2012). Stuck drill strings can be released through by either pumping down high viscosity pills for cleaning the borehole or adding friction-reducing additives to reduce friction coefficient. If wall cave-ins and borehole breakouts are the issue, the weight of the drilling fluid is increased to clean out the borehole (Huenges 2010).

2.2.2.4 Fishing

Occasionally a part of the drill-string can break off and be left in the borehole. This lost part is called a “fish” (Huenges 2010, Devereux 2012). The process of retrieving the fish is termed “fishing”.
The main causes for fish occurring in the hole includes;

- Failure somewhere in the drill string caused it to break and drop into the hole.
- A stuck pipe cannot be freed and has to be either cut or unscrewed downhole.
- An object falls into the borehole.

2.2.2.5 Side-tracking

If fishing is unsuccessful, occasionally wells will be side-tracked. Side-tracking is the process of leaving an existing hole at a certain depth and branching off at an angle to form a new hole (Huenges 2010). This can be achieved by forming a cement plug of a certain length at the desired depth in the borehole. After the cement has hardened, a directional drilling assembly is used to side-track the drill string from the cement plug into the borehole wall. When the new hole is drilled, the new well path can be drilled.

2.3 Geological setting, Krafla Iceland

The Krafla central volcano is located on the Northern Iceland Rift Zone (Fig. 2.2). The Krafla geothermal field sits within an 8 km collapsed caldera (Sæmundsson, 1991, Zierenberg et al. 2013). The caldera is bisected by the NNE-SSE fissure swarm that marks the North Iceland Rift Zone. The caldera is largely filled by basaltic lavas and hyaloclastites. Rhyolite has erupted periodically, but intermediate composition lavas are not abundant (Sæmundsson, 1991; Jónasson, 1994).

Extensive drilling for geothermal development in the caldera began in 1974 (Zierenberg et al. 2013). The results of which revealed the extent of several active geothermal activities and subsurface geology (Sæmundsson, 1991; Jónasson, 1994). The drilling showed that near surface postglacial basaltic lavas are underlain by hyaloclastite erupted during the last glacial stage (Guomundsson, 1983). An older sequence of hyaloclastite is overlain and underlain by interglacial lavas down to about 1.2 km, where intrusive rocks begin to dominate. In the deeper regions of the geothermal reservoir doleritic intrusions are abundant, however felsic intrusions were also intersected in several drill holes (Zierenberg et al. 2013). Intrusions generally become more abundant and coarser grained at deeper depths.

The most recent eruptions in the Krafla central volcano were the Krafla Fires; a period of rifting that started with basaltic fissure eruptions in 1975 and continued irregularly until 1984 (Holmgeirsson et al. 2010; Zierenberg et al. 2013). This eruptive sequence consisted of nine volcanic eruptions and ~15 swelling and subsidence events. This volcanic activity affected the geothermal reservoir substantially and limited steam production in existing power plants (Zierenberg et al. 2013).

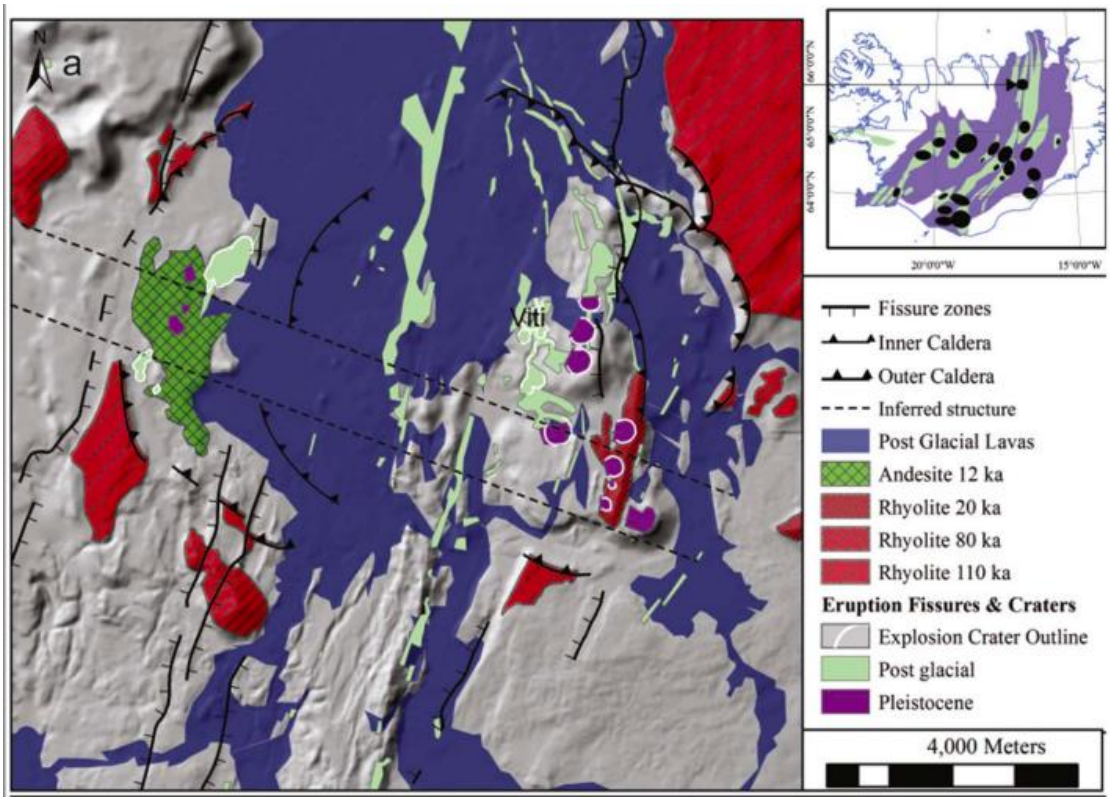

Figure 2.2: Geological map of the Krafla central volcano, highlighting key eruptive material, volcanic and structural features. Figure from Kennedy et al. (2018)

2.4 Boreholes hit magma

2.4.1 Previous magma intersection

Prior to the IDDP-1 drill hole, drilling into magma has occurred on two previous occasions in Hawaii (2005) and in Krafla (2008) (Teplow et al. 2009, Mortensen et al. 2010, Zierenberg et al. 2013).

In 2005, dacite melt was encountered during a routine commercial operations of injection well KJ-13 at Puna Geothermal Venture wellfield, Big Island of Hawaii (Teplow et al. 2009). This was located along a segment of the Kilauea Lower East Rift Zone. At a depth of 2488 m, a dacite melt was intercepted. The melt flowed up the borehole and was repeatedly redrilled over a depth interval of 8 m. Clear vitric glass cutting were recovered to the surface. These cuttings were dacitic and has a silica content of 67 wt%. The intercepted magma is interpreted as an end-stage differentiate of basaltic magma injection into the Kilauea East Rift zone.

Magma was probably first intersected in the Krafla Geothermal system in 2008. The KJ-39 well in the Suourhlioar well field, intercepted magma at 2,571 m depth. Glass retrieved from this event was partially hydrated with silica content ranging from 69.0 to 78.8 wt% (Mortensen et al. 2010, Zierenberg et al. 2013).

2.4.2 IDDP-1 well

The drilling contract for the IDDP-1 well was signed in August 2008 (Holmgeirsson et al. 2010). The IDDP-1 exploration well was designed to drill to completion at 4.5 km depth, where injected water was expected to reach supercritical conditions (Zierenberg et al. 2013). Based on seismic and magnetotelluric surveys, a magma body was inferred to underlie Krafla Caldera at depths of 3-7 km (Einarsson 1978) and the well was designed to intercept the supercritical hydrothermal fluids circulating above it.

The IDDP-1 well and drilling design plan was as follows:

- Surface casing to be drilled to 100 m below the surface. A wellbore rotary drill with a 26” tricone bit with a 36” under-reamer to be used with a drilling fluid of a benotonite mud mixture.
- Intermediate casing I to be emplaced following drilling to 300 m below the surface. Drilling using a wellbore rotary drill with a 23” tricone bit with a benotonite mud mixture as drilling fluid.

- Intermediate casing II to be emplaced upon reaching 800 m below the surface. Drilling with a wellbore rotary with a 23" tricone bit and a drilling fluid of a benotonite mud mixture.
- Anchor casing to be installed on reaching 2400 m below the surface using a wellbore drill with 16-1/2" tricone bits. Drilling fluid to be a bentonite mud mixture as long as it could be sufficiently cooled, if not the drilling fluid would be switched to water.
- Production casing to be drilled to 3500 m below the surface using a wellbore drill with 12-1/4" tricone bits. Drilling fluid to be a bentonite mud mixture as long as it could be sufficiently cooled, if not the drilling fluid would be switched to water.
- Slotted liner to be installed up to 4500 m below the surface, drilled by a wellbore with a 8-1/2" tricone bits. Water to be used as the drilling fluid.

2.4.2.1 Surface casing

The pre-drilling of IDDP-1 began in June 2008. The well was drilled with a 26" tricone pilot and a 36" under reamer (Pálsson et al. 2014). Bentonite-based mud was used as the drilling fluid and the well was drilled to a depth of 87 m below the surface in nine days. At this depth the formation was stable for the casing shoe and it was decided to run the casing (Holmgeirsson et al. 2010, Pálsson et al. 2013).

2.4.2.2 Intermediate casing I (18/Nov/2008 to 24/Nov/2008)

Drilling for the intermediate casing I started on 18 November 2008. Due to the hard formations encountered, drilling progress was slower than expected with a rate of penetration (ROP) of 2.5 m/h. No circulation losses were detected while drilling and the depth of this section was 275 m below the surface.

The well was cased to 260 m below the surface depth due to problems in the wellbore (Holmgeirsson et al. 2010, Pálsson et al. 2014). On 24 November cementing was successful.

2.4.2.3 Intermediate casing II (27/Nov/2008 – 10/Dec/2008)

Drilling for the intermediate II casing continued through 27 November (Holmgeirsson et al. 2010, Pálsson et al. 2014). To keep the hole relatively vertical, drilling progress was slow and the weight on bit (WOB) was kept low. On 8 December, minor drilling fluid losses were detected and healed with LCM at a depth of 788 m below the surface. The well was cased to a depth of 784 m below the surface and the casing was successfully cemented on 10 December (Holmgeirsson et al. 2010, Pálsson et al. 2014).

2.4.2.4 Anchor casing (24/March/2009 – 18/May/2009)

To drill further (anchor and production casing) it was proposed to use a new drilling rig. A Drillmec HH-300 rig was chosen and mobilised to the well site in the middle of March 2009 and drilling recommenced on 24 March (Holmgeirsson et al. 2010, Pálsson et al. 2014).

Anchor casing of the bottom hole assembly (BHA) consisted of a 16-1/2" roller cone tricone bit, a 9-1/2" mud motor, two 16-1/2" stabilizers, an Anderdrift tool, 9-1/2" and 8" drill collars, a shock sub, a jar, and heavy weight drill pipes (Holmgeirsson et al. 2010, Pálsson et al. 2014). Initially the drilling fluid used for the anchor casing was water to drill out the cement, however, when drilling into the formation at 803 m below the surface, the drilling fluid was changed back to mud. Drilling progress commenced well up to a depth of 2000 m below the surface although several unusual events occurred. These events included:

1. At 1194 m depth, a sudden pressure drop in the standpipe was observed and torque dropped. A float sub twisted apart in the BHA and the drill-string broke. Fishing took 48 hours to recover the broken piece. During this time, the mud motor was blocked and had to be replaced.
2. When drilling resumed the ROP was rather low (3-5 m/h). ROP decreased and testing showed either the bit or the mud motor was failing. A decision

was made to pull out of hole (POOH) from 1400 m below the surface. The mud motor was not working properly and was again replaced.

3. On reaching 1432 m below the surface, losses of 20 l/s were detected and a decision was made to POOH and cement off the loss zone to minimise mud losses, and to prevent interflow between loss zones during casing. After only drilling for a further 47 m, the bit was in a bad condition with almost all carbides broken off on the outer rows of the cones. On 7 April a junk basket was used to retrieve the missing carbides, however only formation cuttings and small metal fragments were retrieved. At the time the well appeared to be tight and the cement plugging was abandoned.
4. On 8 April the BHA was returned in hole (RIH) without a mud motor. No circulation losses were detected. An Anderdrift tool was used to measure the wells inclination which was 1.5°. On 13 April when drilling had reached 1907 m below the surface, the drill was POOH to replace the bit. The bit was badly worn and needed replacing. Drilling recommenced on April 15.
5. On 18 April at 2074 m below the surface a sudden drop on the standpipe was observed and the torque dropped. The drill collar had twisted apart and had dropped the lower string assembly. Fishing occurred for two hours to recover the BHA. A new BHA was run in the hole on 20 April and drilling resumed again from 2074 m below the surface.

On the morning of 21 April when drilling had reached 2101 m below the surface the torque values were fluctuating and the drill was pulled out for reaming (Holmgeirsson et al. 2010). When the last single was pulled out the weight of the bit dropped by 20 tons and the standpipe pressure decreased. The BHA had broken and fishing attempts were carried out over six days to recover the broken assembly. These attempts were unsuccessful. (Holmgeirsson et al. 2010, Pálsson et al. 2014). During this time the cause of the drill string loss was unknown, it was later interpreted as the drill string becoming stuck in response to interception with a magma body (Pálsson et al. 2014; Zierenberg et al. 2013; Saubin et al. 2017).

To continue drilling, a side-track to pass the fish was necessary. A 100 m thick cement plug was placed above the fish. On 12 May the drill bit was in formation at 1934 m below the surface, however the conditions in the well became difficult (Holmgeirsson et al. 2010, Pálsson et al. 2014). Sufficient hole cleaning was hindered by washout and circulation losses. To make hole cleaning more effective and to reduce the risk of a cave-in from the surface to 2000 m below the surface, a modification to the casing program was decided. Instead of having the anchor casing to 2400 m below the surface, it was changed to 2000 m below the surface. Drilling for the anchor casing was completed at 2005 m depth (Holmgeirsson et al. 2010, Pálsson et al. 2014).

The casing job started on the 18 May. The anchor casing consists of two sections of different thicknesses. The top 300 m were 13 5/8" Ib/ft T9, the remaining casing was 13 3/8" 72 Ib/ft K-55 (Holmgeirsson et al. 2010, Pálsson et al. 2014). The casing shoe was set at 1949 m below the surface and 24 m above the shoe was a stab-in float collar (Pálsson et al. 2014).

2.4.2.5 Production casing (25-May-2009 – 25-June-2009)

Drilling for the production casing started on the 25 May. Once the cement had been drilled out, the challenge was to circulate the cuttings from the bottom with 12-1/4" drill bit in a 16-1/2" hole (Holmgeirsson et al. 2010, Pálsson et al. 2014). To overcome this, the plan was to drill with high viscous pills with a relatively low ROP and low pumping rate, after which the pumping rate would be increased and the string rotated and moved up and down hole (Holmgeirsson et al. 2010, Pálsson et al. 2014).

On 8 June at 2103 m below the surface, there was a sudden rise in torque and the string became stuck for two minutes (Pálsson et al. 2014). Using 160 tons the string was freed and one single was pulled out. Several high viscous pills were used to circulate the drill for one and a half hours. After circulation, a string was lowered to the bottom of the hole. When the bit reached the well bottom, the torque once again increased and the bit was pulled up 13 m. A few minutes later

the torque increased and the drill string got stuck (Holmgeirsson et al. 2010, Pálsson et al. 2013). Immediately after the standpipe pressure increased and there was a loss in circulation (Holmgeirsson et al. 2010, Pálsson et al. 2014). On 10 June the string was on the surface and fishing attempts with jarring and pulling was commenced. Fishing was carried out for two days without success. A possible reason identified for the string being stuck was that the cement had caved in. It was decided to attempt to dissolve the cement by pumping down two pills of hydrochloric acid. However, the drill string was not freed and the drill string was detached again and a second side-track was planned (Holmgeirsson et al. 2010, Pálsson et al. 2014). The cause behind the stuck bit at the time was unknown, this event was later interpreted as a second interception with the magma body (Pálsson et al. 2014; Zierenberg et al. 2013; Saubin et al. 2017).

Two attempts were needed to cement above the fish. On 15 June, a cement plug was placed from the top of the fish at 2072 m below the surface, up to 1927 m below the surface (Holmgeirsson et al. 2010, Pálsson et al. 2014). On the same day a side-track was attempted, however, the cement was too soft for side-tracking and the bit was pulled out to allow the cement to harden. On 19 June side-tracking commenced at a depth of 1985 m below the surface (Holmgeirsson et al. 2010, Pálsson et al. 2014). During side-tracking the bit was in the country rock but no cement was observed. Torque and pressure fluctuated and big chips of fine-grained basalt were recovered. These unexpected returns were explained as resulting from thermal cracking of the formation, which is believed to be above 340 °C and was cooled repeatedly as a result of the length of time that the hole was open below the casing shoe (Holmgeirsson et al. 2010, Pálsson et al. 2014). On reaching 1992 m below the surface it was decided to POOH and lay down the mud motor to reduce the chances of the drill string becoming stuck again. On 23 June, drilling resumed at a low ROP. At 2071 m below the surface total loss of circulation occurred. High viscous pills were pumped down two times to keep the well clean and maintain this state. Drilling was running fine until reaching 2100 m below the surface (Holmgeirsson et al. 2010, Pálsson et al. 2014).

On 25 June at 2104.4 m depth the rate of penetration doubled from 2 m/hr to 4 m/hr, the torque increased and the string was stuck and had to be pulled free (Holmgeirsson et al. 2010, Pálsson et al. 2014). A single was pulled out and the well was circulated for 90 minutes. The bit was run down to the bottom again and the torque increased again at the same depth. When running in again (2 m) the top drive and the single on the floor moved upwards and the weight decreased by 45 tons and immediately the string was stuck. Circulation was managed to be maintained and the returns were pulsating to the surface initially but became steady (Holmgeirsson et al. 2010; Zierenberg et al. 2013). The returns included quenched glasses, which initially were clear containing relatively spherical bubbles, however, they became red-brown in colour (further detail on the recovered glass cuttings in section 2.4). Circulation was maintained for 24 hours without moving the string, but after a while there were no returns. After the string was pulled out the POOH commenced and the bit was in excellent condition. It was clear that at 2104.4 m the drill had drilled into magma. Further drilling was pointless and the drill hole was capped (Holmgeirsson et al. 2010; Zierenberg et al. 2013.

Fig 2.3 summarises the IDDP-1 drill, the depths reached for each casing and the estimates of the magma intercepts. During the drilling of the IDDP-1 magma was intercepted three times between 2101 – 2104.4 m depth. Magma interception occurred when there was an increase in standpipe pressure followed by a decrease in weight on the bit. This was interpreted as representing the ascent of magma within the borehole (Saubin et al. 2017).

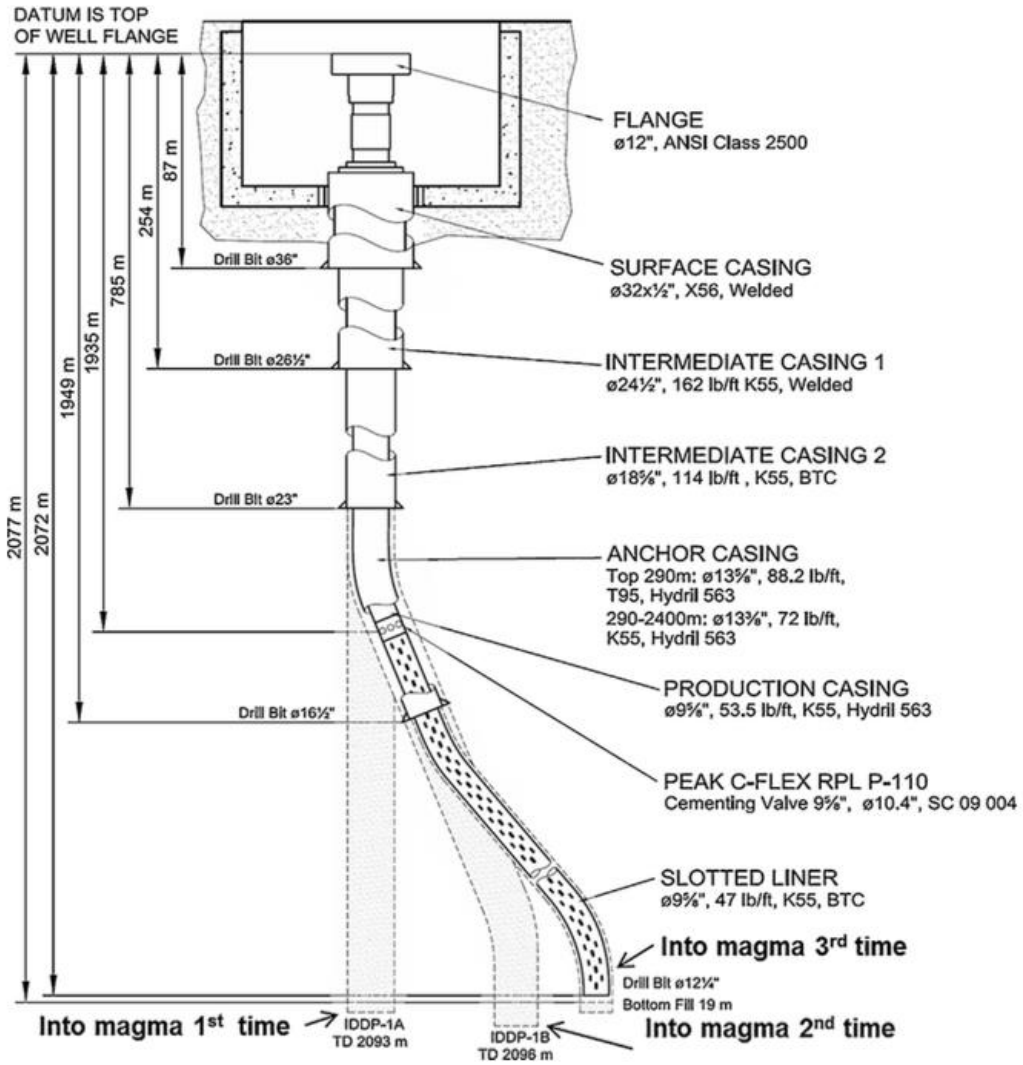

Figure 2.3: Overview of the IDDP-1 drilling configuration illustrating key changes in casing used at depth over the campaign. Figure from Pálsson et al. (2014).

2.5 The recovered glass cuttings

2.5.1 Time constrained glass cuttings

The set of samples received for this project were retrieved in a time-series from 15:17 on 24 June 2009 to 00:50 on 26 June 2009. The colour and vesiculation of these glass cuttings have been determined by observations made through a binocular microscope (Saubin et al. 2017).

Initially, clear sparsely phyric pumiceous glass fragments (Fig 2.4a) were most abundant in the returned cuttings (Holmgeirsson et al. 2010, Pálsson et al. 2014, Zierenberg et al. 2013). The proportion of the clear glass cuttings decreases significantly after 17:00 (Fig 2.5, Saubin et al. 2017) and the dominant cuttings recovered from the IDDP-1 become sparsely phyric, dark brown, poorly vesiculated glass (Fig 2.4b). Bubbles in the glass cuttings were initially spherical in shape, suggesting that the melt was not being significantly sheared at the time it was quenched. In contrast the bubbles in the later recovered cuttings were highly elongated, suggesting shearing due to movement of the magma. Both clear and brown glass have a refractive index of 1.49 (Zierenberg et al. 2013). Zierenberg et al. (2013) suggest that the textural change of the glass indicates that the pressure or quench time of the magma varied over time during penetration by the drill bit.

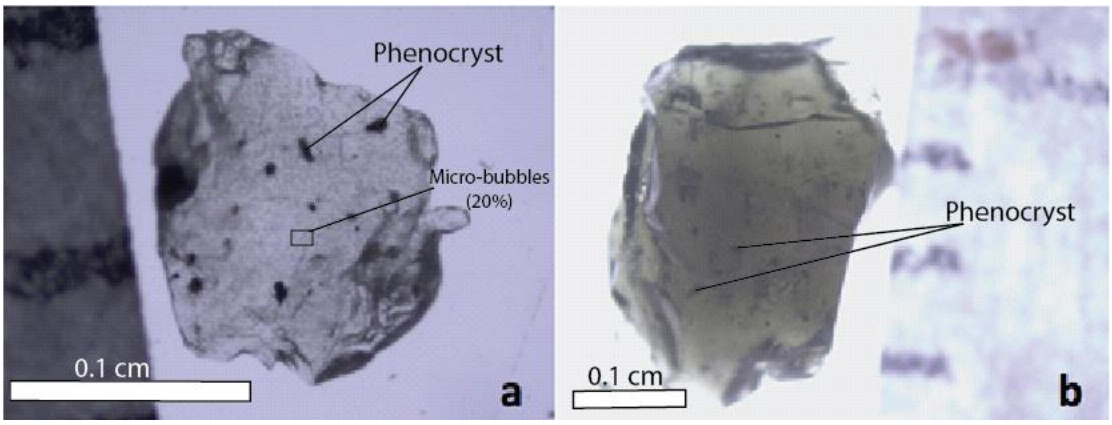

Figure 2.4: Example of glass cuttings from IDDP-1 showing colour variation. a) Clear glass with micro-vesicles and phenocrysts; b) Brown glass with no micro-vesicles.

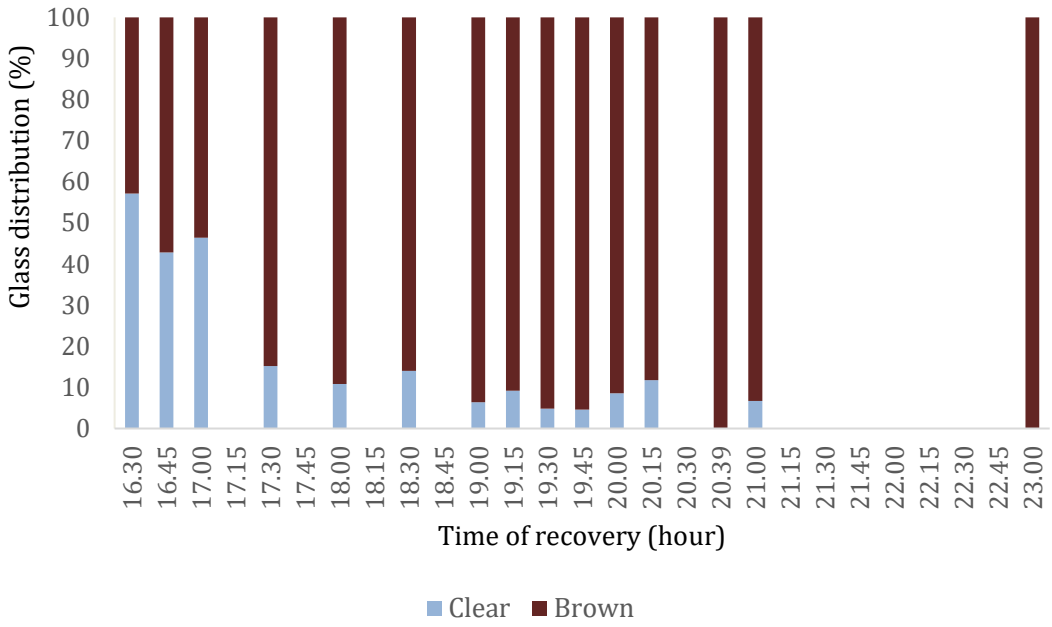

Figure 2.5: Variation of colour of the recovered glass cuttings with time. Figure obtained from Saubin et al. 2017)

The glass cuttings have been separated into low vesicularity (<5% bubbles) and high vesicularity (>5%). The majority of the cuttings that have a high vesicularity are clear (77.08%), whereas the majority of glass cuttings that have a low vesicularity are brown (Figure 2.6).

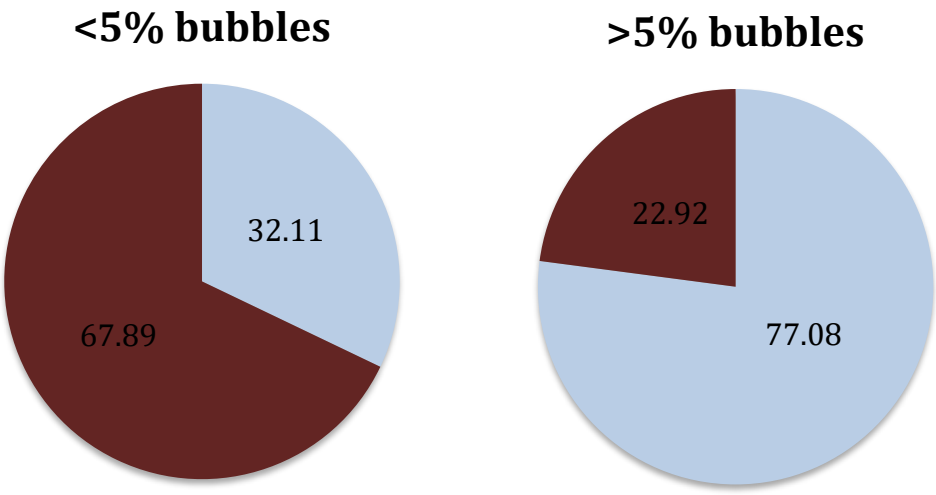

Figure 2.6: Variation of glass colour with vesicularity. Most high vesicularity glasses are clear, and most low vesicularity glasses are brown. Figure from Saubin et al. (2017)

2.6 Previous work on the IDDP-1 glass cuttings

The unexpected interception of the magma provides many opportunities for research as it gives a direct insight into a resting magma body. This not only presents opportunities for understanding the evolution of rhyolitic magma chambers, but also raises possibilities for future geothermal development. All glass cuttings used in previous studies were received at 1700 (Saubin pers.comm., 2017).

2.6.1 Glass and mineral chemistry

Previous work on the glass cuttings by Zierenberg et al. (2013) has included characterising their composition and determining the origin of the magma. Based on petrography, Zierenberg et al. (2013) identified three chemically distinct high-silica rhyolite glasses quenched from melt by the drilling fluid.

- Melt-1 is the dominant type of glass recovered from the IDDP-1 and is interpreted to be the quenched intersected magma. Zierenberg et al., (2013) defines Melt 1 to include both clear and brown glass cuttings described in this thesis. The clear glass is termed Melt-1a in this thesis, and the brown glass is termed Melt-1b.
- Melt-2 is a crystalline felsic intrusive rock with quenched rhyolite glass. It is believed to be representative of the host rock into which the rhyolite melt was emplaced. The felsite is composed of alkali feldspar, plagioclase, quartz, titanomagnetite and augite; the rhyolite glass makes up variable amounts of the felsite (up to ~20%).
- Melt-3 is a glass that is textually, and mineralogically similar to the felsite (except that it contains less alkali feldspar or contain small irregular grains of residual alkali feldspar). It contains abundant crystals and/or glomerocrysts of quartz, plagioclase, augite and magnetite. There are signs of resorption with some plagioclase crystals exhibiting irregular compositional zoning and quartz crystals highly embayed. The glass in these crystal rich cuttings is typically moderately vesicular. The textures of Melt-3 suggest that it has invaded and partially assimilated the felsite.

Zierenberg et al. (2013) used an electron probe microanalysis (EPMA) to determine the glass composition of the glass cuttings and X-ray fluorescence to determine the whole rock chemistry. Table 2.1 summarises their glass and whole rock compositions.

Table 2.1: Summary of the major elements composition of glass (wt%) and the whole rock chemistry determined by X-ray fluorescence. Major oxide and the whole rock chemistry normalised to 100 wt% on an anhydrous basis. Data obtained from Zierenberg et al. (2013).

	Melt-1 (n=5)	**STDEV**	**Melt-2 (n=6)**	**STDEV**	**Melt-3 (n=3)**	**STDEV**	**JB-2 (felsite)**
SiO_2	76.47	0.4	77.04	0.43	77.81	0.09	75.66
TiO_2	0.33	0.04	0.21	0.05	0.2	0.02	0.42
Al_2O_3	12.02	0.1	11.68	0.08	11.69	0.05	11.98
FeO	2.75	0.16	1.84	0.14	1.85	0.06	2.99
MnO	0.07	0.02	0.09	0.04	0.02	0.02	0.07
MgO	0.19	0.04	0.07	0.01	0.10	0.01	0.35
CaO	1.35	0.13	0.48	0.02	0.72	0.04	1.67
Na_2O	3.79	0.07	3.55	0.12	3.58	0.05	4.04
K_2O	3.05	0.08	5.05	0.21	4.01	0.11	2.75
P_2O_5	n.a	-	n.a	-	n.a	-	0.07

The major oxide analysis has shown that all the melts are high-silica rhyolites. The difference between Melt-1 and Melt-2 is the higher K_2O and lower CaO content in Melt-2. The composition of Melt-1 is similar to the whole rock composition of crystalline felsite (JB-2). The composition of Melt-3 glass lies between Melt-1 and Melt-2 on a plot of Na_2O versus K_2O (Fig 2.7a) and K_2O versus CaO (Fig 2.7b), suggesting it is a mixture of Melt-1 and Melt-2. However, Melt-3 shows higher SiO_2 content than the other two melts (Fig 2.7c-d), which is consistent with the textural evidence of quartz resorption.

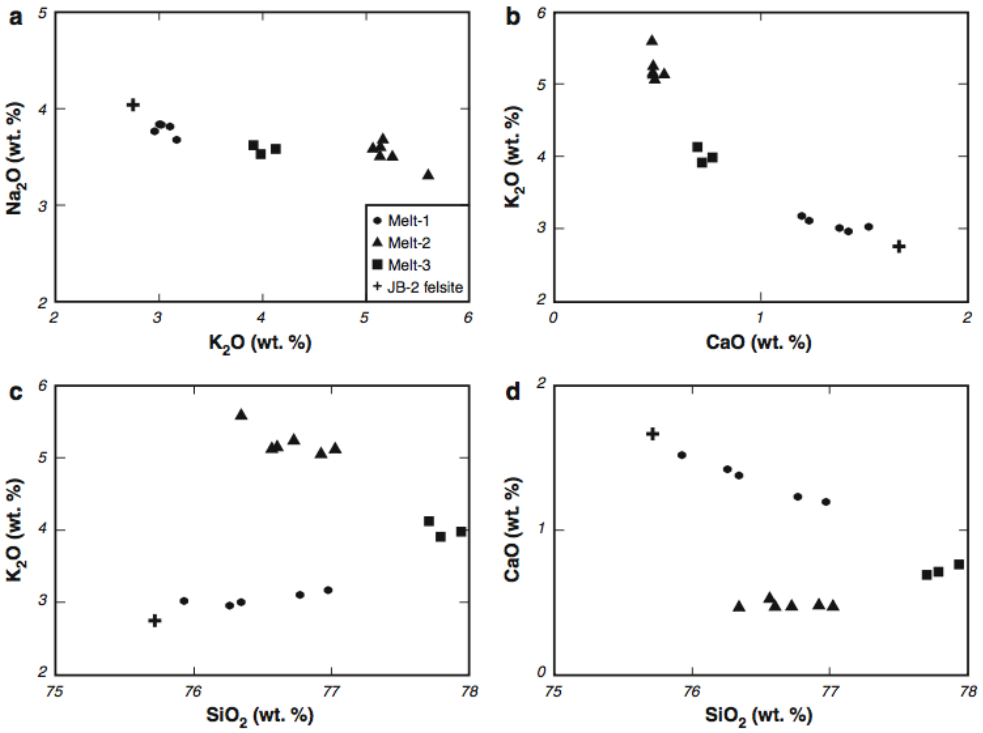

Figure 2.7: Chemical variation diagrams for the different glasses and the crystalline felsite (JB-2). Data are normalised on an anhydrous basis. a) K_2O versus N_2O, b) CaO versus K_2O, c) SiO_2 versus K_2O and d) SiO_2 versus CaO. Figure from Zierenberg et al. (2013).

2.6.2 H_2O and CO_2

Table 2.2 summarises the volatile measurements on the quenched Melt-1 glasses done by Zierenberg et al. (2013). Vesiculated glass have volatile contents identical to the more common non-vesiculated glass. The high ratio of OH to H_2Om in the glass suggests that the melt was quenched to glass at a high temperature by the drilling fluid (Zierenberg et al. 2013).

Table 2.2: H_2O and CO_2 content of Melt-1 from Zierenberg et al. (2013). Volatile content is determined by FTIR.

Sample	H_2O_m (wt%)		OH (wt%)		H_2O_t (wt%)		CO_2 (ppm)	
Vesiculated (n=2)	0.58	0.05	1.12	0.06	1.7	0.01	78	8
Non Vesiculated (n=11)	0.6	0.11	1.18	0.09	1.78	0.15	87	16
Average	0.6	0.02	1.17	0.04	1.77	0.17	85	15

Zierenberg et al. (2013) calculated the H_2O-CO_2 saturation pressures of the glasses using VolatileCalc (Newman and Lowenstern 2002) assuming a temperature of 900 °C (section 2.4.3). The H_2O-CO_2 saturation pressures are mostly between 35 and 45 MPa (Zierenberg et al. 2013). These pressures are below the lithostatic pressure but greater than the hydrothermal system (Fig. 2.8). Pressures above the hydrostatic pressure in an active geothermal field suggest that there must be a low permeability barrier that separates the melt from the overlying convection hydrothermal system (Zierenberg et al. 2013). Loss of circulation prior to the intercepting the magma suggests that a high permeability zone existed above the magma.

Trewick et al. (2016) investigated the vesiculation history of the magma and attempted to characterise the average H_2O concentration and the bubble population density in quenched glass with different textures. The results show that H_2O concentrations have some spatial variability, and they observed enrichment of H_2O towards the bubbles, which they suggested was the result of resorption. However, mean H_2O values for the clasts they analysed ranged from 1.41 – 1.68 wt %, with no statistically significant difference between glass cuttings that exhibit different textures.

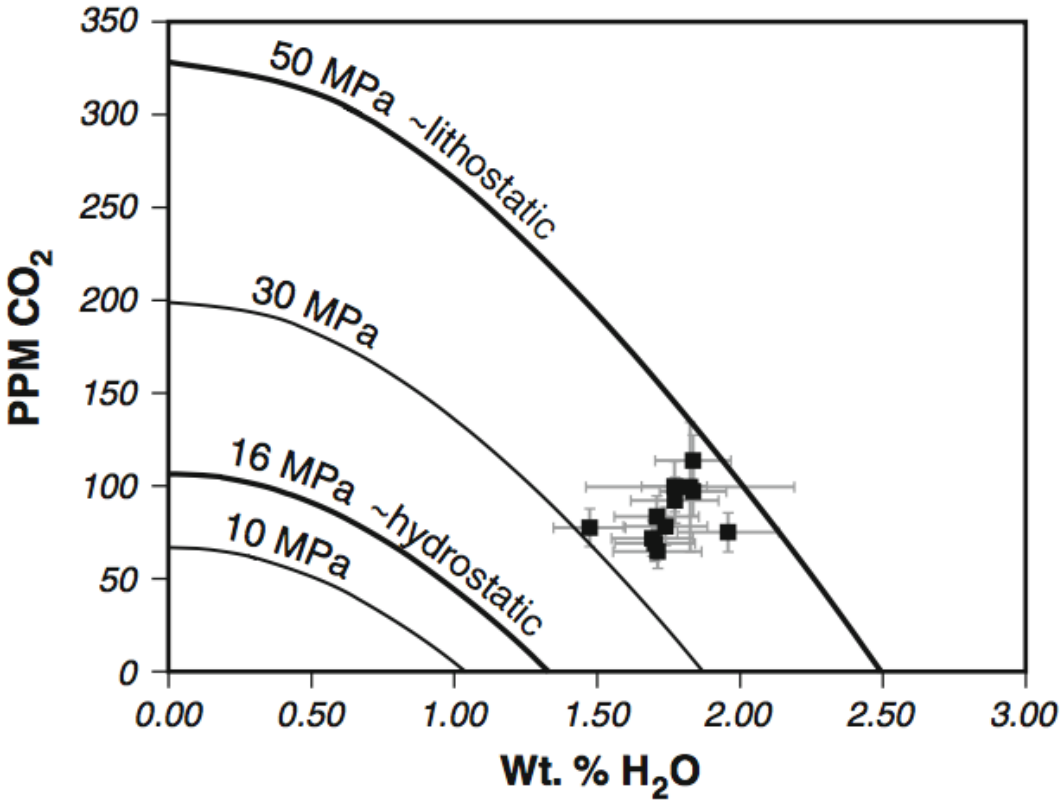

Figure 2.8: H_2O versus CO_2 in Melt-1 glass. Saturation pressure contours were calculated using VolatileCalc (Newman and Lowenstern 2002). Figure obtained by Zierenberg et al. (2013).

2.6.3 Temperature estimates

Previous work on the IDDP-1 glass cuttings includes estimating the temperature of the intercepted melt. Based on two-pyroxene geothermometry and modelling of the crystallisation sequences, Zierenberg et al. (2013) estimate the in situ temperature of the magma to be between 850 – 920 °C. The high ratio of dissolved OH to H_2O_t (0.66) indicates that the magma was quenched at temperatures between 760 and 940 °C (Elders et al. 2014).

Using a Horner plot the temperature of the host rock (Felsite) the magma was sitting was indicated. Horner plots are an experimental analysis which can be used in drilling operations to derive reservoir pressure and/or temperature conditions. This is done through the derivation of a heating rate at hole bottom following temporary well closure (Dowdle and Cobb, 1975). Based on temperature logs from 13 October 2009, 3 December 2009 and 28 January 2010,

the host rock temperature was indicated to be ~500 °C (Fig 2.9), (Morstensen et al. 2014).

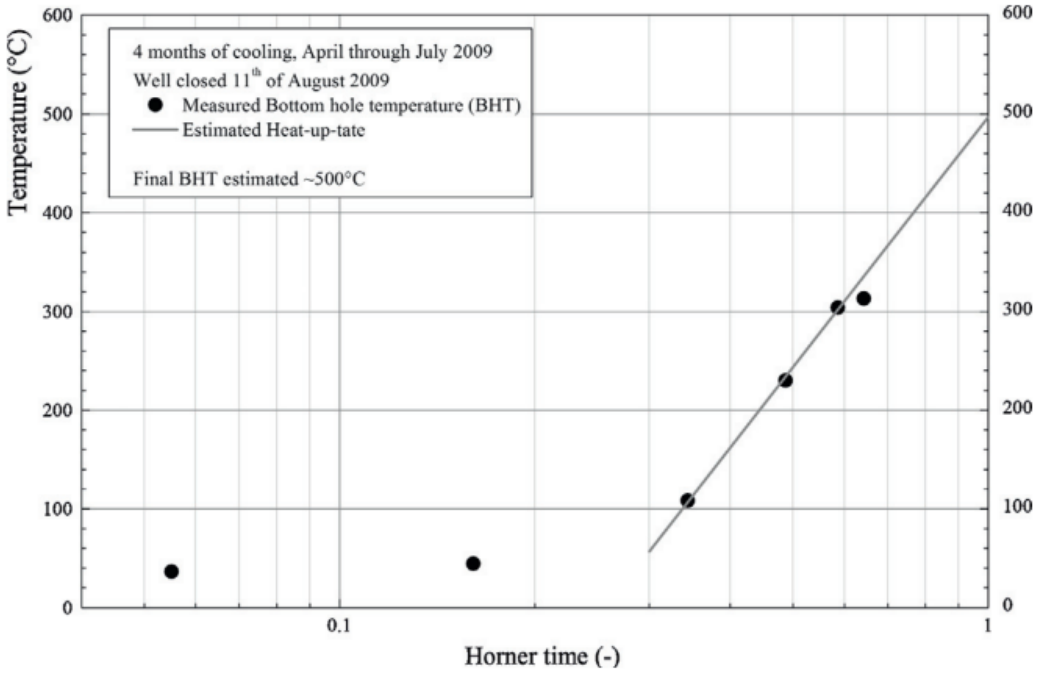

Figure 2.9: Horner plot for six recovery logs from the ICCP-1 borehole. Assuming no active convection processes near the bottom, temperature recovery indicates ~500 °C near the bottom of the well. From Mortensen et al. (2014).

2.7 Project objective

This project will differ from previous work on the Krafla glass cuttings as it will investigate the magmatic volatile (H_2O and CO_2) content, the glass composition and the glass texture in glass cuttings that were collected over the time period that circulation was maintained after the third interception of the magma body and returns of quenched glass reached the surface. The time of return of each glass cutting has been recorded allowing these samples to be used to understand how the magma responded to being intercepted by the drilling. Samples that Zierenberg et al. (2013) interpreted as the magma body (i.e. Melt-1) were selected. A total of 18 glass cuttings with different colour and vesicularity were selected (Table 2.3). For this project, the glass cuttings have been grouped into two categories based on textural characteristics; clear glass cuttings (termed Melt-1a) and brown glass cuttings (termed Melt-1b).

Table 2.3: Summary of the sample analysed by FTIR. Sample name based on time of the glass cutting recovery.

Sample	Colour	vesicularity
1545	Melt-1a	<5%
1645B	Melt-1b	>5%
1645C	Melt-1b	<5%
1645D	Melt-1a	>5%
1730B	Melt-1b	<5%
1730C	Melt-1b	>5%
1800A	Melt-1b	>5%
1800B	Melt-1b	<5%
1800C	Melt-1b	>5%
1800E	Melt-1b	<5%
1830C	Melt-1a	<5%
1915	Melt-1b	<5%
1945A	Melt-1b	<5%
1945B	Melt-1b	<5%
2015	Melt-1b	<5%
2039C	Melt-1b	<5%
2039D	Melt-1b	<5%
0050	Melt-1b	>5%

2.7.1 Additional glass cuttings

In addition six glass cuttings collected together at 1700 on 25 June have been included. These glass cuttings consist of brown (Melt-1b) clasts ranging in vesicularity (Table 2.4). H_2O contents for these samples had already been collected using Fourier transform infrared spectroscopy using a conventional bench-top globar source and focal-plane-array camera detector (FPA-FTIR) and these data (Joyce, pers. Comm. 2017) have been processed to allow comparison to the time-series of samples.

Table 2.4: Summary of the textural description of the additional Krafla glass cuttings.

Sample	Colour	Vesiculation
Ice 216-3	Melt-1B	<5%
Ice 220-8	Melt-1B	>5%
Ice 214-7	Melt-1B	>5%
Ice 217-2	Melt-1B	<5%
Ice 219-5	Melt-1B	<5%
Ice 221-1	Melt-1B	>5%

2.8 Summary

Preparation of the IDDP-1 well drilling started in the year 2000 and continued until drilling activity started in mid-2008. The IDDP-1 well was designed to to drill down to ~4-5 km in order to reach fluids. However drilling problems occurred for nearly three months from March 2009. Drilling problems included getting stuck, having twist offs, which results in side-tracking at two different times (21 April and 8 June). The causes of these issues become clearer at 2104 m depth. On 24 June the rate of penetration increased, the torque increased and the string got stuck and the drill moved upwards. It was clear the drill bit drilled into a magma body of some size. Drilling stopped when the magma was intercepted, however circulation continued and glass cuttings were recovered and time of recovery recorded. Initially clear glass cuttings were the most abundant and then decreased and dark brown glass cuttings became dominant. Previous studies have indicated that the magma body consists of high silica (76.5% SiO_2) rhyolite melts with an in-situ temperature estimated between 850 and 920 °C emplaced in a country rock at ~500 °C. Previous volatile studies show that the quenched melt contains 1.77 wt% H_2O and 85 ppm CO_2, indicating that the in situ pressure is above hydrostatic (~16 MPa) and below lithostatic (~55 MPa). In summary, these previous studies have not looked at how the characteristics of the volatiles dissolved in the melt changed with time. This project will differ from other work by examining the time-series of cuttings. The clear glass (Melt-1a) and the brown

glass (Melt-1b) will also be examined to determine whether they came from different sources.

Chapter 3: H_2O, CO_2 and silicate melts

3.1 Introduction

Volatiles are a very important factor in magmatic processes (Sparks, 1978). Dissolved volatiles change the physical and chemical properties of melts and are a driving force of volcanic eruptions. Silicate melts like the Krafla glass cuttings contain dissolved volatile species that are weakly soluble, and exsolve to form bubbles. The most common magmatic volatiles are H_2O and CO_2. This chapter presents an overview of the structure and composition of silicate melts, the mechanisms and controls of magmatic volatile solubility and diffusion in the melt, and how these factors influence bubble growth and resorption. Understanding the role magmatic volatiles have on melts and their properties can help determine the causes of the volatile distributions observed in the Krafla glass cuttings (Chapter 5) and give an insight to the magmatic evolution which occurred owing to the interception of the magma by IDDP-1 drilling (Chapter 6).

3.2 Silicate melts

Silicate melts consist primarily of silicon, oxygen, aluminium, alkalis, magnesium, titanium and iron. The basic unit is a silicon atom in tetrahedral co-ordination with four oxygen atoms. These silicate tetrahedra are usually found in conjunction with other silicate tetrahedra or charge balancing cations. A pure silicate melt consists only of Si and O and forms an array of silicate tetrahedra linked together at all corners by strong Si-O covalent bonds (Bottinga & Weill 1972). In the presence of other elements in the magma, the silicate tetrahedra network becomes altered. Network formers are those elements which can substitute for Si in tetrahedral sites without affecting the melt structure. Network formers in silicate melts include Ti^{4+}, Al^{3+} and Fe^{3+}. The lower charges of Al and Fe means that they can only act as network formers in the presence of other cations, which are required to maintain charge balance. If the supply of charge-balancing cations is exhausted, Al and Fe will act as network modifiers.

Other network modifiers include Na, K, Mg and Ca, which bond with O to form metal oxides (MO). Network modifiers cause Si-O-Si linkages to break, with some Si-O bonds replaced with M-O bonds. This weakens the adjacent Si-O bonds because the cations polarise the shared O (Bottinga and Weil, 1972).

3.2.1 Melt classification

A silicate melt entirely composed of network formers in tetrahedral sites is fully polymerised. Melt structure becomes increasingly depolymerised with addition of network modifiers as they break up the tetrahedral network (Bottinga and Weil, 1972). The degree of polymerisation controls the melt viscosity. Silicate melts are classified by their composition, typically by the proportions of SiO_2 and alkalis (Na and K). Generally, melt polymerisation increases with increasing SiO_2 content and decreases with increased Alkali content. Total Alkali Silica (TAS) diagram (Fig 3.1) are used to represent these properties.

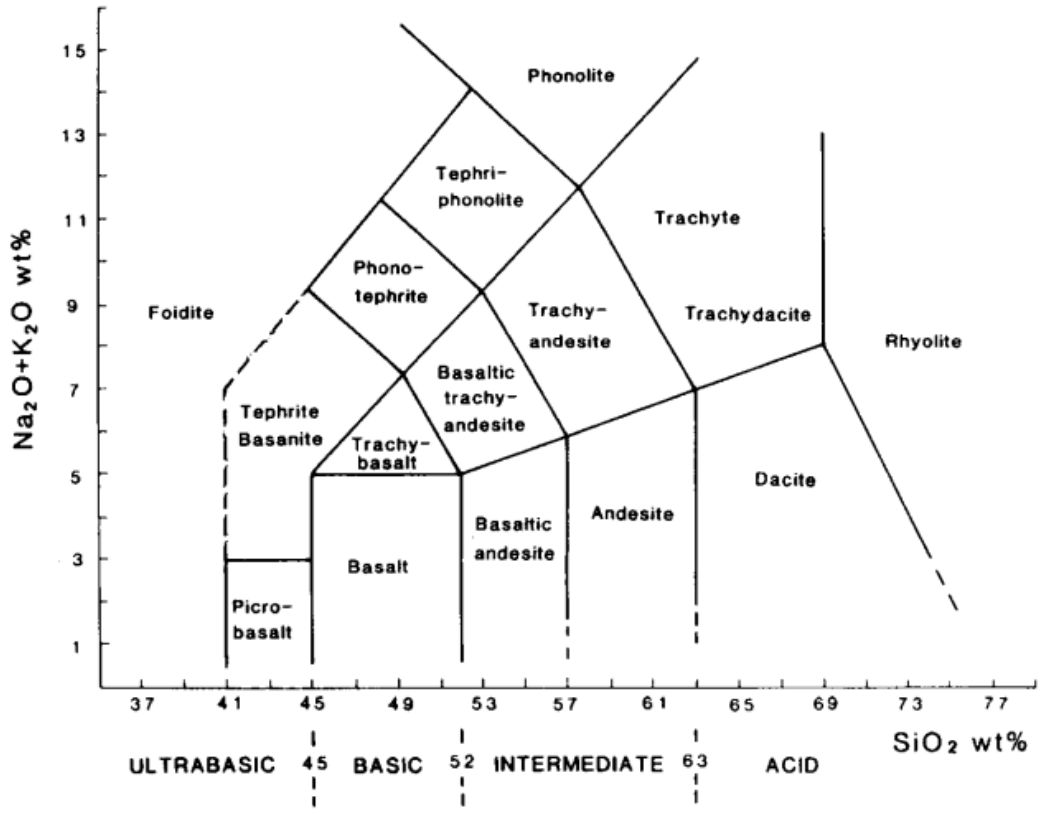

Figure 3.1: Total Alkali Silica (TAS) plot. Figure obtained from Le Bas and Streckeisen (1991).

3.3 Magmatic volatile

Naturally occurring silicate melts will contain a variety of dissolved volatiles. These species are weakly soluble in the melt. The most common volatiles are H_2O and CO_2. Other volatiles include S, Cl and F-bearing species.

3.3.1 H_2O speciation in silicate melt

In silicate melts, total H_2O (H_2O_t) is dissolved in two species, molecular H_2O (H_2O_m) and dissociated hydroxyl groups (OH). H_2O_m is neutral and does not affect the melt structure. OH groups are anions (OH^-) and act as network modifiers. Stolper (1982) showed these two species interconvert via the equilibrium reaction:

$$H_2O_m(melt) + O^{2-}(melt) \rightleftharpoons 2OH^-(melt) \qquad \text{Eq. 3.1}$$

in which H_2O_m reacts with a bridging oxygen (O^0) to form OH groups that are bounded to the silicate network and act as network modifiers (Stolper, 1982).

The H_2O speciation reaction (Eq. 3.1) is a reversible reaction. The equilibrium position of the reaction (K), represents what proportions of the two species are expected to be present in a range of given conditions. This equilibrium constant (K) for H_2O can be defined as

$$K = \frac{{X_{OH}}^2}{X_{H_2O_m} X_O} \qquad \text{Eq. 3.2}$$

where X represents the mole fractions on a single oxygen basis. The value of K determines the relative proportions of H_2O_m and OH in a melt for a given H_2O_t content when the system is in equilibrium, and the proportions vary with H_2O_t content. At low H_2O_t, OH is the dominant species, but H_2O_m becomes dominant at

higher H_2O_t. Higher K values indicate higher proportions of OH, which requires heat input to break bonds and thus is an endothermic process. In addition, as K varies with pressure, temperature and melt composition, equilibrium speciation also varies (Stolper 1982; Stolper 1989; Silver et al. 19990; Hui et al. 2008).

3.3.2 CO_2 speciation in silicate melt

CO_2 is the second most abundant volatile in natural silicate melts. CO_2 has two distinct species in silicate melts, molecular CO_2 (CO_{2m}) and carbonate groups (CO_3^{2-}). CO_{2m} is neutral and does not affect melt structure, but CO_3^{2-} reacts with network modifying cations therefore is not associated with depolymerisation of the melt (Fine and Stolper, 1985; Lowenstern 2001). These two species interconvert via the equilibrium reaction:

$$CO_{2_m}(melt) + O^{2-}(melt) \rightleftharpoons CO_3^{2-}(melt) \qquad \text{Eq. 3.3}$$

in which CO_{2m} reacts with bridging oxygen to from CO_3^{2-}. The equilibrium constant for CO_2 is as follows:

$$K = \frac{X_{CO_3^{2-}}}{X_{CO_{2m}} X_{O^{2-}}} \qquad \text{Eq. 3.4}$$

where X represents the mole fraction. In contrast to dissolved H_2O in silicate melts, in which the species concentration ratio depends strongly on H_2O_t, as total CO_2 varies, CO_{2m}/CO_{2total} and CO_3^{2-}/CO_{2total} are roughly the same (Zhang et al. 2007), although they do vary with melt composition. In rhyolitic melt, CO_2 is present as CO_{2m} and in basaltic melt, CO_2 is present as CO_3^{2-} (Zhang et al. 2007).

3.4 Temperature estimation

3.4.1 Equilibrium speciation temperature

Temperature is the strongest control on K for any composition. The relationship with K and temperature (T) is expressed by:

$$lnK = A + \frac{B}{T} \qquad \text{Eq. 3.5}$$

where A and B are constants related to the standard state entropy and enthalpy of Eq. 3.1 (Zhang and Ni 2010).

Studies of the effect of K with temperature are impacted by the quench effect (Section 3.4.2), which limits the temperatures that can be investigated as high temperature melts have to be quenched to glass for analysis at room temperature. Measurements of high temperature melts at room temperature are difficult because melt density and molar absorptivity coefficients vary with temperature (Zhang and Ni 2010). A study by Nowak and Behrens (2001) that investigated K in haplogranite is calibrated for 500 – 800 °C, 100 – 300 MPa and 1.27-5.15 wt% H_2O_t. Fig 3.2 shows the variation in speciation using the K derived by Nowak and Behrens (2001).

K also varies with composition, however, the variation for melt composition is less than for temperature. Zhang and Ni (2010) showed rhyolite melts exhibited a sharper decrease in K with temperature than dacite and andesite melts. The constants A and B in Eq. 3.5 vary with composition, however, the relationship between K and melt composition is not well characterised. Data for other compositions, such as basalt, trachyte and phonolite, are limited.

Hui et al. (2008) investigated the effect of pressure on K. They found there to be no dependence. The effect of pressure at <1 GPa is negligible therefore, the pressure effect can be considered negligible.

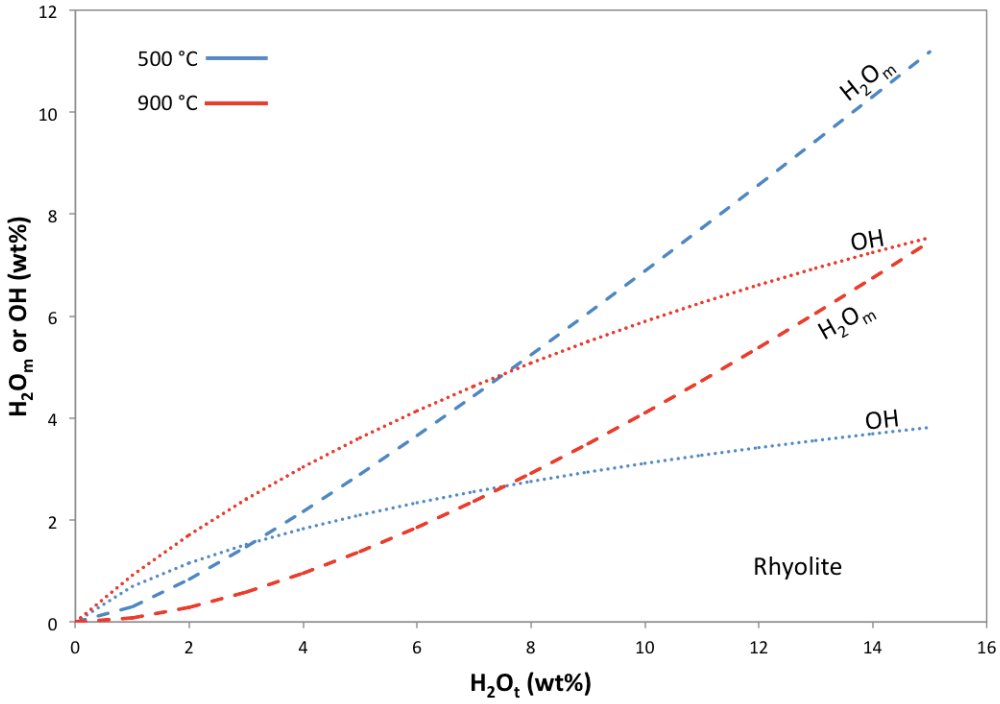

Figure 3.2: Variation in equilibrium speciation with temperature and H_2O_t concentration. Equilibrium speciation contours taken from Nowak and Behrens (2001). The data for the anhydrous glass composition used to calculate K are from the EPMA analysis on the Krafla glass cuttings (Chapter 5).

3.4.2 Quenching effect

The equilibrium speciation data obtained by experimental studies of melts at temperature above ~1000 K (eg., Silver and Stolper 1989; Stolper 1989; Silver et al. 1990) are now known to have been affected by the quench effect (Zhang et al. 2010). During the initial stages of quenching the H_2O_m-OH interconversion reaction (Eq. 3.1) keeps pace with cooling and maintains equilibrium speciation until the reaction slows at lower temperatures. This results in a final volatile speciation that reflects an equilibrium at a cooler intermediate temperature rather than the original experimental temperature. Speciation data affected by the quench effect can be described by the apparent equilibrium constant, Q:

$$Q = \frac{[OH]^2}{[H_2O_m][O]} \qquad \text{Eq. 3.6}$$

The expression of Q is identical to the expression of K (Eq. 3.4), except K is only appropiate when the system is in equilibrium (Zhang and Ni, 2010). For a volcanic glass affected by the quench effect, the measured speciation will have an apparent equilibrium constant Q that is lower than the true equilibrium constant, K, of the original hotter temperature. Therefore, volcanic glasses affected by the quench effect have higher H_2O_m/OH ratios at higher temperature. The magnitude of the difference between K and Q is determined by the quench rate, with bigger differences caused by slower quench (Fig 3.3).

Like K, Q can be related to temperature as follows,

$$lnQ = A + \frac{B}{T_{ae}} \qquad \text{Eq. 3.7}$$

where T_{ae} is the apparent equilibrium temperature. T_{ae} is calculated from lnQ assuming Q is the same as K even though equilibrium is not reached at any temperature. Fig 3.3 illustrates the variation of Q and T_{ae} as a function of temperature during cooling at various quench rates (Zhang and Ni, 2010).

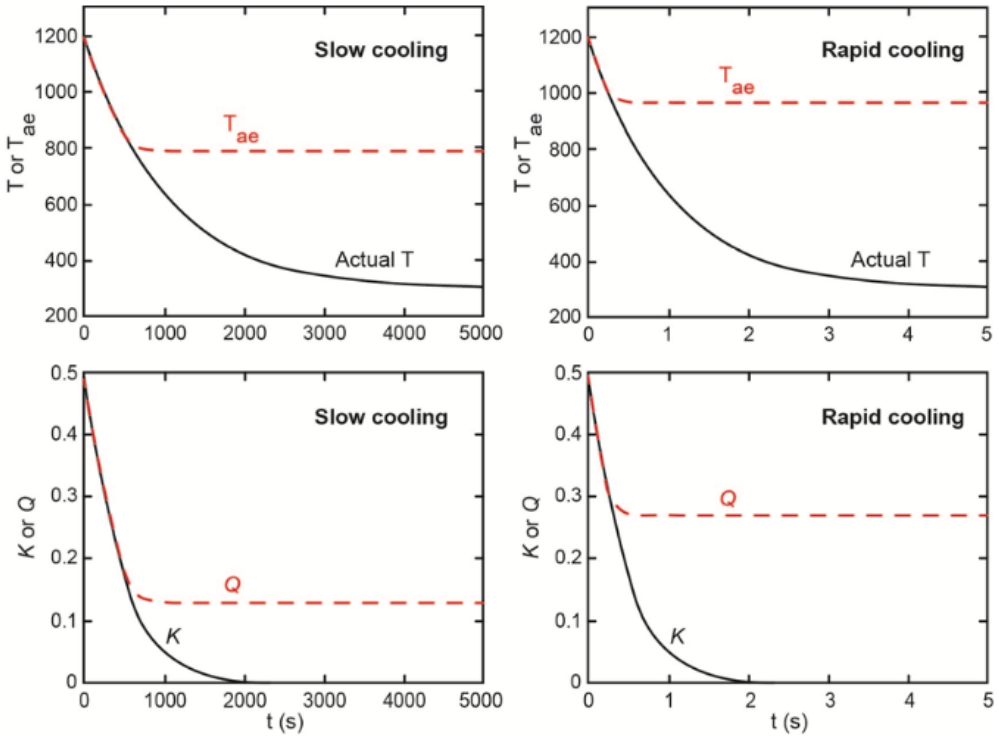

Figure 3.3: **Schematic evolution of Q and T_{ae} for rapid cooling and slow cooling of a hypothetical reaction**. Figure from Zhang and Ni (2010).

3.5 Melt viscosity

3.5.1 Effect of H_2O and CO_2

Viscosity is a measure of a melt's resistant to flow (Pa s). Dissolved OH groups act as network modifiers that reduce melt polymerisation, and therefore melt viscosity decreases with increasing H_2O_t. Studies by Hess and Dingwell (1996) have shown that viscosity of rhyolite melts vary by more than seven orders of magnitude for H_2O_t concentrations of 0.01 to 8 wt% (Fig 3.4a). The decrease of viscosity with increasing H_2O_t is the most significant with the addition of the first 1 wt% of H_2O_t (Hess and Dingwell, 1996). The effect diminishes for every additional wt%.

Data on the effect of CO_2 on silicate melt viscosity is limited with studies indicating that CO_2 does not appear to affect the viscosity (Lange, 1994; Morizet et al. 2007). It is believed that it has no effect because its dissolution does not alter the fundamental silicate melt structure. However, in recent study by Morizet et al. (2017) have measured glass transition temperature (section 3.6.1) in low silica melt decreases with increasing CO_2 content, therefore viscosity decreases. This contradicts the melt polymerisation because CO_2 are neutral in melt. However, since the Krafla melt is high in silica, the effect CO_2 on melt viscosity would not be considered.

3.5.2 Effect of temperature

Temperature is the strongest control on melt viscosity, where melt viscosity increases with decreasing temperature. Melt viscosity displays non-Arrhenian behaviour (non-linear) with temperature, usually expressed as $1/T$ (Hess and Dingwell, 1996). Fig 3.4b shows the variation of viscosity with temperature, with all melt compositions showing a decrease of viscoisty with increasing temperature. The exact nature of this temperature-dependence varies with the anhydrous composition and volatile content of the melt.

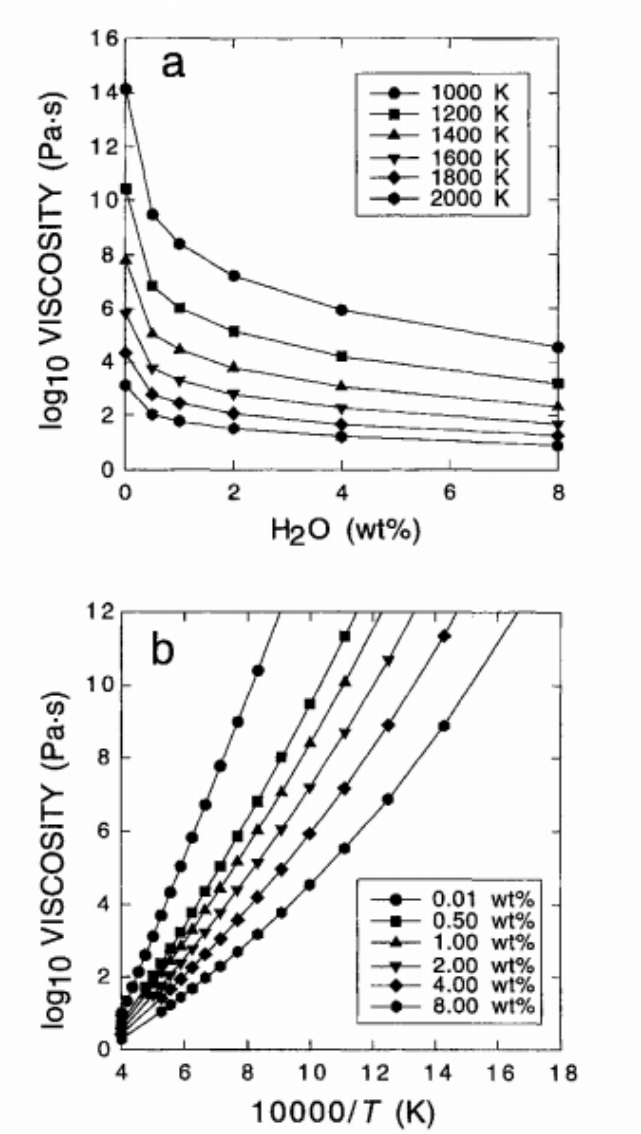

Figure 3.4: Variation of rhyolite viscosity with temperature and H_2O concentration. a) Variation of viscosity with H_2O concentration at different temperatures. b) Variation of viscosity with temperature at constant H_2O concentration. Figure from Hess and Dingwell (1996).

3.6 Melt to glass

The transition between liquid-like and glass-like behaviour over a temperature interval is known as the glass transition (Fig. 3.5). The transition from liquid to glass occurs when the liquid is unable to achieve equilibrium due to external perturbation (Dingwell & Webb 1989). In volcanic contexts this is most likely due to rapid cooling, or from deformation during flow. The ability of the melt to

maintain an equilibrium state is controlled by the structural relaxation timescale of the melt. Structural relaxation timescale is controlled by the rate of self-diffusion of Si and O atoms in the liquid matrix (Dingwell 2006). The self-diffusion involves breaking Si-O bonds (Dingwell and Webb, 1989). If the timescale of perturbation is more rapid than this structural relaxation timescale, the silicate structure is unable to deform rapidly enough to maintain an equilibrium liquid state and the melt begins to act like a solid and therefore becomes a glass.

The structural relaxation timescale of a melt is given by the Maxwell relationship:

$$\tau_s = \frac{\eta_s}{G^\infty} \qquad \text{Eq. 3.8}$$

where τ_s is the structural relaxation timescale, η_s is the shear viscosity and G^∞ is the shear modulus and can be considered to be constant ($\sim 10^{10}$ Pa; Dingwell and Webb, 1989). The structural relaxation timescale of a melt varies with temperature and volatile content, like melt viscosity.

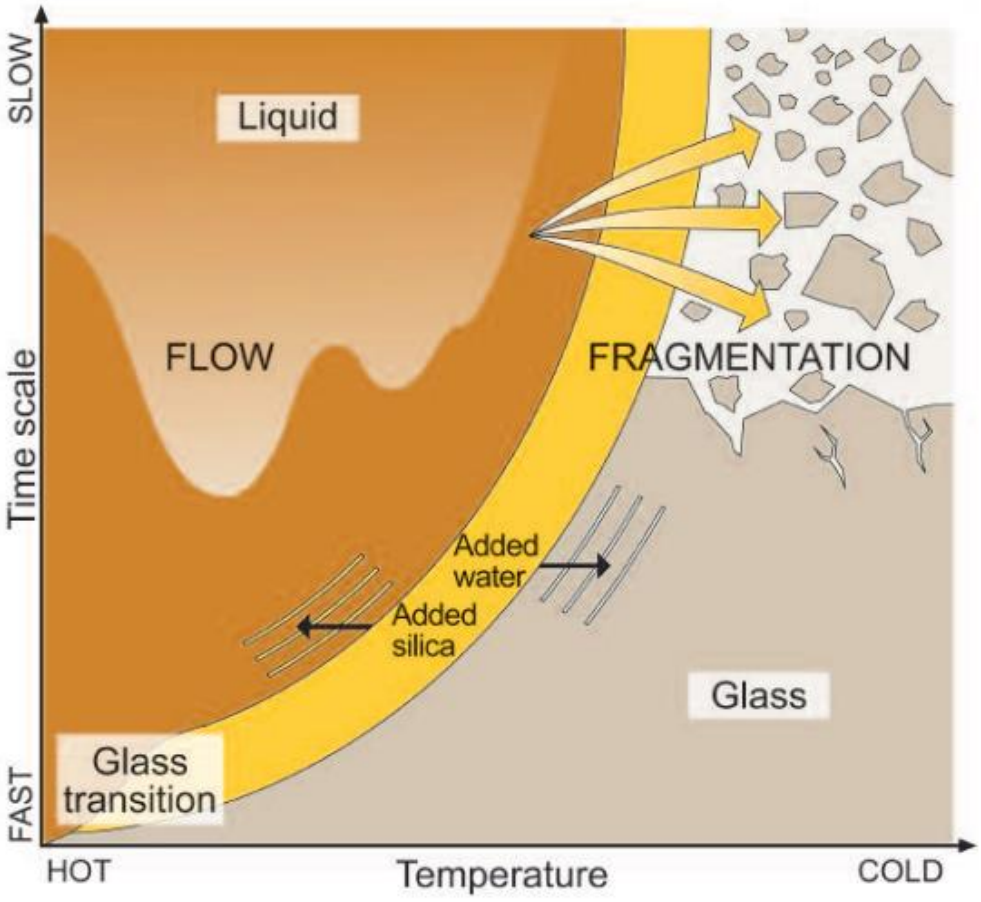

Figure 3.5: Schematic drawing of glass transition for a silicate melt. The glass transition separates the liquid and solid response of the molten state. Figure from Dingwell and Webb (1989).

3.6.1 Glass transition temperature

The glass transition occurs over a temperature interval, the exact definition of T_g differs depending on how it is determined. The two most common techniques used to determine T_g are dilatometry and calorimetry. In dilatometry studies, T_g is defined as the temperature at which the melt viscosity is 10^{12} Pa s (Giordano et al. 2008). In calorimetric studies, a glass sample is repeatedly heated and cooled across the glass transition at different heating/cooling rates. This method is able to measure the variation in the specific heat capacity (c_p) of the glass with temperature. Fig 3.6 shows a result from the study by Giordano et al. (2005) for determining the T_g using a calorimetry method. When the transition from glass to liquid is reached there is a rapid increase in c_p. The glass transition is defined

as the temperature range between which c_p deviates from the glassy state and the temperature at which c_p is in a constant state, and from this two definitions of T_g are obtained (Giordano et al., 2005). First, is $T_{g\ peak}$, which is the temperature at which c_p is at the highest value. The second is $T_{g\ onset}$, which is intersecting the extrapolations of the gradual c_p in the glassy state and the tangent of the increase in c_p during the glass transition interval.

Calorimetry studies have shown that the value of T_g is influenced by the heating/cooling rate. Slower cooling rates create a longer effective structural relaxation timescale and therefore lower T_g (Dingwell and Webb 1989; Giordano et al. 2005)

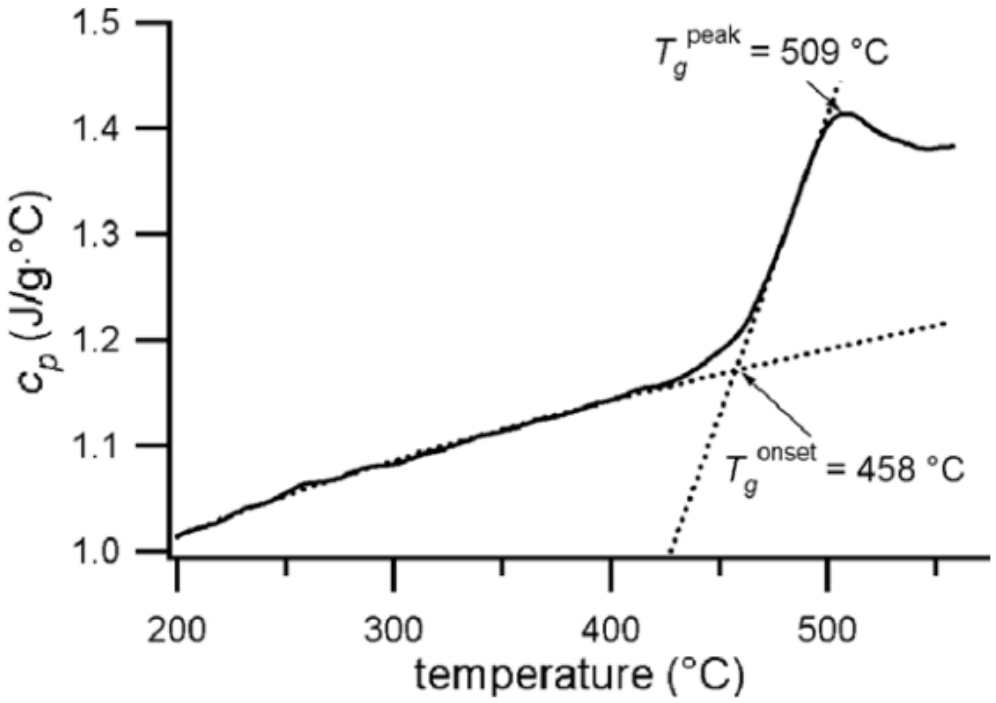

Figure 3.6: Determination of T_g using a calorimetry method. Figure from Giordano et al. 2005.

3.6.2 Controls on glass transition temperature

T_g is affected by quench rate, with T_g being higher for faster quench rates and lower for slow quench rates. Like viscosity, T_g varies with composition including volatile content. Volatiles dissolved in the melt can alter the structural relaxation timescale of the melt, resulting in an increase of volatile decreasing T_g (Giordano et al. 2005).

3.7 Solubility

Solubility is the property of a substance that can be dissolved in a solvent at equilibrium. For this project the solvent is the silicate melt and the solute is H_2O and CO_2 species. If the silicate melt is over-saturated with the volatile then two phases, (melt and fluid) exist in equilibrium. The term fluid is used since many temperature and pressure conditions relevant to volcanology will be above the critical point (Barker and Alletti, 2012). Henry's Law quantifies the solubility of a gas in a solvent and shows that at a fixed temperature the solubility of a gas is proportional to its partial pressure:

$$C = k\, P_{gas} \qquad \text{Eq. 3.9}$$

where C is the concentration in the solvent, P_{gas} is the partial pressure of the gas, and k is Henry's Law constant, which depends on the solvent, temperature and gas.

3.7.1 H_2O solubility in silicate melt

Due to the non-unity stoichiometric coefficient for OH in Eq. 3.1 and H_2O speciation, the dependency of H_2O solubility on pressure is non-Henrian (Zhang et al. 2007). The solubility of total H_2O can be written as;

$$X_{H_2O_t} = \frac{X_{OH}}{2} + X_{H_2O_m} \quad \text{Eq. 3.10}$$

where X denote mole fractions of the dissolved species in the melt. From the gas-liquid equilibrium of H_2O (gas) ⇌ H_2O (melt) and assuming ideal gas behaviour for the gas phase and ideal mixing in the melt, $X_{H_2O_m}$ is proportional to P_{H_2O}. X_{OH} is proportional to square root of $X_{H_2O_m}$ (Eq. 3.2) and therefore is proportional to $\sqrt{P_{H_2O}}$. The solubility of H_2O_t in silicate melt depends on pressure as;

$$X_{H_2O_t} = k_1\sqrt{P_{H_2O}} + k_2 P_{H_2O} \quad \text{Eq. 3.11}$$

where the first term on the right-hand side of the equation results from OH groups and the second term results from H_2O_m (Zhang et al. 2007). According to Eq. 3.11 at low pressures the dissolved H_2O_t is low and OH will be the dominant species. As pressure increases, H_2O_t also increases, whereby the proportion of H_2O_m will increase. As H_2O_m species becomes more dominant, H_2O_t solubility will begin to increase more rapidly than if it continues to follow a square root dependency on pressure (Zhang et al. 2007).

3.7.2 CO_2 solubility

For CO_2 although there are also two species like H_2O, it is more simple as the concentration of the two species are simply proportional to each other (Eq. 3.3). Therefore the solubility of CO_2 follows Henry's law (Eq. 3.9), (Zhang and Ni, 2010).

3.7.3 H_2O-CO_2 solubility

Silicate melt is unlikely to be in equilibrium with a fluid consisting of a single volatile species. The presence of additional volatile species would lower the

solubility of H_2O compared to a melt that is in equilibrium with a pure H_2O fluid (Barker and Alletti, 2012). Experimental studies have shown that H_2O solubility can be assumed to be independent of CO_2 concentration, for pressures below 400 MPa (Blank et al. 1993). However, addition of CO_2 gas lowers the concentration of H_2O in a melt by diluting the H_2O vapour phase (Lowenstern 2001).

For rhyolitic melts the model VolatileCalc by Newman and Lowenstern (2002), can model the solubility of mixed H_2O-CO_2 fluids in different composition, pressure and temperature conditions (Fig 3.7). The VolatileCalc model is valid for $\leq$ 11 wt% H_2O_t and 10,000 ppm CO_2, pressures of $\leq$ 500 MPa and temperature in a range of 600 – 1500 °C.

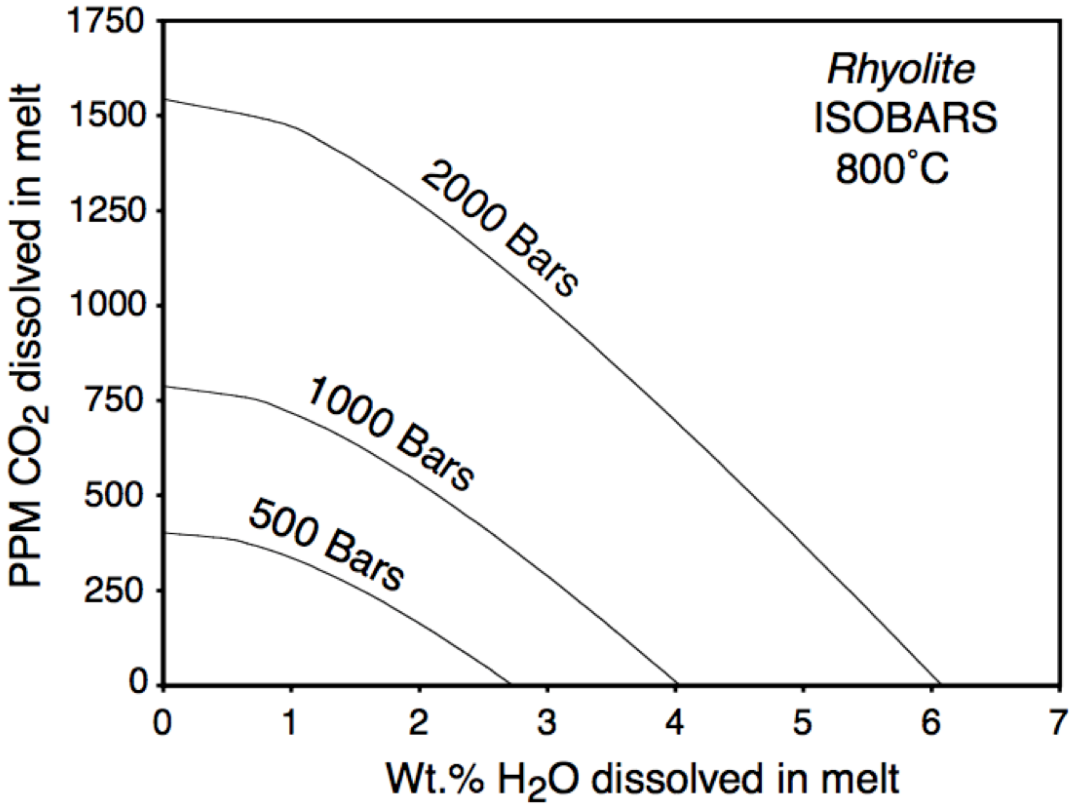

Figure 3.7: Example of pressure estimates from VolatileCalc. Isobars represents range of values for dissolved H_2O and CO_2 in rhyolitic melt in equilibrium with H_2O-CO_2 gas at 800 °C and selected pressures. Figure from Newman and Lowenstern (2002).

3.8 Diffusion

Diffusion occurs as a result of the thermally activated random motion of particles such as atoms, ions or molecules, which leads to a net flux of particles when the concentration of a component is not uniform (Zhang and Ni, 2010). This net flux is described by Fick's first law:

$$J = -D\frac{\partial C}{\partial x} \qquad \text{Eq. 3.12}$$

where J is the diffusive mass flux (a vector), D is the diffusion coefficient (m^2/s), C is concentration in units of mass per unit volume and $\frac{\partial C}{\partial x}$ is the concentration gradient (a vector). The negative sign indicates that flux moves from high to low concentration. Therefore, large concentration gradients are associated with large diffusive fluxes.

To understand how a concentration profile will evolve, the relationship between concentration, space and time is necessary. The general equation for one-dimensional diffusion is given by Fick's second law as;

$$\frac{\partial C}{\partial t} = \frac{\partial}{\partial x}\left(D\frac{\partial C}{\partial x}\right) \qquad \text{Eq.3.13}$$

where t is time, x is distance, D is constant.

3.8.1 Diffusion of H_2O

As already discussed, H_2O is present in the melt as both H_2O_m and OH whose proportions vary according to the equilibrium interconversion reaction (Eq. 3.1). Fick's second law can be modified to give the diffusion of H_2O_t as the sum of the diffusion of each species (Zhang and Ni, 2010):

$$\frac{\partial X}{\partial t} = \frac{\partial}{\partial x}\left(D_{H_2O_m}\frac{\partial X_{H_2O_m}}{\partial x} + \frac{1}{2}D_{OH}\frac{\partial X_{OH}}{\partial x}\right) \qquad \text{Eq. 3.14}$$

where $X_{H_2O_m}$ is the mole fraction of H_2O_m, X_{OH} is the mole fraction of OH and $D_{H_2O_m}$ and D_{OH} are the diffusivities of H_2O_m and OH. The factor of $\frac{1}{2}$ accounts for the 2 mol of OH that are produced with every 1 mol of H_2O_m (Eq. 3.1).

Shaw (1974) carried out the first experimental study on H_2O diffusion. Shaw (1974) investigated the mass gain of obsidian melt during hydration and concluded that H_2O_t diffusivity ($D_{H_2O_t}$) is dependent on the concentration of H_2O_t. The next major advance in H_2O diffusion study was the development of infrared spectroscopy, which allowed the microanalytical determination of the concentration of H_2O_t and the two species, H_2O_m and OH (Stolper 1982, Newman et al. 1986). Zhang and Stolper (1991) measured H_2O_m and OH concentration profiles in experimentally dehydrated obsidians. The results of the experimental profiles show that D_{OH} is much slower than $D_{H_2O_m}$ and $D_{H_2O_m}$ is roughly the same as for $D_{H_2O_t}$. This suggests that for H_2O_t, H_2O_m is the mobile species and OH is immobile (Zhang and Stolper 1991; Zhang et al. 2007), essentially the diffusion of H_2O_m is controlling the diffusion of H_2O_t. Therefore, OH concentration profiles are formed indirectly by diffusion of H_2O_m and then the conversion of H_2O_m to OH via Eq 3.1. The results of the difference in diffusivity may be explained by H_2O_m being a small, neutral molecule that can move relatively easily whereas the OH groups are bounded to a cation and therefore cannot move easily (Zhang and Stolper 1991).

3.8.2 Diffusion of CO_2

The diffusitivity of CO_2 does not depend on its own concentration and is roughly independent of the anhydrous melt composition. Diffusitivity of CO_2 in melts are expressed by the following (Zhang et al. 2007):

$$lnD_{CO_2t}^{all\ melts} = -13.99 - \frac{17367+1944.8P}{T} + \frac{(855.2+271.2P)}{T} C_w \qquad \text{Eq. 3.15}$$

where D is in m^2/s, T is in K, P is in GPa, and C_w is the wt% of H_2O_t.

3.8.3 Comparison of CO_2 and H_2O diffusivities

$D_{H_2O_m}$ is greater than $D_{CO_{2t}}$, and $D_{H_2O_t}$ is usually greater than $D_{CO_{2t}}$. This can be explained by the size of the molecules, where the effective radius of H_2O_m is smaller than the effective radius of CO_{2m}.

The diffusion of H_2O and CO_2 shows similarities and distinctions. In both H_2O and CO_2, speciation plays an important role where the neutral species (H_2O_m and CO_{2m}) is the dominant diffusing species and diffusivity of these species increases with H_2O_t. The major differences are that H_2O speciation results in $D_{H_2O_t}$ that depends strongly on H_2O_t. CO_2 speciation results in CO_2 diffusivity that is independent of CO_{2t} (Zhang and Ni 2010).

3.9 Bubbles in melt

3.9.1 Bubble formation

Formation of bubbles occurs when volatiles dissolved in a melt become over-saturated and exsolve to form a gas phase. Bubble formation may occur when there is a change in pressure and/or temperature in the melt causing the equilibrium solubility value to fall below the concentration of volatiles dissolved in the melt, or when there is addition of volatiles to the melt, which increases the concentration of dissolved volatiles above the equilibrium volatile solubility of the system (Mourtada-Bonnetoi and Laporte, 1999; Mangan and Sisson, 2000). In volcanism, a decrease in the confining pressure of the system caused by magma ascent or magma depressurisation results in a reduction in the amount of volatiles that can be dissolved in the magma and they exsolve to form bubbles. Bubble formation can also occur with growth of anhydrous (H_2O deprived) crystal phases. This increases the concentration of H_2O dissolved in the remaining melt and can drive them above the equilibrium solubility value.

Bubble formation can occur by homogeneous and/or heterogeneous nucleation. Homogenous bubble nucleation is the nucleation of a bubble in a crystal and bubble free melt. Homogeneous nucleation may therefore require oversaturation pressures of up to 200 MPa (Mourtada–Bonnetoi and Laporte, 1999). Heterogeneous nucleation occurs in the presence of a nucleation sites such as a crystal, microlite, inclusion or xenolith. Heterogeneous bubble nucleation is more efficient and does not require as high supersaturation pressures (only ~5 MPa) (Gardner et al. 1999).

3.9.2 Bubble growth

Bubble growth is controlled by both depressurisation and exsolution (Proussevitch and Sahagian, 1996). Depressurisation contributes to bubble growth by oversaturation of the melt in volatiles and a decrease of the density of the volatiles. Volatiles diffuse into bubbles if the melt is oversaturated due to depressurisation, increase of temperature or changes in the composition. During bubble growth, volatile concentrations at the bubble wall will be the equilibrium volatile solubility value for the current local pressure and temperature conditions. Away from the bubble wall the melt will contain more volatiles than the new equilibrium solubility value. As a result, volatiles will diffuse down a concentration gradient towards the bubble wall and into the bubble (McIntosh et al. 2014). Thus, if a bubble is growing, the volatile concentration decreases towards the bubble wall (Fig 3.8b, McIntosh et al. 2014).

3.9.3 Bubble resorption

During bubble resorption the volatile concentration at the bubble wall will increase above the concentration of volatile dissolved in the melt due to a decrease in the equilibrium volatile solubility caused by an increase in pressure and/or decrease in temperature (Fig 3.8C). This transfer of volatiles back into the melt will cause the bubble to shrink (Watkins et al 2012; McIntosh et al 2014) and volatiles will diffuse down a concentration gradient away the bubble wall and into the melt (McIntosh et al. 2014).

Studies have investigated bubble resorption in magmatic melts. Yoshimura and Nakamura (2008) have shown that bubble resorption can occur in an open degassing scenario by holding vesicular melt in an apparatus that maintains a pressure difference between the melt and the exterior. In higher-pressure sample chambers, H_2O gas is capable of escaping, and so H_2O was lost by diffusion from sample margins resulting in the resorption of bubbles along the margins. Bubble resorption was also investigated in a H_2O-CO_2 system (Yoshimura and Nakamura, 2010). A H_2O-rich melt containing bubbles of H_2O was surrounded by a pure CO_2 fluid, and bubbles were seen to shrink initially as fast-diffusing H_2O moved from the melt into the surrounding fluid and H_2O moved from the bubbles into the melt to maintain equilibrium. CO_2 moved from the fluid into the melt and ultimately into the bubbles, however due to the slower timescale of CO_2 diffusion temporary bubble resorption occurred.

Bubble resorption in magmatic contexts have been attributed to an increase in pressure causing resorption. H_2O concentration profiles around bubbles in obsidian pyroclasts from Mono Craters, California (Watkins et al. 2012), shown that bubbles were resorbing prior to the glass transition. Watkins et al. (2012) interpreted this as evidence of pressure increase cycles in the conduit prior to eruption.

Second study of bubbles resorption been attributed to an increase in pressure by Carey et al. (2013) have also observed in direct evidence of bubble resorption in

basaltic pyroclasts from explosive lake eruption in Kilauea, Hawaii. H_2O concentrations in the samples were too low to analyse but the bubble resorption was inferred with a halos consisting of small bubbles surrounding a large bubble. This texture is thought to represent bubbles which had begun to resorb as they sank during conduit convection. This causes an increase in pressure. During pressure decrease caused by either as a result of further convection of eruption, the H_2O-rich melt surrounding the partially resorbed bubble became supersaturated and nucleated a secondary bubble population.

Bubble resorption has also been attributed to cooling of the magmatic melt. McIntosh et al. (2014) have shown if resorption is caused by temperature decreases during quench, previous growth history maybe preserved. Speciation data indicate that the H_2O_m distribution records resorption, while the OH distribution records earlier decompressive growth.

If a bubble is not growing or shrinking it is in equilibrium with the melt, and the volatile concentration in the surrounding melt is constant throughout from the bubble wall (Fig 3.8a).

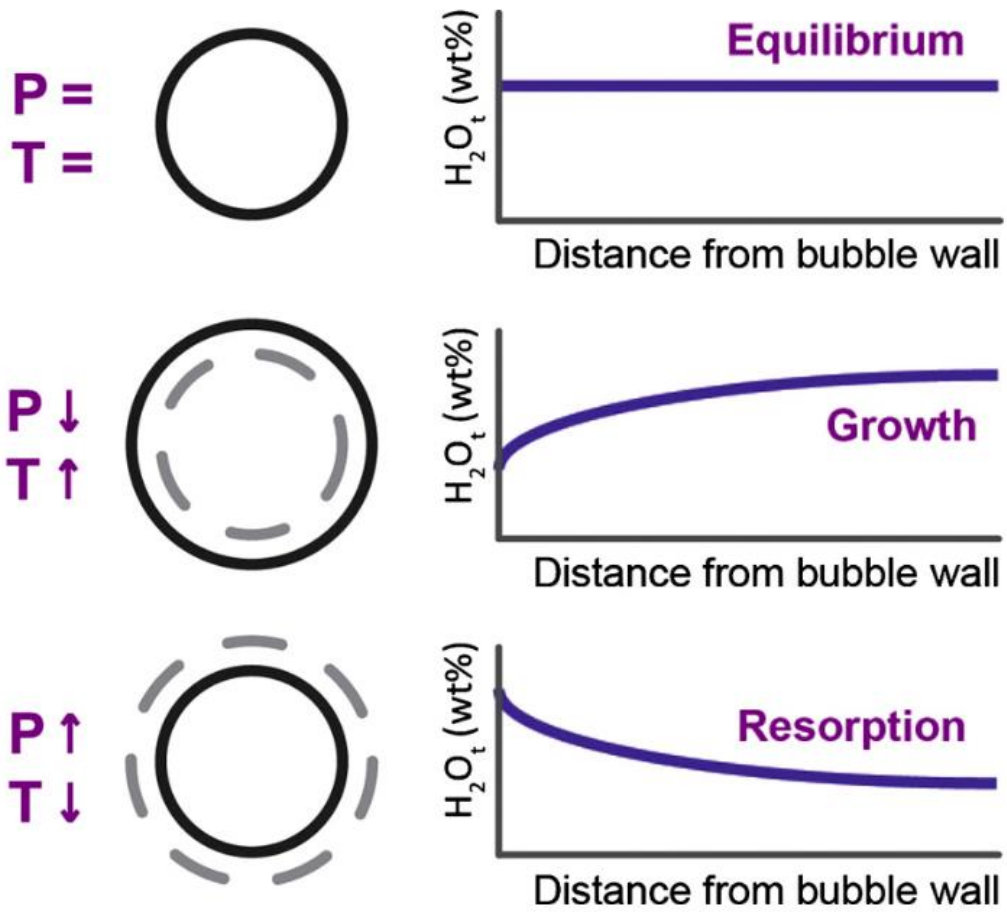

Figure 3.8: Schematic figure linking the pressure and temperature conditions, state of bubble growth and associated concentration profiles in the melt. Solid black lines indicate current bubble size; dashed grey lines represent the previous bubble size. Figure from McIntosh et al. 2014.

3.10 Summary

Many experiments have been carried out investigating many aspects of magmatic volatiles and its influence of the melt and bubble property. This project will look at the evolution of the magmatic H_2O and CO_2 from the Krafla glass cuttings in response to the unexpected interception by the IDDP-1 drill. Chapter 4 discusses analytical techniques used to achieve an understanding of the insights of the H_2O and CO_2 content of the Krafla melt and also it's melt properties.

Chapter 4: Analytical methods and data production

4.1 Introduction

This chapter provides an overview of how the samples were analysed, and the methodologies used to produce the data presented in Chapters 4 and 5. For this project Fourier transform infrared spectroscopy (FTIR) was used to measure volatile elements, H_2O and CO_2, dissolved in the glass and electron probe microanalysis (EPMA) was used to measure major element compositions of the glass.

4.2 FTIR measurements of magmatic H_2O and CO_2

H_2O and CO_2 concentrations in the Krafla glass cuttings were analysed by FTIR. As well as total H_2O (H_2O_t) and CO_2 (CO_{2t}) concentrations, FTIR can determine the speciation of H_2O (i.e., the amount of H_2O present as molecular H_2O, H_2O_m, versus hydroxyl, OH, groups) and CO_2 (i.e., the amount of CO_2 present as molecular CO_2, CO_{2m}, versus carbonate, CO_3^{2-}, groups) (see Chapter 3 section 3.3). H_2O speciation data can be used to investigate the magmatic conditions immediately prior to quenching, including species gradients resulting from pressure changes (e.g., Watkins et al., 2012; Carey et al., 2013), temperature changes (e.g., McIntosh et al., 2014), and post-quenching hydration (e.g., Dixon et al. 1995; Anovitz et al. 2008; McIntosh et al. 2017). FTIR results will therefore help to establish the evolution of magmatic volatiles caused by the magma being intersected by drilling during IDDP-1.

4.2.1 Principle

FTIR is a non-destructive technique and can resolve H_2O and CO_2 concentrations ranging from a few ppm to several wt % (Newman et al. 1986). In FTIR, infrared (IR) radiation is passed through a glass sample of known thickness. As the radiation passes through the sample it interacts with the molecular species present in the glass, triggering transitions in the molecular vibrations of covalent bonds (Stolper 1982). These transitions absorb the wavelength of IR radiation that corresponds to the frequency of the molecular vibration (Stolper 1982; Newman et al. 1986). Different bonds have different molecular vibration frequencies and hence absorb different wavelengths of IR radiation. This allows identification of the specific molecular species present in the samples. These absorption values can be converted into concentrations using the Beer-Lambert law;

$$c = \frac{M.A}{\rho.d.\varepsilon} \times 100 \qquad \text{Eq. 4.1}$$

where c is the concentration of species of interest (wt.%), M is the molar mass of H_2O or CO_2 (g.mol^{-1}), A is the absorbance of the species of interest, the height of the peak above background (unitless), ρ is the density of the sample (kg.m^{-3}), d is sample thickness (cm) and ε is the molar absorptivity for the absorbance band of interest (l.mol^{-1}.cm^{-1}) (Stolper 1982, Newman et al. 1986).

FTIR is especially useful for identifying H-O species as the bonds are highly polarised and therefore are efficient absorbers of IR radiation (Della Ventura et al. 2010). Several different absorption bands exist for the H_2O species (Fig 4.1):

- In the near infrared (near-IR) region (wavenumbers 14000-4000 cm^{-1}), absorption bands for H_2O exist at ~7100, ~5200, ~4500 and ~4000 cm^{-1}, of which the 5200 and the 4500 cm^{-1} bands are the strongest and were used in this study. The 5200 cm^{-1} band is attributed to the bending and stretching of H_2O_m (Scholze 1960; Bartholomew et al. 1980). The 4500 cm^{-1} band is attributed to combination modes of Si-OH and Al-OH groups (Stolper 1982). The weaker absorbance band at 7100 cm^{-1} is a first

overtone of the O-H stretching, and the origin of the 4000 cm^{-1} band is not fully understood (Bartholomew et al. 1980; Newman et al. 1986).

- In the mid infrared (mid-IR) region (4000-400 cm^{-1}) the bands related to H_2O exist at ~3500 and ~1630 cm^{-1}. The 3500 cm^{-1} band is broad and asymmetric, and attributed to the fundamental OH stretching of both H_2O_m and OH. The shape of the band reflects the distribution of H-bond strength within the glass. The 1630 cm^{-1} is symmetric and is attributed to the fundamental bending mode of H_2O_m (Nakamoto 1978). The absorption bands for CO_2 exist at ~2350 and at a doublet peak at ~1515 and ~1435 cm^{-1}. The 2350 cm^{-1} band is related to the antisymmetric stretching mode of CO_{2_m} (Newman et al. 1986, Stolper et al. 1989). The doublet is attributed to a doubly degenerate asymmetric stretching of CO_3^{2-}.

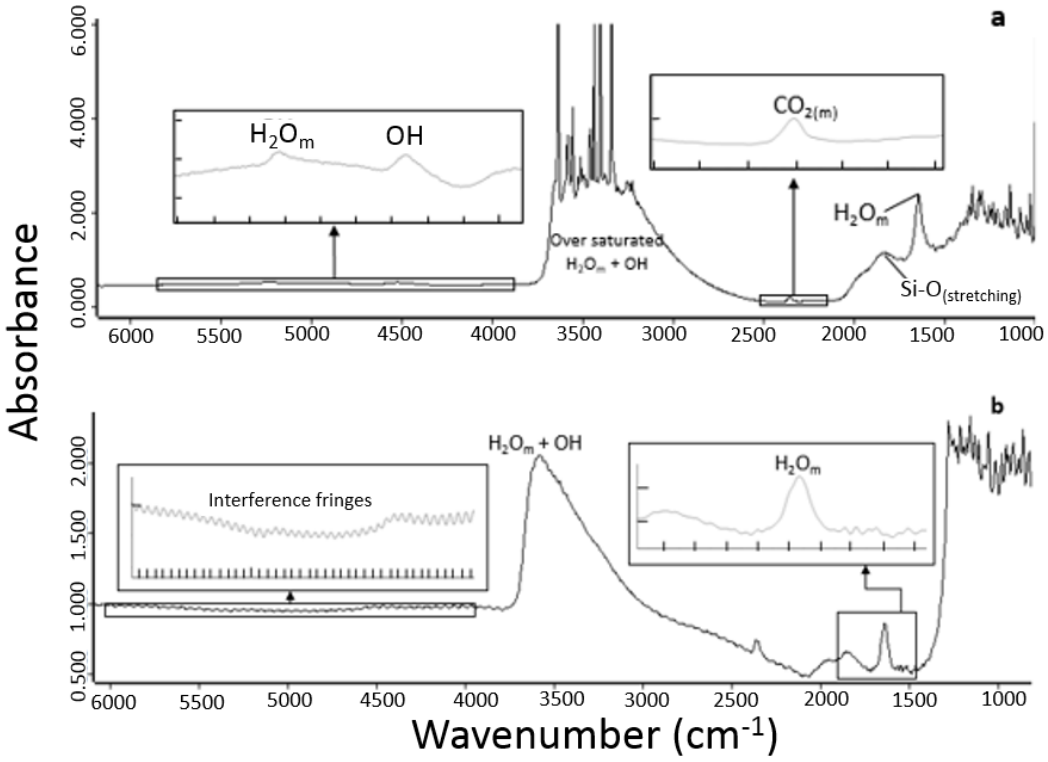

Figure 4.1: Representative spectra showing the positions of the volatile absorption bands in the near-IR (A) and mid-IR (B). The bands in the near-IR are weaker and hence require thicker samples in order to be amplified.

4.2.1.2 Synchrotron radiation FTIR

Synchrotron radiation Fourier-transform infrared spectroscopy (SR-FTIR) produces a much brighter light than conventional globar sources (von Aulock et al. 2014), resulting in a higher signal to noise ratio even when using small aperture sizes. A synchrotron source not only emits powerful light but also delivers the light at a smaller range of incidence angles, meaning less light is blocked by the aperture. These features allow significantly higher spatial resolution and spectra with higher signal-to-noise ratios, enabling H_2O and CO_2 gradients to be measured in greater detail, their concentrations to be measured with greater accuracy, and their detection limits to be reduced.

4.2.1.3 Focal Plane Array Detectors

Focal plane array detectors (FPA) consist of multiple channel detectors (Miller and Smith, 2005; von Aulock et al. 2014). All individual detector elements on the FPA simultaneously measure the absorbance of the spectral range of the system (Miller and Smith 2005). As a result, maps of absorbance over a large area can be created in a relatively short time. However, while FPA analyses are ideal for making large absorbance maps, the signal to noise ratios are lower than those from a synchrotron sourced FTIR due to the weaker light source, making smaller peaks harder to resolve. The spatial resolution of FPA is not only limited by the pixel size but also by signals off the focal plane as FPA are not confocal. Currently, FPA is not routinely used with a synchrotron source because of the difficulty in setting the FPA detector up on the synchrotron beamline and artefacts that appear in the image that are most apparent when tiling images and may be produced by sample specific scattering (or diffraction) and/or coherence speckle noise (von Aulock et al. 2014).

4.2.2 Sample preparation

For this project, we want to understand how the magmatic volatiles evolved and what that can tell us about how the magma responded to being intercepted by the IDDP-1 drilling project. To achieve this, 18 glass cuttings recovered from the IDDP-1 borehole at different times were selected for analysis and detailed mapping using synchrotron-sourced FTIR and the FPA at the infrared microspectroscopy beamline of the Australian Synchrotron (AS). Mapping consisted of measuring and displaying H_2O and CO_2 distributions around a feature, such as bubbles in the glass.

The samples were chosen to best represent the evolution of the magma body. At each time interval a sample that exhibited the most common texture was selected (See chapter 2 section 2.5.1 on the textural details of the glass cuttings). At time intervals with a mixture of textures, multiple samples (up to 4 glass cuttings) with different textures were selected.

4.2.2.1 Target sample thickness

Measurements of both H_2O and CO_2 were desired and therefore the samples needed to be prepared to a thickness that allowed the relevant vibrational bands to be detected. The aim was for each glass cutting to be analysed twice in the FTIR as thick and thin samples. Thick samples would allow H_2O_m and OH to be detected in the near-IR and CO_2 to be detected at the 2350 cm^{-1} band. The thin samples would allow measurements of the H_2O peaks in the mid-IR region, because H_2O peaks in the mid-IR are stronger than the peaks in the near-IR. Larger peaks are more desirable as they are easier to measure. However, if the samples are too thick all the radiation at that wavenumber is absorbed and no radiation reaches the detector, so the peak will no longer be proportional to concentration and thickness (von Aulock el. 2014). On the absorbance FTIR spectra this appears as a noisy peak that is cut off (Over saturated H_2O_m + OH;

Fig 4.1a). Thicker samples will also increase the likelihood of the beam hitting bubbles or crystal, which would interfere with the results.

To achieve the desired peak heights in the near-IR, concentrations of H_2O and CO_2 measured in the IDDP-1 glass cutting by Zierenberg et al. (2013) were used to estimate target sample thicknesses by rearranging (Eq. 4.1):

$$d = \frac{M.A}{\rho.c.\varepsilon} \times 100 \qquad \text{Eq. 4.2}$$

Zierenberg et al. (2013) used molar absorption coefficient values of 1.86 $l.mol^{-1}.cm^{-1}$ for H_2O_m and 1.5 $l.mol^{-1}.cm^{-1}$ for OH (from Ihinger et al. 1994), and 1214 $l.mol^{-1}.cm^{-1}$ for molecular CO_2 (from Behrens et al. 2004). A density value of 2350 $kg.m^{-3}$ for rhyolite (Stevenson et al. 1994) was used. H_2O_m and OH concentrations provided by Zierenberg et al. (2013) are 0.60 ± 0.11 wt%, and 1.08 ± 0.09 wt%, respectively; CO_2 concentration is 85.08 ± 15.07 ppm. The desired minimum absorbances of the 5200 cm^{-1} and the 4500 cm^{-1} bands are 0.05, and 0.1 for the CO_2 band at 2350 cm^{-1}.

Using the above absorbance values, the minimum required wafer thickness for optimum results for the near-IR peaks and 2350 cm^{-1} (CO_2) peak was estimated to be between 200 to 250 μm. Table 4.1 summarises the values of each parameter from the Beer-Lambert law (Eq. 4.1) used in the thickness calculations.

Table 4.1: Parameter values from Zierenberg et al. (2013), which was used to calculate the required sample thickness for the near-IR and the CO_2 band.

Parameter	H_2O_{mol}	OH	CO_2	Units	Reference
$c_{average}$	0.6	1.17	85.08	wt%, ppm	Zierenberg et al. 2013
$c_{minimum}$	0.49	1.08	70.01	wt%, ppm	Zierenberg et al. 2013
$c_{maximum}$	0.7	1.26	100.15	wt%, ppm	Zierenberg et al. 2013
ρ	2350	2350	2350	kg.m^{-3}	Stevenson et al. 1994
A	>0.05	>0.05	>0.1	unitless	-
M	18.02	18.02	44.01	g/mol	-
ε	1.86	1.5	1214	l.mol^{-1}.cm^{-1}	Ihinger et al. 1994 (H_2O); Behrens et al., 2004 (CO_2)

For measurements in the mid-IR, the samples were thinned to prevent too much absorbance and cut-off of the peaks (Fig. 4.1b). A maximum target thickness for each sample was calculated after the samples had been analysed in the near-IR region. When the values for concentration and molar absorptivity coefficient are known, the thickness can be directly calculated for each sample. Therefore, unlike the near-IR thickness calculations, the sample-specific H_2O_m and OH concentrations measured by the preceding near-IR analyses can be used as input in the calculations of the thickness required for analysis of H_2O peaks in the mid-IR region (more detail of concentration calculation in section 4.2.4).

Newman et al. (1986) show that the molar absorptivity coefficient for the 3500 cm^{-1} band depends on H_2O speciation:

$$\varepsilon 3500 = X_{OH}\varepsilon 3500_{OH} + X_{H_2O_m}\varepsilon 3500_{H_2O_m} \qquad \text{Eq. 4.3}$$

where X_{OH} and $X_{H_2O_m}$ are the mass fractions of water dissolved as OH and H_2O_m respectively. Newman et al. (1986) calculated that if all H_2O is present as H_2O_m the molar absorptivity for the 3500 cm^{-1} band is 56 l.mol^{-1}.cm^{-1} ($\varepsilon 3500_{H_2O_m}$), and if all H_2O is present as OH it is 100 l.mol^{-1}.cm^{-1} ($\varepsilon 3500_{OH}$). The molar

absorptivity used for the 1630 cm^{-1} band was 55 $l.mol^{-1}.cm^{-1}$ (Newman et al., 1986).

The density value used for the target thickness calculation was the same, 2350 $kg.m^{-3}$ (Stevenson et al. 1994).

Based on the near-IR H_2O species measurements, target thickness for the samples ranged from 40 to 60 μm to produce the desired peaks. Table 4.2 summarises the parameters needed to calculate the maximum target thickness for the mid-IR analysis.

Table 4.2: Parameter values required to calculate the thickness for the thin samples.

Parameter	H_2O_m + OH ($3500cm^{-1}$)	H_2O_m (1630 cm^{-1})	Units	Reference
C	from near-IR for each sample	from near-IR for each sample	wt%	-
ρ	2350	2350	$kg.m^{-3}$	Stevenson et al. 1994
A	>0.1	>0.1	unitless	-
M	18.02	18.02	g/mol	-
ε	speciation dependent (77.6 – 147.8) (Eq. 4.3)	25	$l.mol^{-1}.cm^{-1}$	Newman et al. 1986

4.2.2.2 Doubly polished sample wafer preparation

A major challenge in using FTIR is preparing samples (von Aulock et al. 2014), since thin, doubly polished unsupported wafers are needed. This can be difficult for very small or fragile samples, and hence limits the samples that can analysed. Variations of sample thickness can cause major errors in the volatile calculation from FTIR measurements. The measured values are directly proportional to both

the thickness and volatile content of the glass. Therefore the accuracy of the thickness measurements is often the biggest limitation to the accuracy of quantitative measurements, especially in the case of very thin samples.

Preparation of wafers of thick samples was undertaken in the Department of Geological Sciences, University of Canterbury. Fig 4.2a illustrates the series of processes that were followed in preparing the samples. Preparation started by mounting a chip of the glass cuttings onto a glass slide using the adhesive Crystalbond™ 509. Crystalbond™ 509 has a relatively low melting temperature, ~121 °C, and is soluble in acetone, allowing it to be easily removed from the sample when desired. This enables easier handling of samples during preparation. Mounted samples were polished using silica carbide grinding paper with a grade of P1200 and then P2000 to achieve a flat surface, before final polishing using diamond paste of 3 μm followed by 1 μm on a polishing disc. After polishing, the sample was turned over and remounted in Crystalbond™ 509 so that the other side could be ground and polished in the same way to the target thickness. The two surfaces were prepared parallel to avoid thickness variations across the samples. Sample thickness was checked throughout the grinding and polishing of the second surface while the sample was mounted on the glass slide using a digital indicator micrometer. This ensured the target thickness was reached and ensured variations across the samples were minimised. Finally, the Crystalbond™ 509 was removed by placing the samples in an acetone bath and allowing the adhesive to dissolve. Once the Crystalbond™ 509 had dissolved, the sample was moved from the bath and left to dry, leaving a freestanding sample wafer for analysis. To reduce risk of damage during transport, all the samples prepared for near-IR and CO_2 analysis were transported mounted on the glass slide and removed just prior to analysis. Once analysed the freestanding wafer was stored in a gelatine capsule. Samples were handled using a paintbrush rather than tweezers to avoid breaking the samples.

Thin sample wafers for analysis of H_2O peaks in the mid-IR region were prepared from the thick wafers by grinding down and re-polishing one of the surfaces to the target thickness. This was undertaken at the Australian Synchrotron after the

thick wafers had been analysed. The thickness of the sample was checked throughout the grinding and polishing using a digital indicator micrometer. This ensured that the target thickness was reached and ensured thickness variation across the sample was minimised. Fig 4.2b illustrates the series of processes to prepare the thin samples from the thick samples

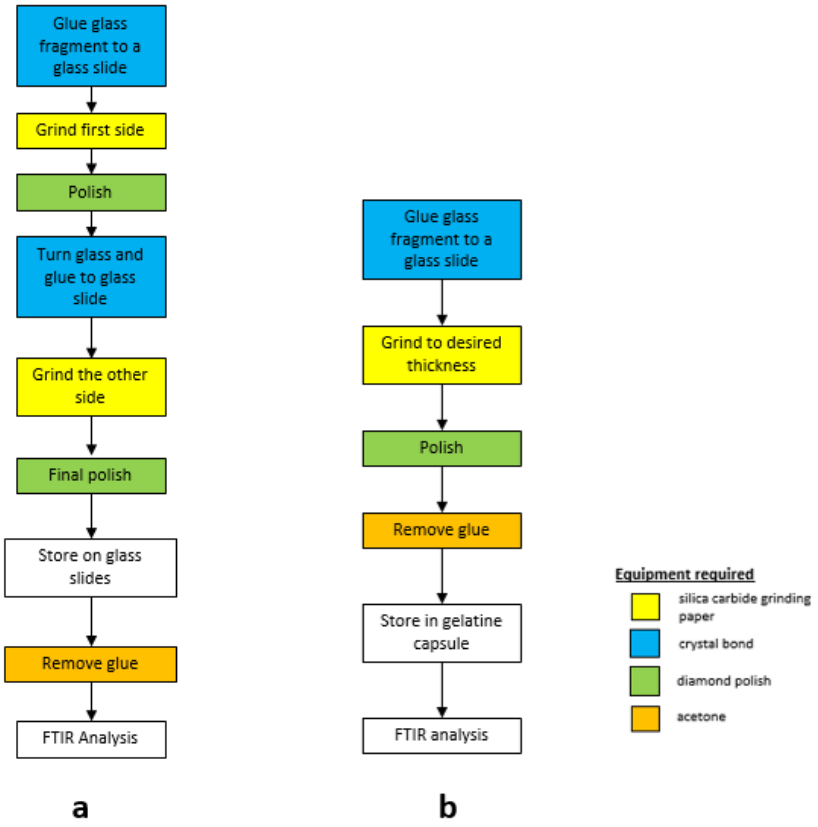

Figure 4.2: Schematic diagram showing the sample preparation process for a) the thicker samples and b) the thinner samples.

4.2.3 FTIR data collection

For this project, the infrared microspectroscopy beamline at the Australian Synchrotron (AS) was used for four days. Absorbance maps for both thick (~200 µm) and thin (~30-40 µm) samples were created using a Bruker Hyperion 2000 infrared microscope attached to a Bruker Vertex 80v spectrometer bench on the AS infrared microspectroscopy beamline. Maps were collected over 128 scans (background every 5 measurements) at a spectral resolution of 8 cm^{-1} using a

synchrotron source, an extended potassium bromide (KBr) beamsplitter, and a liquid-nitrogen cooled mercury cadmium telluride (MCT) detector. A pinhole of 0.2 μm were used to create a spatial resolution of 5.56 μm but by overlapping the spectra a spatial resolution for each maps is ~3 μm. Samples were placed inside a purge box under 19-20% humidity. In total, 44 maps were created for 19 thick samples, and 8 maps were created for 8 thin samples. The size of the maps for the thicker samples ranges from 40 x 40 μm, to 40 x 80 μm. The maps for the thinner samples ranged from 35 x 35 μm, to 50 x 50 μm.

During the time at the AS, 13 additional maps were created for 8 samples from spectral images using the offline (i.e., non-synchrotron source) Bruker Hyperion 3000 infrared microscope with focal plane array detector (FPA) attached to a Bruker Vertex 70 spectrometer bench. The images were collected over 256 scans with a spectral resolution of 8 cm^{-1}, using a conventional globar source, a KBr beamsplitter and the FPA detector (which had 64 by 64 channels covering 180 x 180 μm, giving a spatial resolution of 2.8 μm). The size of the maps compiled from the 180 x 180 μm FPA images range from 180 x 700 μm, to 720 x 720 μm.

4.2.4 FTIR data processing

The peaks analysed for the near-IR region were the 5200 cm^{-1} band for H_2O_{mol} and 4500 cm^{-1} for OH. The peaks analysed for the mid-IR were the 3500 cm^{-1} band for H_2O_t, 1630 cm^{-1} peak for H_2O_{mol} and the 2350 cm^{-1} peak for CO_2. In rhyolites total CO_2 is present as CO_{2_m} and CO_3^{2-} are not preserved (Chapter 3, section 3.2.2.2). The following describes how each parameter required in the Beer-Lambert law (Eq. 4.1) was established to calculate the concentrations of the Krafla glass cuttings.

4.2.4.1 Absorbance

Bruker's OPUS (v7.2, 2012) spectroscopy software for was used to determine the height above the baseline of each relevant peak. The integration command on OPUS was used to calculate peak heights at a given peak with a linear baseline fit (method R in OPUS).

4.2.4.1.1 CO2 absorbance

As expected, a single CO_{2_m} peak at ~2350 cm^{-1} was observed in the thicker samples. However, in the thin samples there is a double peak at ~2350 cm^{-1} in spectra collected by SR-FTIR (Fig 4.3). These doublets are always positive, with the higher wavelength peak (peak 1) absorbance value higher then the lower wavelength peak (peak 2). The difference between the two peaks heights tends to change with sample thickness, where the greatest absorbance differences are in the thinnest samples. In all thick samples, the location of the CO_2 single peak is in the trough of the two peaks in the thin samples (Fig 4.3). These doublets were only observed from thin samples measured by the SR-FTIR and are not observed in the FPA-FTIR analysis. Watkins et al. (2012) identified such doublet peaks at this wavenumber to be caused by gaseous CO_2 (CO_{2gas}). As bubbles were not in the beam path, it is presumed that CO_{2gas} would be in the atmosphere in which the measurement was conducted. However, measurements were conducted in a purge box under 19-20% humidity to ensure measurements were taken in a clean, dry atmosphere.

The following suggests that these doublet peaks are not caused from CO_{2gas} in the atmosphere surrounding the measurements;

1. The doublet peaks only appear in the spectra for the thin samples; in the thick samples the peak is a single peak indicative of dissolved CO_{2_m} (Watkins et al. 2012). Measurements of the thick and thin samples were conducted under the same conditions. If the CO_{2gas} were in the atmosphere surrounding the measurements it would be expected to be in both sets of measurements.

2. One possibility to explain the absence of the doublet in the thick samples is that the CO_{2_m} vibrations overwhelm those from the CO_{2gas}. However, the doublet peaks in the thin samples all have higher absorbance than the single peaks in the thicker samples (Fig 4.3).
3. The doublet peaks are always positive indicating that CO_{2gas} has increased between background and sample measurements. Background measurements were taken every five sample measurements. If there was CO_{2gas} leaking into the purge box during the measurement series the levels, and thus the doublet peak, would be expected to increase gradually throughout the measurement sequence. However, during the five sample measurements the absorbance of the doublet does not change. This suggests that the CO_{2gas} always increases after every background and then remains stable for five sample measurements before increasing again, but only after the next background. This seems hard to explain, unless the actual movement to conduct a background is causing some sort of leak. However, once again, why does this only affect the analyses of thin samples and not the thick samples?

Based on these observations, it seems more likely that these doublet peaks relate to something specific about the thin sample rather than CO_{2gas} in the atmosphere around the measurements because bubbles in the samples were avoided during data collection.

The causes of the double peak at ~2350 cm^{-1} in the thin samples are currently unknown. For the purpose of this project, the concentrations of CO_2 were taken from the peaks in the thick samples. This is because the peak is always positive and a single peak, indicative of CO_{2_m} dissolved in rhyolite (Watkins et al., 2012).

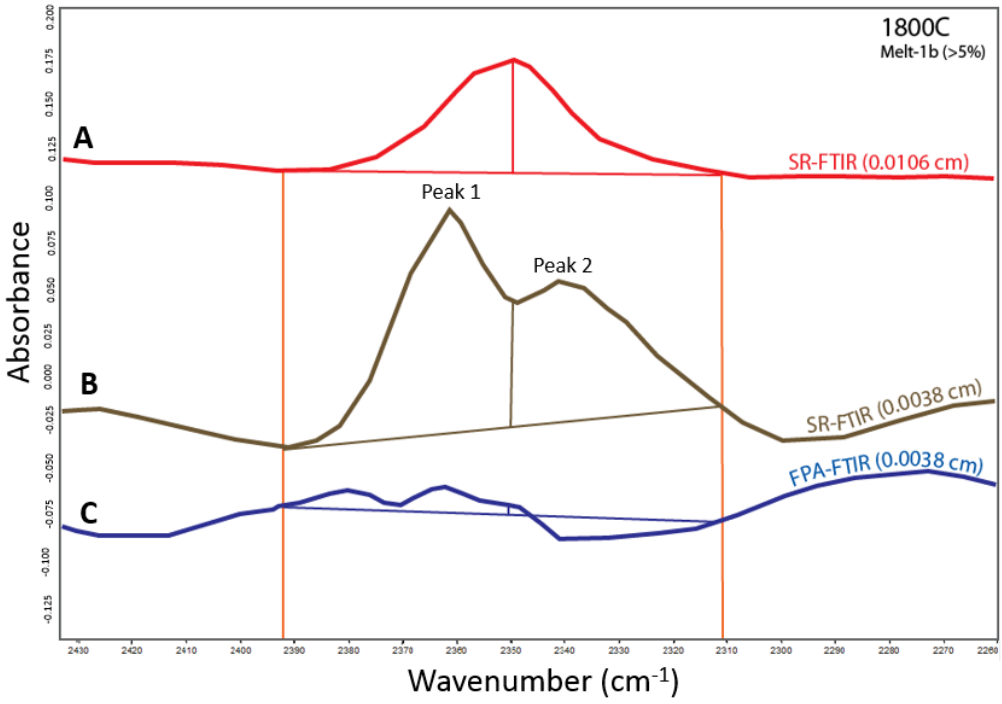

Figure 4.3: Variation of the CO_{2m} peak (~2350 cm^{-1}) between, A) the thick (106 μm) sample measured by the SR-FTIR (red), B) thin (39μm) sample measured by the SR-FTIR (brown) and C) a thin sample measured by the FPA-FTIR (blue). Spectra displaced along y-axis for clarity. All three peaks are from the same sample (1800C).

4.2.4.2 Sample thickness

Sample thickness is a major concern as it can introduce significant error to the volatile concentration calculations (von Aulock et al. 2014). Therefore, in addition to careful sample preparation, the sample thicknesses were determined at each spot using the following three methods:

A digital indicator, with a needle-tip contact point, mounted on a stand with a marble base was used to directly measure thickness. Placing the sample on the marble base and measuring the distance with and without the sample under the needle-tip and obtaining the difference was the simplest and quickest method to measure sample thickness. The digital indicator has an accuracy of 1 μm, however, it was difficult to be certain that the thickness was measured at precisely the same spot as the FTIR measurement was taken. Firstly, because the needle tip is larger than the analytical spot size, and secondly, as the needle was positioned by eye after the sample had been measured and transferred from the

infrared microscope, it was difficult to be certain that the thickness was measured at exactly the same spot as the analysis. There was also the danger of the needle tip breaking the sample.

Interference fringes were used to measure sample thickness from the thinner samples (Nishikida et al. 1996; Tamic et al. 2001; Wysoczanski and Tani, 2006; Nichols and Wysocazanki, 2007). Interference fringe patterns were seen as a regularly undulating background in the FTIR spectra of the thinner samples even in transmitted light (Fig 4.4). As sample thickness decreases, the amplitude and wavelength of the interference fringes increases. Nishikida et al. (1996) have shown that, in thin samples, the wavelength of the interference fringe pattern is directly proportional to the thickness and the refractive index of the sample:

$$t = \frac{m}{2n(v_1 - v_2)} \qquad \text{Eq. 4.4}$$

where t is the thickness of the analysed area (cm), m is the number of waves in the selected interval of wavenumbers (between v_1 and v_2), and n is the refractive index of the glass. For the Krafla glass a refractive index of 1.5 for rhyolite was used (Liu et al. 2005). Interference fringes in the region either side of the 2350 cm^{-1} band between 2000 and 2700 cm^{-1} were chosen, as this is a "clear" domain with no overlap with volatile peaks. Advantages of this method include a precision up to ±3 μm (Sun et al. 2007) and as the fringes appear on the FTIR spectra the thickness is calculated for the exact spot analysed. However, the limitation in estimating thickness by interference fringes is that it is only useful for samples that have been polished thin enough for the spectra to exhibit interference fringes (Nichols & Wysoczanski, 2007) and it requires knowledge of the refractive index of the sample.

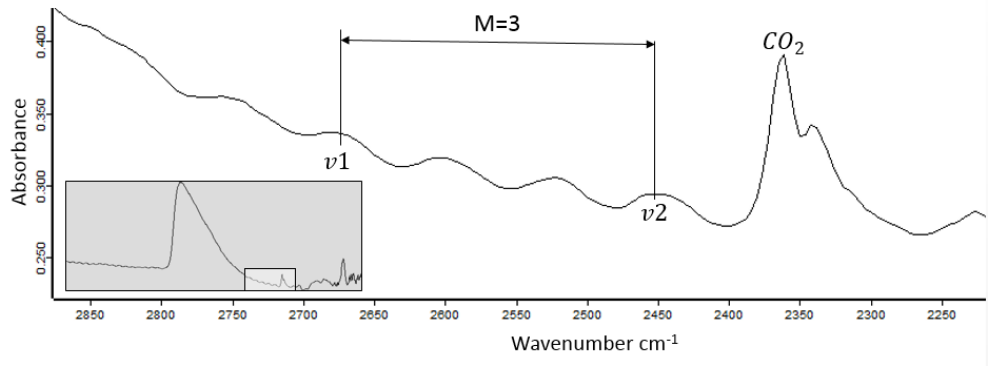

Figure 4.4: Representative spectra showing how the interference fringes are used to determine the thickness of the sample.

Another way to calculate thickness is by using the Si-O stretching on the 1830 cm^{-1} band. Miwa and Toramaru (2013) have shown a clear relationship between the peak intensity of the 1830 cm^{-1} band and the thickness of the samples (Fig 4.4). They also suggest that the volatile content in the glass does not appear to affect this relationship. Therefore, Miwa and Toramaru (2013) were able to calculate sample thickness using the following equation:

$$d = 0.034 \pm 0.0006 Abs_{1830} \qquad \text{Eq. 4.5}$$

where d is the thickness of the sample (cm) and Abs_{1830} is the absorption at the 1830 cm^{-1} band. However, this equation is for the specific composition in the Miwa and Toramaru (2013) study, and as the dependency of this relationship on composition has not yet been determined. It is thus not known if this constant applies to the composition of the IDDP-1 glass cuttings. In this project, the thicknesses of seven samples with a known analysis location were measured using the digital indicator and compared to the absorbance of the 1830 cm^{-1} band measured at the same location. This allowed a constant of 0.0304 ± 0.0008 to be calculated specifically for the Krafla samples (Fig 4.5) and hence the sample thickness at other locations was then estimated using the 1830 cm^{-1} absorption band measurements.

This method can only be done on the thick samples because the 1830 cm^{-1} does not appear in the thin samples. For this project, the thickness from the interference fringes and digital indicator measured thickness were not compared

due to the potential of breaking the fragile sample when using the digital indicator.

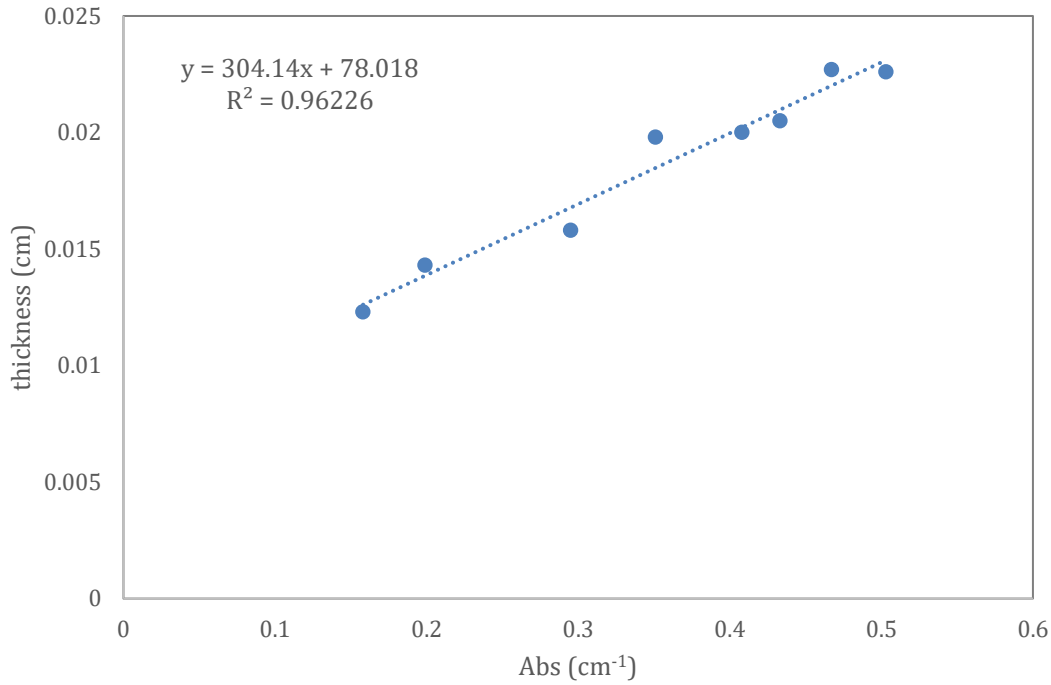

Figure 4.5: The relationship between glass thickness and the absorbance at 1830 cm^{-1} for the Krafla glass cuttings.

A major limitation of thickness estimations by the 1830 cm^{-1} peak is that the directly measured thickness used the digital indicator. As discussed above, the thickness will not be measured at precisely the same spot as the FTIR measurement was taken.

4.2.4.3 Density

Due to the very small sample size, it was too difficult to directly measure the glass density. Sample-specific glass density was calculated using major element data obtained by electron microprobe (section 4.3) and H_2O_t from FTIR using the model for silicate melts at high temperatures from Lange & Carmichael (1987) and Lange (1997), extrapolated to room temperature. Partial molar volumes were taken from Lange & Carmichael (1987) and Lange (1997), except for H_2O,

which was from Ochs and Lange (1997). For samples in which major elements were not analysed, a density of 2410 $kg.m^{-3}$ was used. This was the average density for all the samples that were analysed by the electron microprobe analysis.

4.2.4.4 Molar absorptivity coefficients

For the near-IR H_2O bands, the molar absorptivity coefficient used for the H_2O_{mol} band at 5200 cm^{-1} was 1.61 $l.mol^{-1}.cm^{-1}$ and 1.73 $l.mol^{-1}.cm^{-1}$ for the OH band at 4500 cm^{-1} (Newman et al. 1986).

The molar absorptivity coefficient used for the CO_2 band at 2350 cm^{-1} in the thick samples was 1214 $l.mol^{-1}.cm^{-1}$ (Behrens et al. 2004).

For the mid IR H_2O bands, the molar absorptivity coefficient used for the H_2O_{mol} band at 1630 cm^{-1} was 55 $l.mol^{-1}.cm^{-1}$ (Newman et al. 1986). For the 3500 cm^{-1} band the molar absorptivity coefficient depends on speciation according to Newman et al. (1986). However, the equation provided to calculate the molar absorptivity coefficient requires advance knowledge of the H_2O speciation (Eq. 4.3). Recently, McIntosh et al. (2017) present a new methodology that accounts for the species-dependence of the molar absorptivity coefficient for the 3500 cm^{-1} band without requiring advance knowledge of the species proportions. This enables accurate water species concentrations to be determined from the 3500 and 1630 cm^{-1} absorbance bands.

4.2.4.4.1 Species-dependent molar absorptivity coefficient for total H_2O at 3500 cm^{-1}

The equation that McIntosh et al. (2017) derive uses end-member molar absorptivity coefficient 3500 values (i.e. the theoretical ε3500 value if all water within the glass were present exclusively as H_2O_{mol} or OH) to find accurate H_2O_{total} and OH concentrations from the 3500 cm^{-1} peak. It requires H_2O_{mol}

concentration to be known (from 5200 or 1630 cm^{-1} peak), but not the proportions of the different H_2O species.

The concentration of OH using the end-member ε3500 values can be calculated by rearranging Equation 4.3, using the definitions $X_{OH} = {C_{OH}}/{C_{H_2O_t}}$, and $X_{H_2O_m} = {C_{H_2O_m}}/{C_{H_2O_t}}$:

$$\varepsilon 3500 = \frac{C_{OH}\varepsilon 3500_{OH} + C_{H_2O_m}\varepsilon 3500_{H_2O_m}}{C_{H_2O_t}} \qquad \text{Eq. 4.6}$$

Rearranging for $C_{H_2O_t}$, and substituting into the Beer-Lambert law (Eq. 4.1), an expression for the concentration of OH is given;

$$C_{OH} = \frac{1}{\varepsilon 3500_{OH}}\left(\frac{100M\left({A}/{l}\right)_{3500}}{\rho} - \varepsilon 3500_{H_2O_m} C_{H_2O_m}\right) \qquad \text{Eq. 4.7}$$

This equation makes it possible to directly calculate the concentration of OH in a sample of known thickness, using the 3500 cm^{-1} absorption peak and the H_2O_m concentration (which is found in the 1630 cm^{-1} peak through Beer-Lambert law (Eq. 4.1), and the end-member ε3500 values. H_2O_t is calculated simply by;

$$C_{H_2O_t} = C_{OH} + C_{H_2O_m} \qquad \text{Eq. 4.8}$$

4.3 EPMA measurements on major elements

The same wafers of Krafla glass cuttings analysed by FTIR were analysed by electron probe microanalysis (EPMA) to determine their major element compositions. The EPMA analysis determine if there are any heterogeneities within and between samples. Major element compositions were also used to calculate the density of the glass cuttings for a more accurate magmatic volatile calculation and in other composition-dependent models used in the study.

4.3.1 Principle

EPMA is a technique for chemical analysis over a small, selected area of solid samples, in which X-rays are excited by a focused electron beam (Potts et al. 1995; Reed 2005). The resulting X-ray spectrum contains lines characteristic of the elements present. Determination of the geochemistry is achieved by measuring line intensities for each element in the sample and comparing their intensities with those emitted from standard samples (Potts et al. 1995; Reed 2005). Standard samples are pure elements or samples of known composition. EPMA can detect elements from atomic number 4 (Be) to 92 (U) (Potts et al. 1995).

4.3.2 Sample preparation

4.3.2.1 Mounting

Glass wafers which had previously been analysed by the FTIR were mounted into 2.5 cm diameter epoxy mounts. Firstly, up to five wafers were placed on double-sided tape adhered to a clean glass plate. Epoxy resin (EPO-TEK® 301) was then poured over the sample wafers into the 2.5 cm cylindrical moulds and left to set overnight. Once the resin had set the mounts were extracted from the mould and the tape was removed, leaving a polished flat surface of the wafers exposed. The glass wafers were then re-polished using diamond paste of 1 μm, leaving the glass surface scratch free.

4.3.2.2 Coating

Most geological samples are non-conductive and require a conductive coating to prevent charging under electron bombardment. Common coating elements are carbon and gold. Carbon coating is the preferred coat for X-ray analysis because it has a minimal effect on the X-ray spectrum (Reed, 2005). As the main aim for

this project was X-ray analysis, the Krafla samples were therefore carbon coated. The sample mounts were placed in a vacuum chamber with a carbon evaporation source consisting of pointed carbon rods in contact. A current of about 100 A was passed through the carbon rods for a few seconds to cause carbon evaporation from the contacts. The evaporated carbon atoms travel in straight lines and coat the mounted samples. The Krafla glass cuttings were carbon coated at the School of Geography, Environment and Earth Sciences, Victoria University of Wellington.

4.3.3 EPMA data collection

Major element compositions of the Krafla glass cuttings were determined using the JEOL JXA-8230 Superprobe at the School of Geography, Environment and Earth Sciences, Victoria University of Wellington. Major elements were determined using an accelerating voltage of 15 kV, current of 8.0 nA, peak/background count times of 30s/15s, and a beam defocused to 10 μm. In order to minimize sodium volatilization during analysis, it was measured for shorter times (10s/5s), measured first and at a fixed peak position in order to eliminate the need for a peak search procedure. Major element analyses were calibrated using natural and synthetic compounds (Jaroewich et al. 1980) as follows: basaltic glass standard VGA-99 for Ca, Mg, Fe; rhyolitic glass standard VG568 for Si, Al, K; and synthetic oxides for Ti, Mn, Cr.

A total of 16 samples were analysed by EPMA. In each sample five points on a clean part of the sample were analysed. To check for any analytical drift during analytical runs, standard sample VGA-99 and VG568 were used as standards (Appendix 1). Each standard was analysed twice after every 25 measurements on the Krafla samples.

4.3.4 EPMA data use

Analyses that generated totals less than 97 wt.% or greater than 103 wt.% were discarded. Measurements from the EPMA were used to compare the glass chemistry of the clear glass and the brown glass and determine if there are any heterogeneities within the samples. Major element compositions were also used to calculate glass density (see Section 4.2.4.3) and in various compositionally dependent models used in the study (Chapter 6).

4.4 Summary

For this project FTIR and EPMA analytical techniques were used on the IDDP-1 glass cutting to help determine the magmatic degassing history of the Krafla magma body in response to a sudden loss of pressure as a result of penetration by drilling. FTIR was used to measure the concentration of H_2O_m, OH, H_2O_t and CO_2 in the glass cuttings. The high resolution maps created using the SR-FTIR, allowed H_2O and CO_2 species distributions to be examined around bubbles in the glass cuttings. The high resolution maps then can help determine the bubble behaviour. Data from the SR-FTIR and the FPA-FTIR are used to calculate the average magmatic volatile concentration of each sample. EPMA is used to determine the major elements compositions of the glass cuttings. In this study these were used to compare the compositions of different glass textures, calculate density to provide a more accurate calculation of the magmatic H_2O and CO_2 contents, and as inputs into various compositionally dependent models used in the study (Chapter 6).

Chapter 5: Glass composition and volatile distribution

5.1 Introduction

This chapter presents data from the major element and magmatic volatile (H_2O and CO_2) analyses of the Krafla glass cuttings. Results from these analyses will form the basis for the interpretations presented in Chapter 6.

5.2 Major element glass chemistry

Table 5.1 provides the average major element compositions of Melt-1a and Melt-1b measured by EPMA. Melt-1a and Melt-1b have broadly similar compositions, but Melt-1a contains higher SiO_2 and K_2O concentrations, while Melt-1b has higher TiO_2, Al_2O_3, MgO and CaO. Both Melt-1a and Melt-1b plot within the rhyolite field on the total alkali silica (TAS) classification diagram (Fig 5.1).

Table 5.1: Geochemistry of the glass cuttings obtained from EPMA. Major oxides normalised to 100 wt% on an anhydrous basis. n is the number of samples analysed

	Melt-1a (n=2)	**STDEV**	**Melt-1b (n=12)**	**STDEV**
SiO_2	77.37	0.34	76.31	0.38
TiO_2	0.29	0.01	0.33	0.02
Al_2O_3	11.78	0.08	12.12	0.11
FeO	2.50	0.10	2.97	0.11
MnO	0.06	0.01	0.07	0.02
MgO	0.16	0.02	0.22	0.01
CaO	1.19	0.02	1.50	0.05
Na_2O	3.28	0.08	3.48	0.09
K_2O	3.37	0.09	2.98	0.05

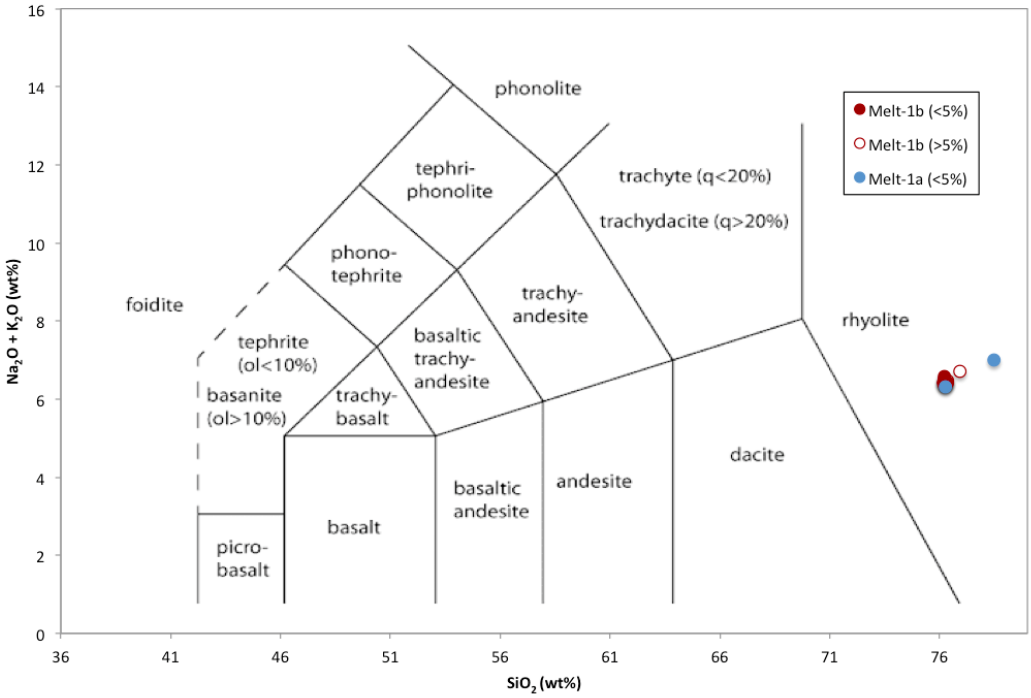

Figure 5.1: TAS diagram with EPMA data of the Melt-1a and Melt-1b.

5.3 Temporal variations of H_2O speciation concentrations in the Krafla melt

5.3.1 H_2O_t concentration

Fig 5.2A shows the temporal variation of total H_2O_t of the Krafla glass cuttings. Overall the H_2O_t concentrations of Melt-1a are lower than those of Melt-1b. The average H_2O_t concentration of Melt-1a (n=3) is 1.46 ± 0.07 wt% and 1.8 ± 0.07 wt% for Melt-1b (n=13). No significant changes are observed in the concentration of H_2O_t over time for both Melt-1a and Melt-1b.

5.3.2 OH concentration

Fig 5.2B shows the concentration of OH over the time of glass recovery. The average OH concentration for Melt-1a (n=3) is 1.00 ± 0.06 wt% and 1.12 ± 0.2 wt% for Melt-1b (n=13). Over the time sampled the OH concentration of Melt -

1a decreased from 1.05 ± 0.08 to 0.93 ± 0.16 wt%. At 16:45 Melt-1b had a large range of OH concentrations (0.71 ± 0.12 to 1.23 ± 0.13 wt%). Apart from the range seen in 16:45, the OH concentrations in Melt-1b from 16:45 until 20:39 increased from 0.71 ± 0.12 to 1.23 ± 0.11 w t%. At 00:50 the OH concentration of Melt-1b was 1.02 ± 0.13 wt%.

5.3.3 H_2O_m concentration

Fig 5.2C shows the concentration of H_2O_m over the time of glass recovery. The concentration of H_2O_m in Melt-1a is lower than Melt-1b. The average concentration of Melt-1a (n=3) is 0.46 ± 0.06 wt%. The average H_2O_m concentration for Melt-1b (n=13) is 0.68 ± 0.1 wt%. At 16:45 and 17:00 there was a large range of H_2O_m concentration in Melt-1b. From 17:30 to 20:39 the concentration of H_2O_m decreased from 0.69 ± 0.12 to 0.57 ± 0.05 wt%. At 00:50 the concentration of H_2O_m was 0.71 ± 0.06 wt%.

5.3.4 OH/H_2O_m

All sample have higher OH concentration than H_2O_m. Fig 5.2D shows the OH/H_2O_m ratio over the time of glass recovery. OH/H_2O_m increased from 0.97 to 2.53 over time for Melt-1b (1645 to 2039), although the large propagated errors mean most values are within error of each other. The glass cutting from 0050 does not follow this trend and has an OH/H_2O_m value of 1.44 ± 0.22. No apparent trend is observed with Melt-1a, though this may reflect the limited data points. The average OH/H_2O_m of Melt-1a is 2.19 ± 0.37 and 1.68 ± 0.45 for Melt 1-b.

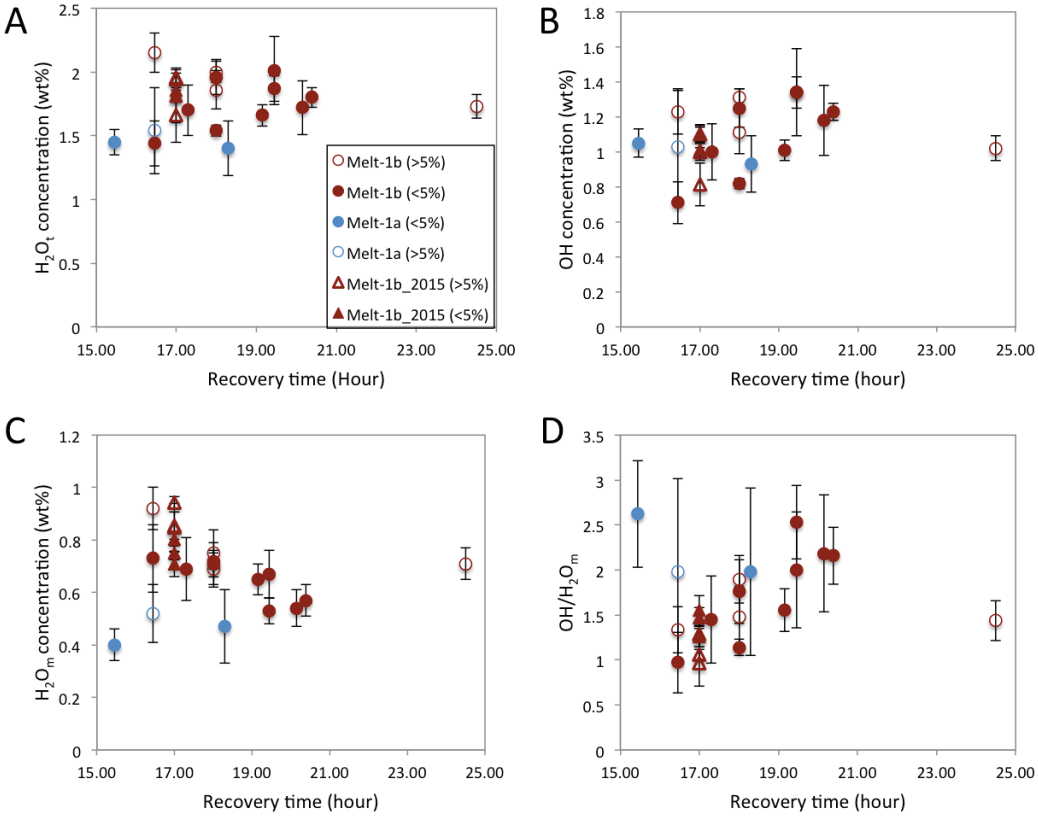

Figure 5.2: Volatile concentrations of the Krafla melt over recovery time. Volatile concentrations were measured for H_2O_t (A), OH (B), H_2O_m (C), and OH/H_2O_m (D). Results from this study (circles) include samples from Melt-1a (blue) and Melt-1b (brown). Other sample results (triangles) were sourced from the addition glass cuttings (Chapter 2, section 2.7.1).

5.4 Temporal variations of CO_2 concentration in the Krafla melt

Fig 5.3 shows the temporal variation of the CO_2 concentration of the Krafla melt. The concentration of CO_2 in Melt-1a is generally higher than the concentration of CO_2 in Melt-1b. The average CO_2 concentration in Melt-1a (n=3) is 139.5 ± 43 ppm, and 78.86 ± 15.4 ppm for Melt-1b (n=10). At 16:45 the concentration of CO_2 in Melt-1b was 72.34 ± 0.4 then the CO_2 decreased to 59.53 ± 8.9 at 17:30. After 17:30, the CO_2 concentration in Melt-1b increased from 63 to 115 ppm (Fig. 5.1D). No trend can be observed for Melt-1a, which may again reflect the limited data for this group. No systematic trend is observed in the vesiculation of the glass cuttings with time.

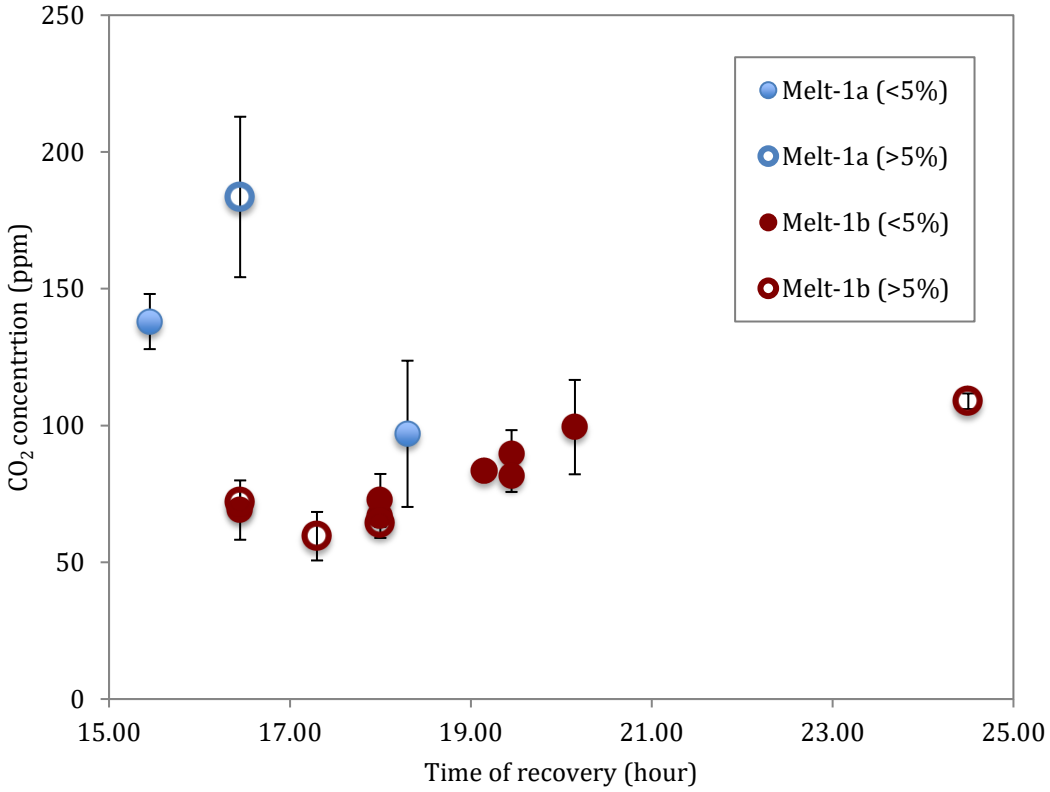

Figure 5.3: CO_2 concentrations in the Krafla melt over the time of recovery.

5.5 H_2O and CO_2 distribution around bubbles

A total of six samples have been mapped for H_2O speciation transects and three samples for CO_2 transects (Appendix 2). These transects have been categorised into three groups;

1. No changes in H_2O and CO_2 concentration towards bubbles (Fig 5.4). This group consists of bubbles in samples 1645C, 1645D and 1945A.
2. H_2O_t and OH concentration decrease towards bubbles and the H_2O_m increases (Fig 5.5). CO_2 does not show systematic trends towards bubbles and may increase, decrease or remain constant. These transects are shown in samples 1545 and 1800C.
3. All H_2O species and CO_2 increase towards the bubbles (Fig 5.6). This is shown in samples 1800A, 1915 and 1945A.

No correlation between time of recovery, glass colour, vesicularity or thickness of the samples has been observed in any of the three groups.

Sample 1800C displays behaviours from group 2 and group 3 (Fig 5.5) for different bubbles in the sample. Indicating that these different bubble behaviours can occur in the same sample.

Sample 1945A (Fig 5.7) have displayed distribution pattern of group 1 and group 3 in the same bubble.

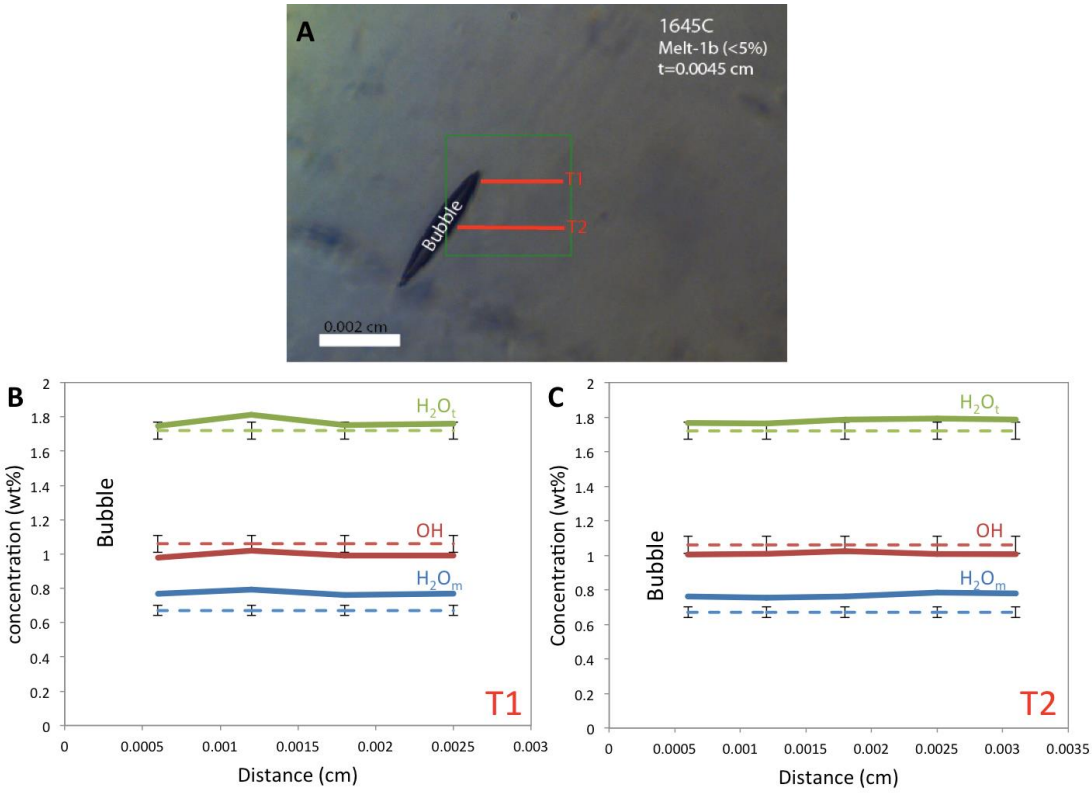

Figure 5.4: Example of H_2O transects showing no changes towards a bubble. Sample was too thin to measure CO_2.

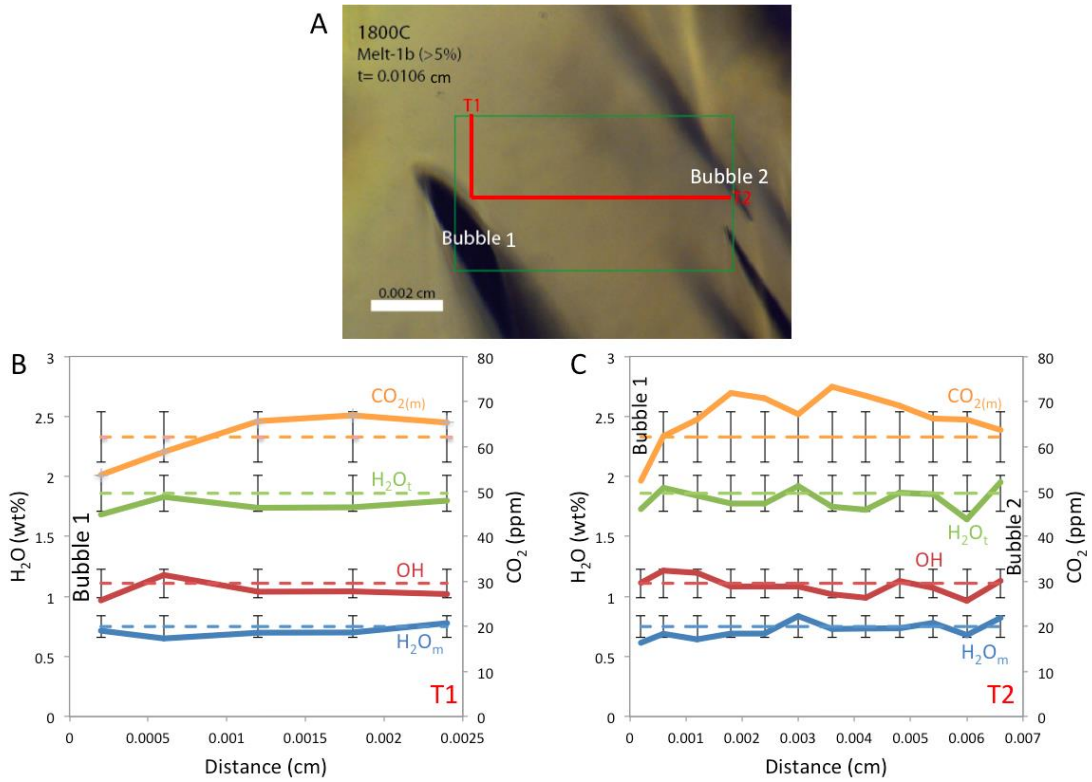

Figure 5.5: Example of samples where H_2O_t, OH and CO_2 decrease and H_2O_m increases towards bubble 1. H_2O_t, OH and H_2O_m increase towards Bubble 2.

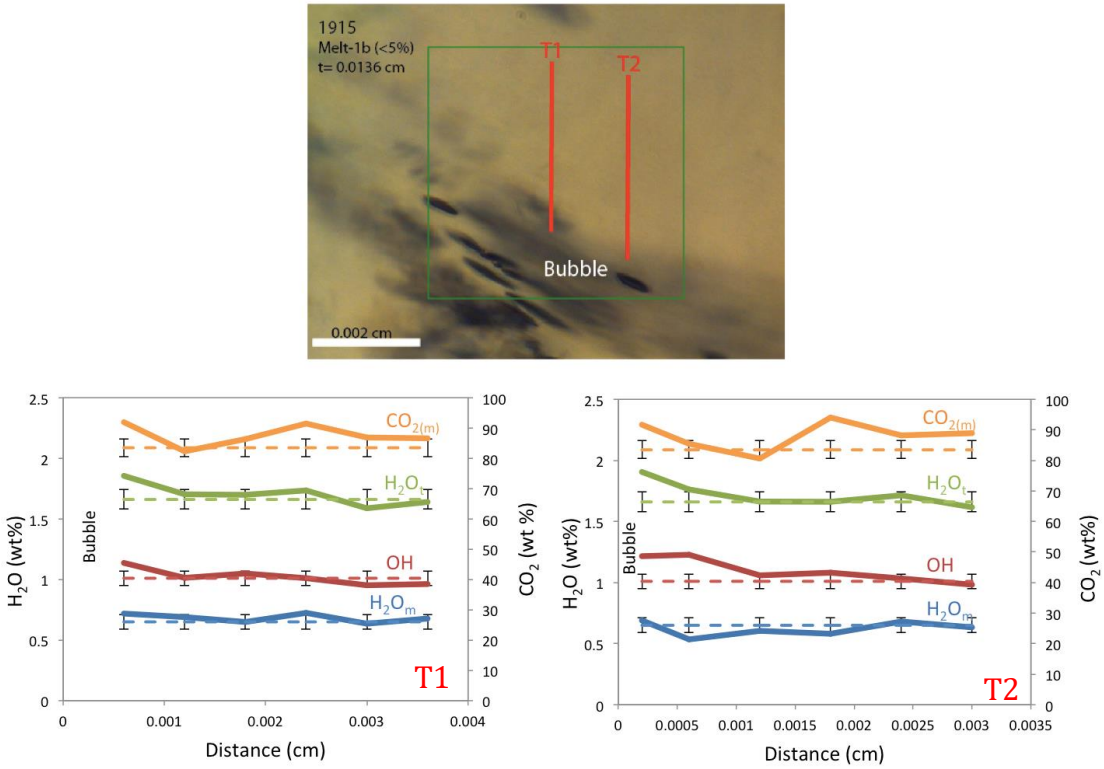

Figure 5.6: Example of bubbles where H_2O_t, H_2O_m, OH and CO_2 increase towards bubbles.

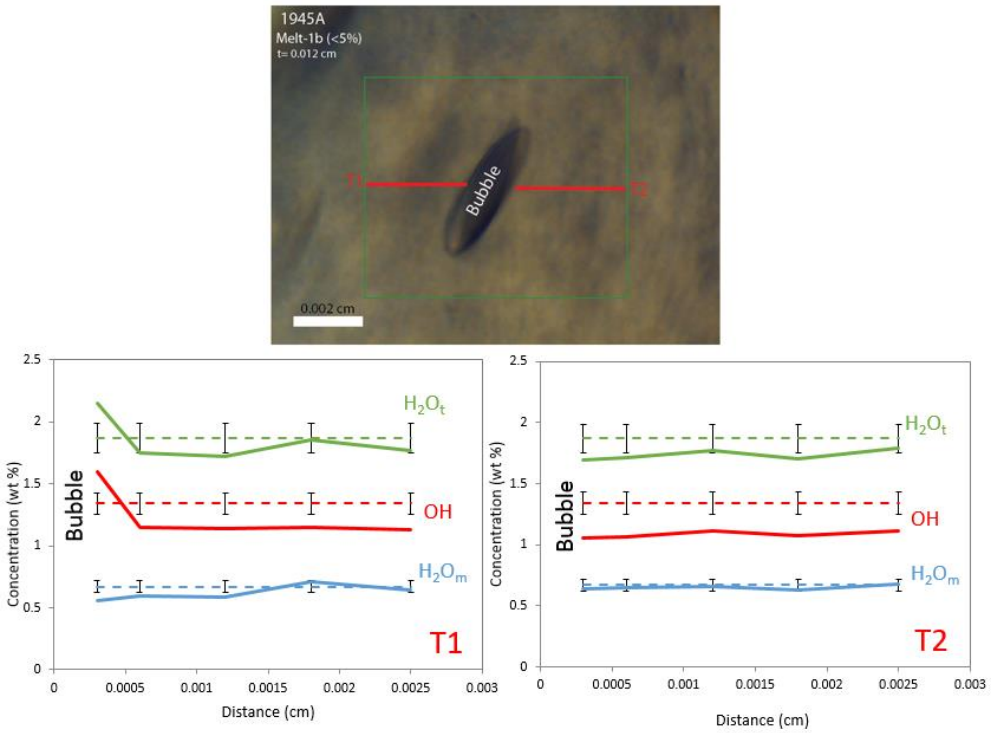

Figure 5.7: Example of multiple volatile distribution around a single bubble. Volatile distribution in T1 shows H_2O_t and OH increases and H_2O_m slightly decreases towards the bubble. Volatile distributions in T2 are constant towards the bubble. Sample is too thin to measure CO_2.

5.6 Summary

Major elements have shown that Melt-1a and Melt-1b are both rhyolite melts however, the two glass types have slightly different glass chemistry. Melt-1a is slightly higher in SiO_2 and K_2O, while Melt-1b has higher concentrations of TiO_2, Al_2O_3, MgO and CaO. The concentration of H_2O_t in the Krafla melt showed no change over time, however, OH/H_2O_m and the concentration of CO_2 increased over time. No correlations between volatile content and vesiculation of the glass cuttings have been observed. Based on seven samples, three volatile distribution around bubbles were identified. 1) The first group showed no changes in volatile distribution towards bubbles, 2) the second groups shows a decrease in H_2O_t and OH, and a increase of H_2O_m towards bubbles and 3) magmatic volatiles increases towards the bubbles. These transects showed no systematic trend with time or texture. Based on theses analyses, the next chapter will present interpretations of the response of the magma to being intercepted by the drilling.

Chapter 6: Implications from the magmatic volatile evolution

6.1 Introduction

This project set out to examine the magmatic volatile (H_2O and CO_2) evolution of the intersected magma from the IDDP-1. The results of the FTIR analyses have answered the two objectives below.

1. Determine any changes in magmatic volatile concentration through time.
2. Map the distribution of H_2O species and CO_2 around bubbles in the samples from the time-series set of samples collected during drilling into the Krafla magma body.

These results, together with other published datasets, will allow the remaining objectives to be addressed:

3. Determine the magmatic degassing history of the Krafla magma body in response to a sudden loss of pressure as a result of intersection by the drilling.
4. Use the degassing history to assess quenches timing and changes in magmatic viscosity.
5. Investigate why the Krafla magma did not erupt while it was being drilled.

This chapter uses the results from the EPMA and FTIR analyses from the previous chapter in order to establish the magmatic volatile evolution of the Krafla melt after the unexpected depressurisation from the IDDP-1 drill. The findings from this project will also be compared to other glass chemistry and magmatic volatile studies from Zierenberg et al. (2013) and data from Saubin et al. (2017). Finally, possible future directions for studies on the magmatic volatiles in the intercepted Krafla melt will be discussed.

6.2. Pre-drilling magmatic conditions

6.2.1 Melt chemistry

Glass chemistry of the glass cuttings from this project and Saubin et al. (2017) have shown that the texturally defined Melt-1a (clear glass) has a range of chemistries clustering into two distinctive end members. The two end-member glass chemistries are similar to the reported glass chemistries of Melt 1 and Melt 3 from Zierenberg et al. (2013), (Fig 6.1). Earlier recovered Melt-1a tends to have a similar composition to Zierenberg et al.'s (2013) Melt-3, however Melt-1a samples have slightly lower Al_2O_3 than Zierenberg et al. (2013) Melt-3. This could reflect the difference of the standardisation procedure of the two different EPMA machines during data collection rather than reflecting a different melt. The later recovered Melt-1a has a similar composition to Zierenberg et al.'s (2013) Melt-1 (Figure 6.2). Two of the Melt 1a samples plot in a linear trend between the Melt-1 and Melt-3 chemistries. There are no systematic differences in vesicularity and microlite contents between the glass cuttings (Saubin et al. 2017). Therefore, the linear variation of the chemistry between the end-member compositions suggests the Melt 1a cuttings represent mixing between Melt-1 and Melt-3 (Fig 6.3). This interpretation is consistent with hypothesise invoked by Zierenberg et al. (2013).

The SiO_2 contents of Melt-1b reported here and in Saubin et al. (2017), both measured in the same electron microprobe laboratory, are slightly lower than Zierenberg et al. (2013), where the SiO_2 contents of earlier recovered Melt-1a are slightly higher than Melt-3. These differences are very small but are not likely to be a result from the interlaboratory bias because it would be expected that all the samples from this project and Saubin et al. (2017) would be systematically higher or lower than Zierenberg et al. (2013) contents. The samples from this project and Saubin et al. (2017) could reflect glass cuttings closer to two end-members.

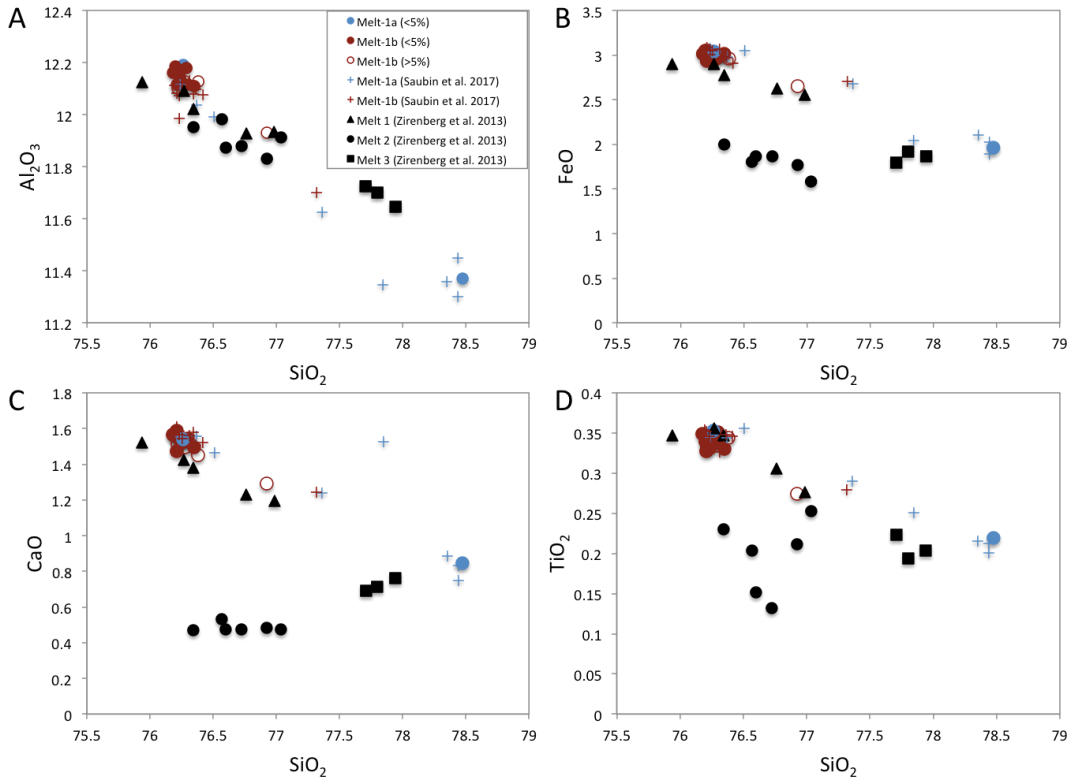

Figure 6.1: Chemical variation diagrams for the different glasses from data obtained at the EPMA, additional data from Saubin et al. (2017) and Zierenberg et al. (2013). Data are normalised to 100% on an anhydrous basis. A) SiO_2 versus Al_2O_3, B) SiO_2 versus FeO, C) SiO_2 versus CaO and D) SiO_2 versus TiO_2.

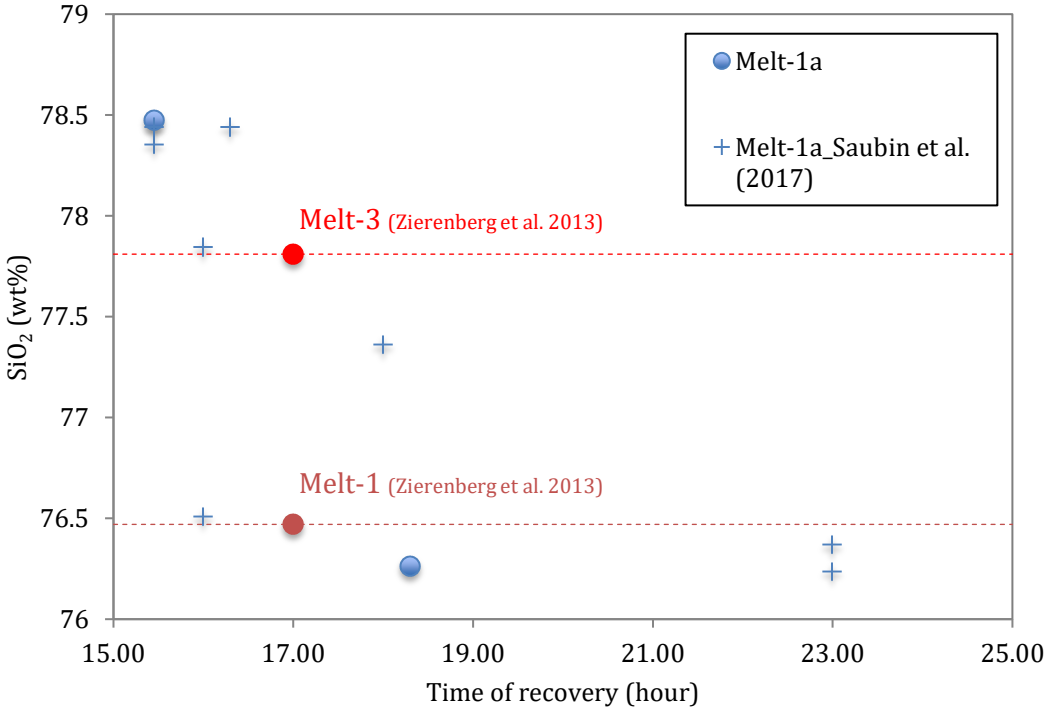

Figure 6.2: SiO_2 variation of Melt-1a (clear glass) over time of recovery.

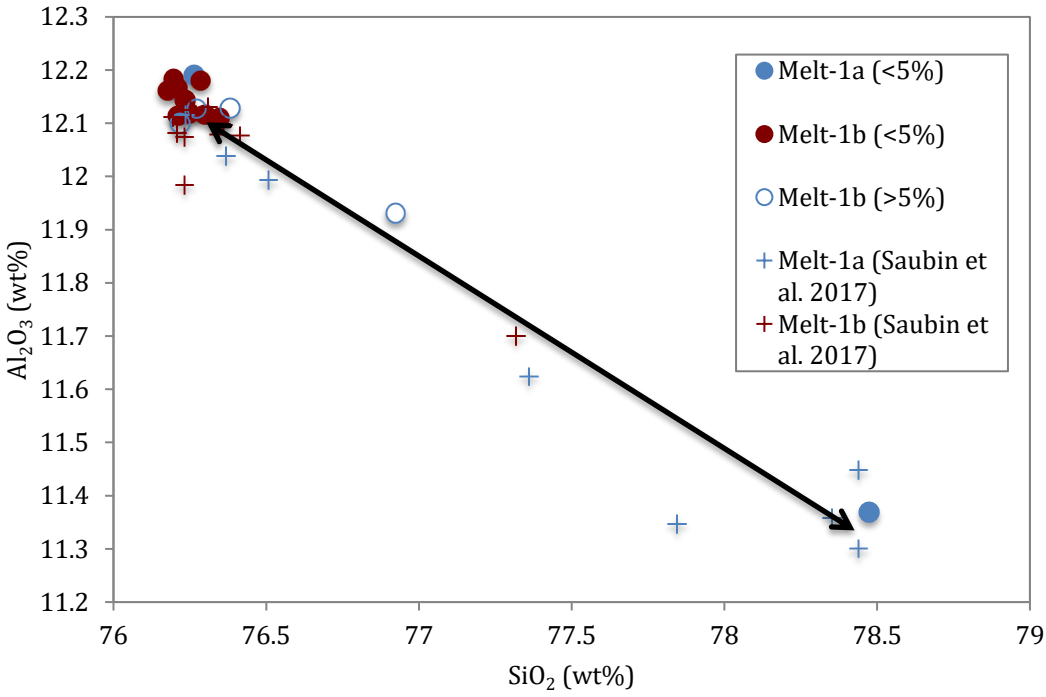

Figure 6.3: Al_2O_3 versus SiO_2 of the data from the EPMA (circles) and EPMA data from Saubin et al. (2017) (crosses). Linear trend indicates mixing of Melt-1a and Melt-1b.

The glass chemistry of Melt-1b (brown glass) from this project and Saubin et al. (2017) has similar glass chemistry to Melt-1 from Zierenberg et al. (2013), (Fig 6.4). Based on Zierenberg et al. (2013) interpretations (Chapter 2 Section 2.6.1) Melt-1b represents the quenched magma body that IDDP-1 drilled into and Melt 3 (Melt 1a) relates to a partial melt of the surrounding felsite.

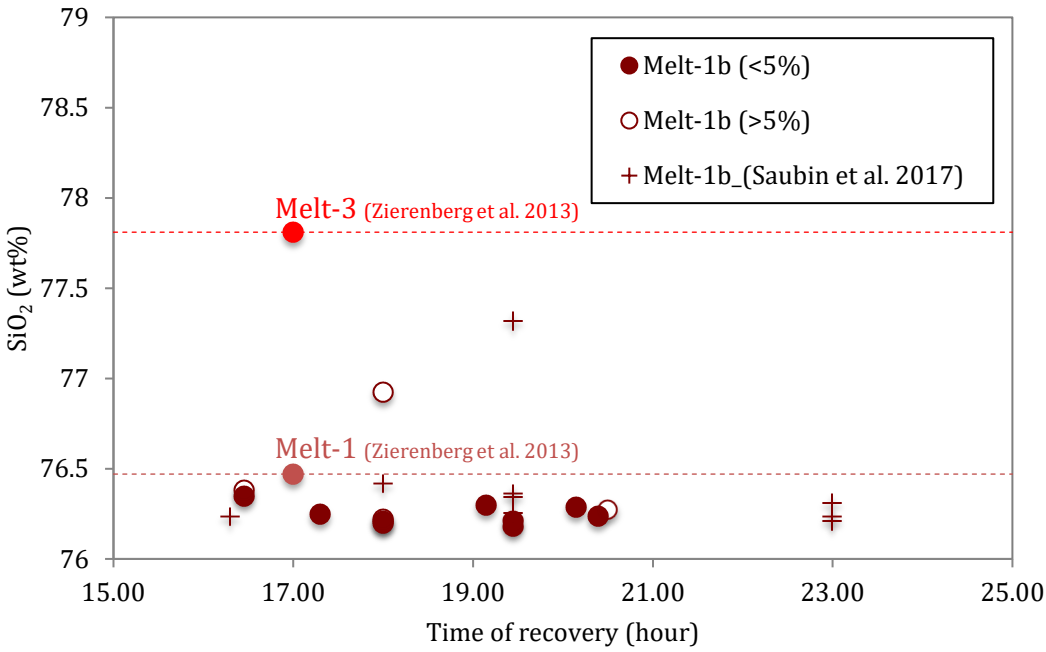

Figure 6.4: Variation of SiO_2 of Melt-1b (brown glass) over time of recovery.

6.2.2 Pre-drilling conditions

Fig 6.5 illustrates the conditions of the melt prior to drilling. The major element analyses have shown the distinct chemical signature of the magma body Melt-1 and Melt-3 and the surrounding felsite, which appears to have interacted with the magmatic body close to the contact. Zierenberg et al. (2013) has suggested that the crystal rich Melt-3 is a result of assimilation of the magma body (Melt-1) with the surrounding felsite. Based on the major element analysis of the crystal-poor clear glass cuttings, Melt-1a has glass chemistries that span the compositions of both Melt-1 and Melt-3. The earlier quenched clear glass have similar compositions to Melt-3, and the later quenched clear glass cuttings are similar in composition to the magma body based on Zierenberg et al. (2013) hypothesis. This supports the hypothesis of Zierenberg et al. (2013) that Melt 3 formed the boundary of the magma body, with more pristine magma being encountered as the drilling progressed.

The CO_2 concentrations in Melt-1a are higher (139.5 ± 43 ppm) than the CO_2 concentration in Melt-1b (Chapter 5, Section 5.4). The high concentration of CO_2 could be caused by CO_2 fluxing from below (Rust et al. 2004). Advancing the interpretation of

Zierenberg et al. (2013), Melt 1 partially melted the felsite to create Melts 3 and 1a. The partially melted felsite melt (Melt-1a) would be an initially anhydrous melt undersaturated in CO_2 and H_2O. This allows Melt-1a to dissolve CO_2 and H_2O from the deep volatiles fluxing from underlying magma (Rust et al. 2004) to create a distinct CO_2 to H_2O ratio reflecting a different volatile saturation history.

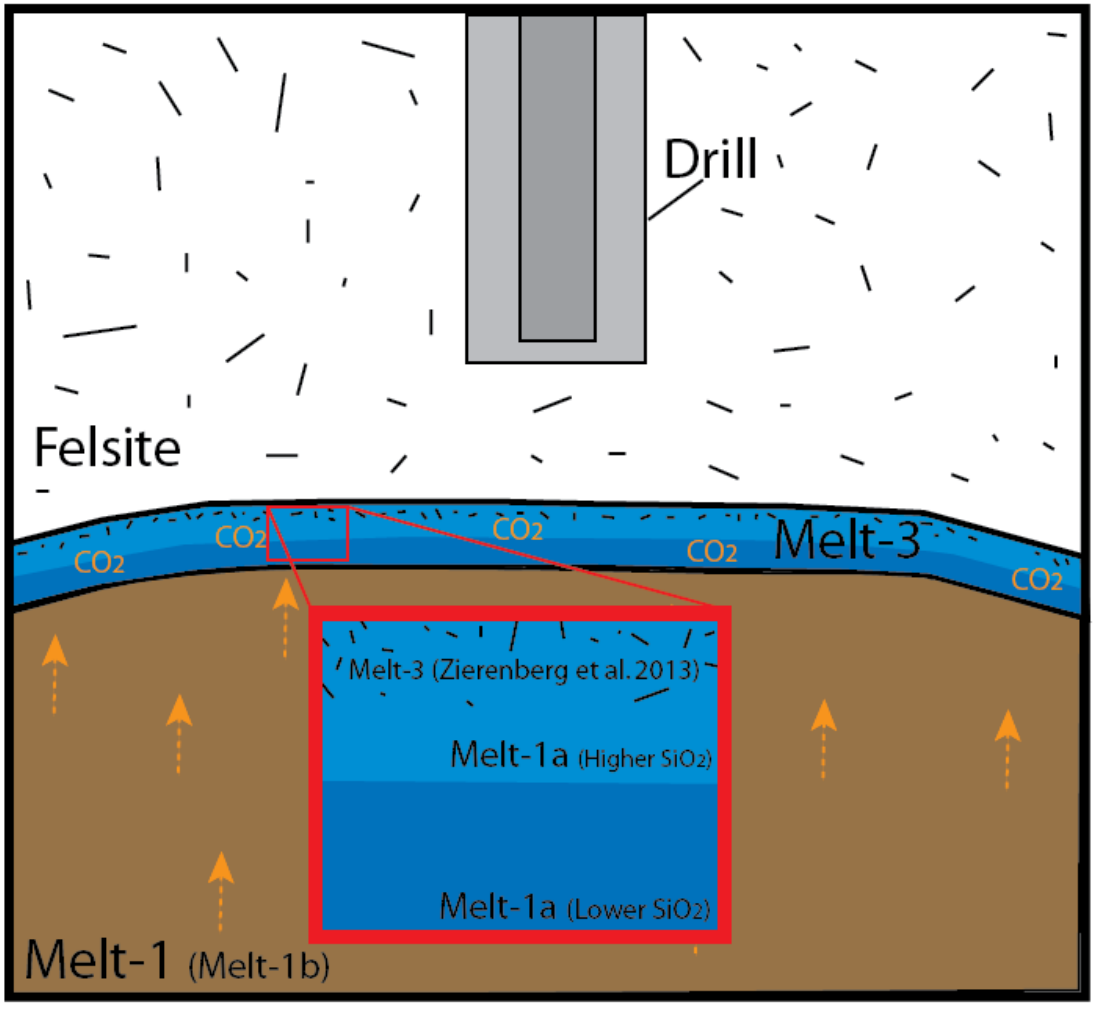

Fig 6.5: Schematic drawing of the melt properties prior to drilling. Melting of the felsite forms an undersaturated melt (Melt-1a) which then dissolves the CO_2 from deep sources.

6.3 Temporal variation of temperature and pressure

The major element measurements and water content measurements were used to estimate the quenching temperatures of the melt. For this project, two methods were used to calculate the quenching temperature; the model of Nowak and Behrens (2002) and the model of Ihinger et al. (1999). The model of Nowak and Behrens (2002) was used as it considers the major element and H_2O content of the glass cuttings. The model of Ihinger et al. (1999) uses the absorbance of the H_2O_m and OH bands in the near-IR region (chapter 4; section 4.2.4.1). This model was used in this project because it is the model Zierenberg et al. (2013) used to estimate the quenching temperature and thus will allow temperatures estimated in this study to be directly compared to the quench temperatures estimated by Zierenberg et al. (2013).

6.3.1 Nowak and Behrens (2001) model

Fig 6.6 shows the equilibrium speciation temperature of the Krafla melt from the model of Nowak and Behrens (2001). To avoid uncertainties on the thickness of the glass wafers quench temperature contours were calculated by using the ration of OH/H_2O_m. Melt-1a shows a decrease from ~575 to ~525 °C over time. Melt-1b shows an increase in temperature over time from <500 to ~625 °C. However, at 00:50 the equilibrium speciation temperature decreases to <500 °C.

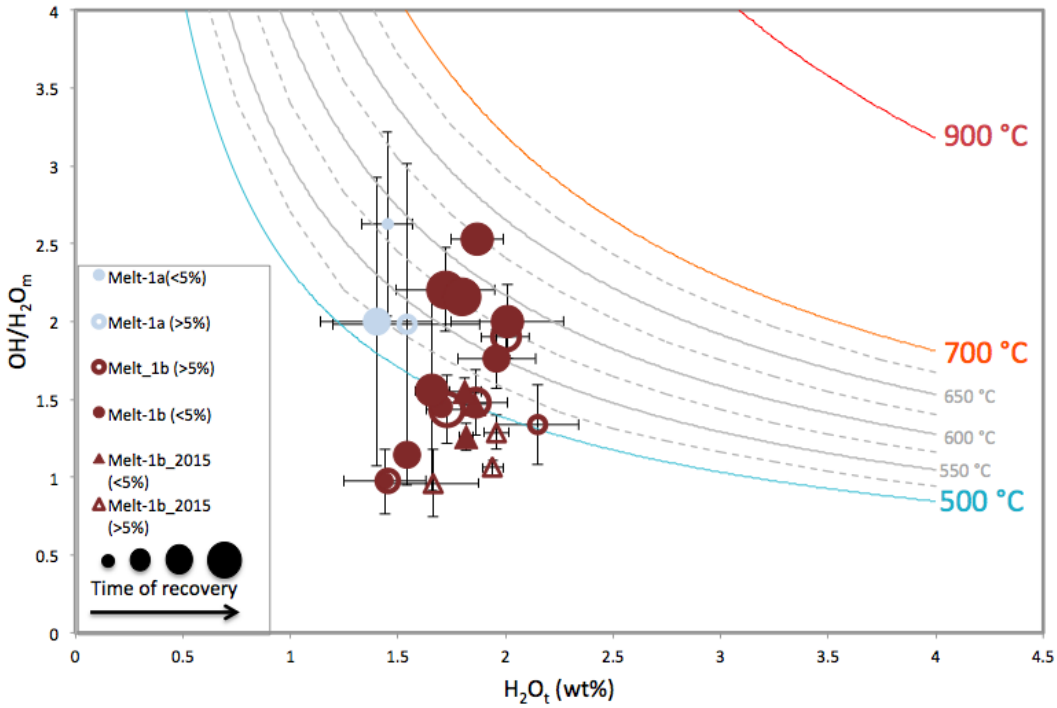

Figure 6.6: Equilibrium speciation temperature of the glass cuttings. Equilibrium speciation temperature contour calculated from Nowak and Behrens (2001). Lowest possible quench temperature contour is 500 °C.

6.3.2 Ihinger et al. (1999) model

Fig 6.7 shows the quench temperatures calculated using the Ihinger et al. (1999) model. It appears as if the quench temperature of Melt-1a is lower than the quench temperature of Melt-1b apart from the glass cutting recovered at 15:45, however, this may again reflect the limited data for Melt-1a. Both Melt-1a and Melt-1b show an increase in quench temperature over time from ~600 °C to ~1400 °C. Quench temperatures estimates from Zierenberg et al. (2013) fit within the increasing quench temperature trend.

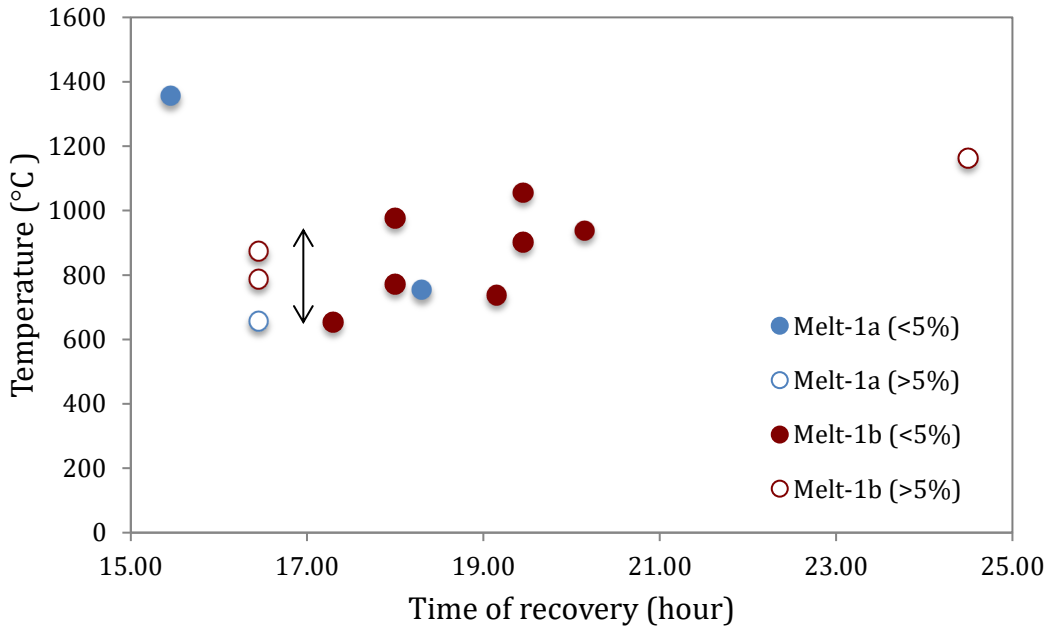

Figure 6.7: Quench temperature of the Krafla glass cutting over time of glass recovery. Quench temperature calculated using a model of Ihinger et al. (1999). Arrow shows calculated quench temperature range from Zierenberg et al. (2013) calculated using the same model.

6.3.3 Comparisons between the two models

The quench temperature from the Nowak and Behrens (2001) model are much lower than the quench temperature obtained from the Ihinger et al. (1999) model. Both models indicate that the first recovered sample at 1545 has a higher quench temperature than 16:45 and that quench temperatures for Melt-1b increase with time.

6.4 H_2O-CO_2 saturation pressure

Pressures at which the H_2O-CO_2 contents of each glass sample were saturated were calculated using VolatileCalc (Newman and Lowenstern, 2002). The lowest temperature that VolatileCalc is calibrated for is 600 °C. Temperatures calculated by the Nowak and Behrens (2001) model for all but one of the samples are below this. Thus, the saturation pressures were calculated at 600 °C (Fig 6.8). Most glass cuttings have H_2O-CO_2 saturation pressures between 15 and 25 MPa. Samples 1645B, 18:00B and 18:30C have saturation pressures below the hydrostatic pressure (~16 MPa) and the rest are above.

The H_2O-CO_2 saturation pressure of Melt-1b increases over time. No trend is observed with H_2O-CO_2 saturation pressure of Melt-1a over time, this may reflect the limited data points.

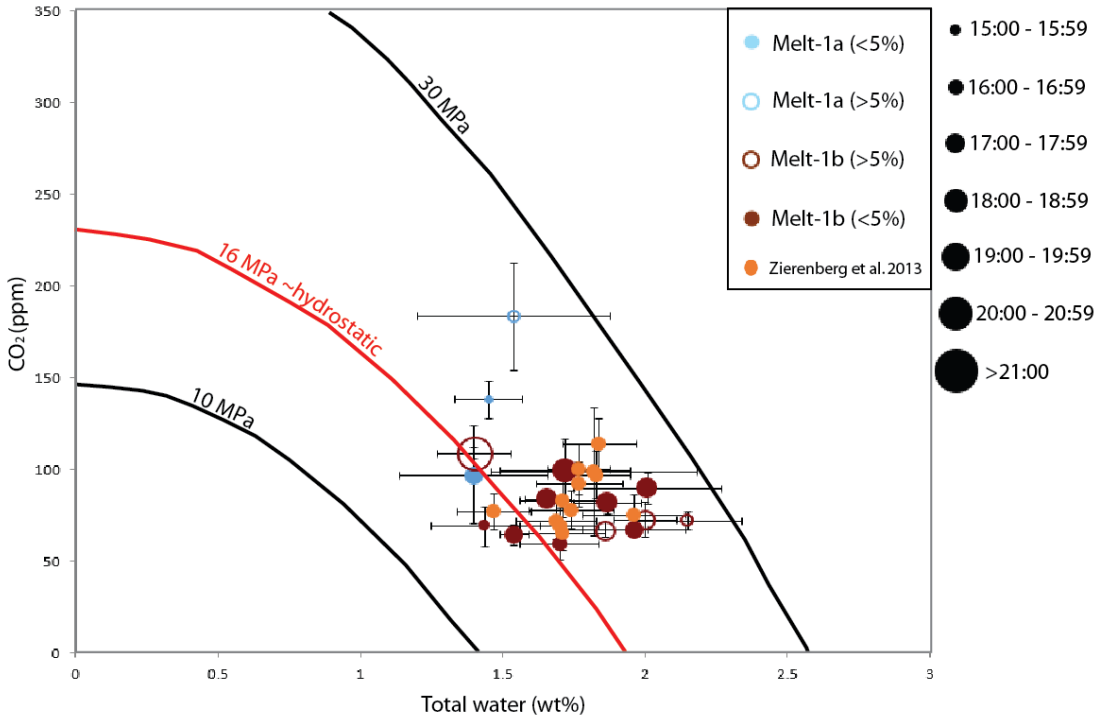

Figure 6.8: Plot of total H_2O vs CO_2. Saturation pressure contours calculated at 600 °C using VolatileCalc (Newman and Lowenstern, 2002).

Using the quench temperatures estimates using the Ihinger et al. (1999) model, H_2O-CO_2 saturation pressures at 900 °C were calculated using VolatileCalc (Newman and Lowenstern, 2002). Quench temperature of 900 °C was used because Zierenberg et al. (2013) used this model assuming a temperature of 900 °C. H_2O-CO_2 saturation pressures from this project can be directly compared to Zierenberg et al's (2013) H_2O-CO_2 saturation pressures estimates. Fig 6.9 shows the saturation pressures calculated at 900 °C. The glass cuttings are mostly between ~30 and 50 MPa. These pressures are still below lithostatic pressure of ~50 MPa, but all glass cuttings are greater than the hydrostatic pressures of ~16 MPa when using a quench temperature of 900 °C. H_2O-CO_2 saturation pressures from Zierenberg et al. (2013) ranged from 35 - 45 MPa. If correlation between H_2O-CO_2 saturation pressures and time are expected it is expected that Zierenberg et al's (2013) points would plot in single point within the trend. This

suggests that there is no systematic correlation between H_2O-CO_2 saturation pressures and time.

In summary, the lower temperature VolatileCalc model indicates lower pressures, and potentially that Melt-1b came from increasingly higher pressures and possibly deeper depths.

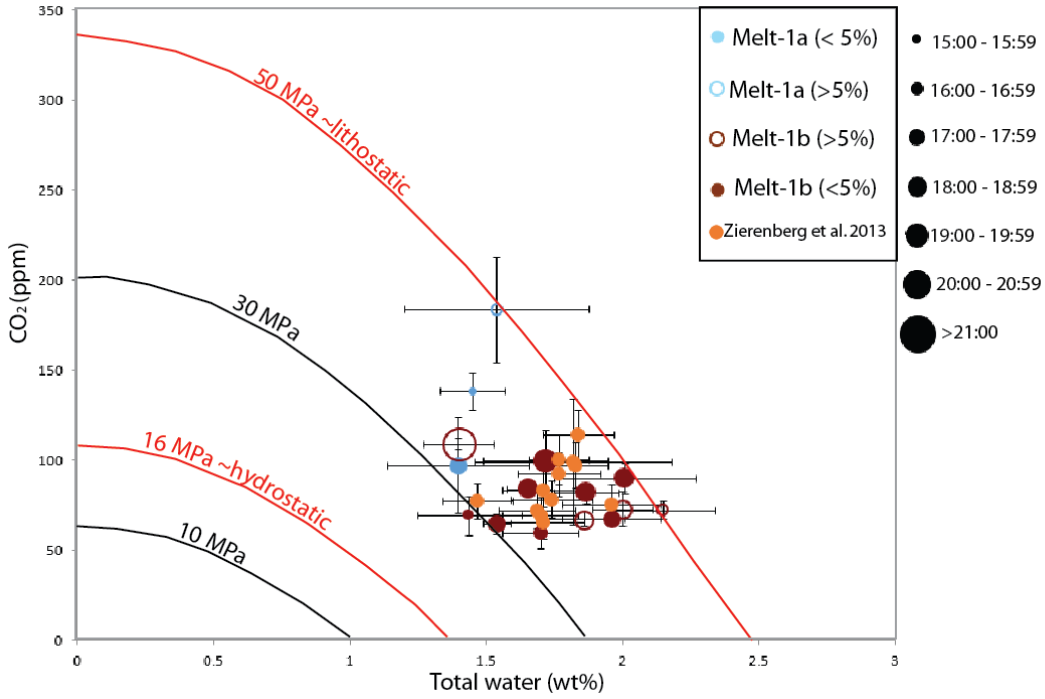

Figure 6.9: Plot of total H_2O versus CO_2. Saturation pressure contour at 900 °C calculated using VolatileCalc (Newman and Lowenstern, 2002).

6.5 Viscosity and glass transition temperature

Using the temperatures calculated from the two quench temperature models viscosity was calculated using a model of Giordano et al. (2008). Fig 6.10 shows the change in melt viscosity (using parameters from both Nowak and Behrens (2001) and Ihinger et al. (1999) models) over time. The lower temperatures of Nowak and Behrens (2001) produce a much higher viscosity estimate compared to Ihinger (1999). Viscosity estimates using both Nowak and Behrens (2001) model and Ihinger et al. (1999) model shows that earlier recovered melt has relatively lower viscosity and from time intervals ~18:00 to ~20:15 the viscosity of melt-1b decreases due to the increase in temperature.

There seems to be a relationship between viscosity and vesicularity where glass cutting with high vesicularity has relatively lower viscosity than the dense glass. This lower viscosity could reflect higher diffusion rates facilitating bubble nucleation and growth, however this may reflect the limited data for this group.

Glass transition temperatures were calculated using the viscosity, assuming the glass transition temperature is the temperature at which the melt is at a viscosity of 10^{12} Pa s (Chapter 3; Section 3.6.1). The average glass transition temperature of Melt-1a is 557 ± 2 °C and the average glass transition temperature of Melt-1b is 528 ± 15 °C. Table 6.1 summarises the glass transition temperature of the Krafla glass cuttings based on their calculated viscosity. The glass transition temperature is consistent with the quench temperature calculation from the Nowak and Behrens (2001) model and the felsite temperature estimates (~ 500 °C) from the Horner plot (Chapter 2, section 2.4.3; Morstensen et al. 2014). However, this may not reflect the actual quench temperature of the melt because of the quench effect (Chapter 3; Section 3.4.2).

In summary, the viscosity of the melts are very high, especially if the Novak and Behrens (2001) model is calculating an equilibrium temperature just prior to drilling induced quenching. However, an imperfect quench may mean that these temperatures are minimums, and these viscosities are maximums. But this would contribute to explaining why the magma did not significantly vesiculate or rise up the borehole to the surface.

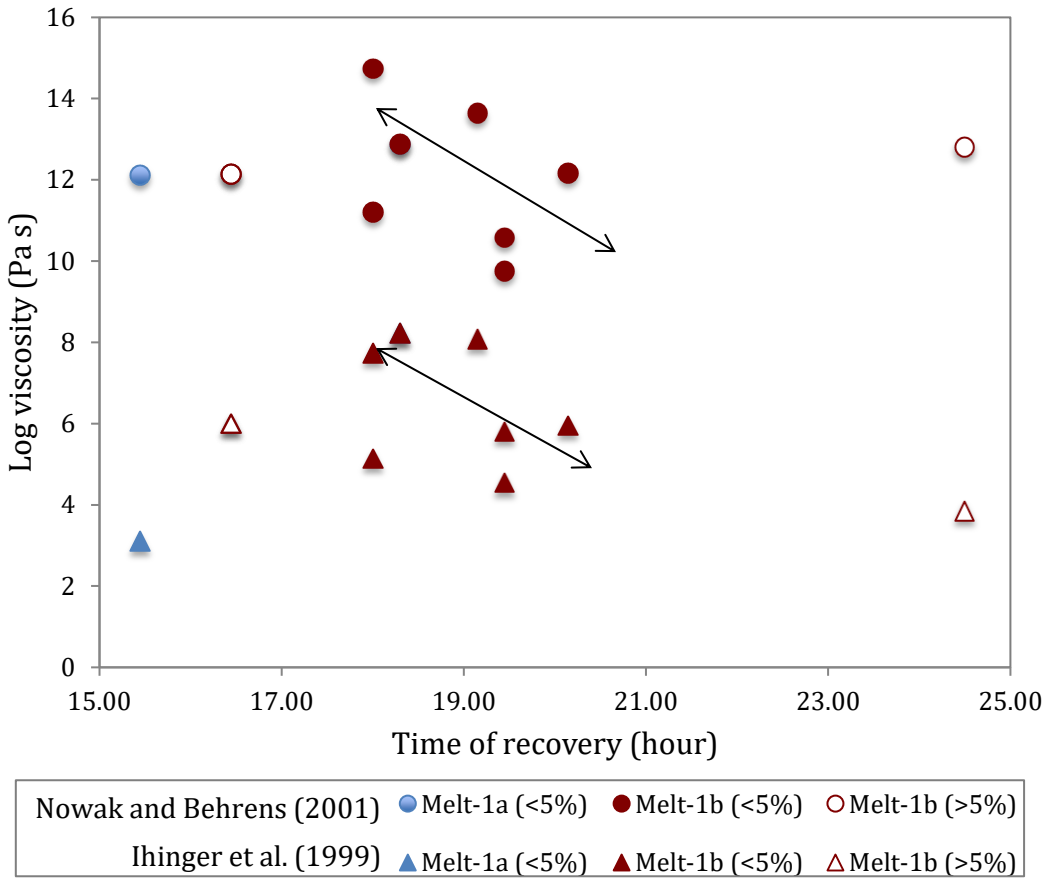

Figure 6.10: Viscosity of the Krafla melt over time. Circle represents viscosity using specific temperatures for each sample from the model of Ihinger et al. (1999) and the triangle represents the viscosity using estimated temperatures for each samples from the model of Nowak and Behrens (2001). Both models show a decrease in viscosity with a low vesiculated Melt-1b. Viscosity calculated using a model of Giordano et al. (2008)

Table 6.1: Average glass transition temperature of the Krafla melt based on viscosity (~10^{12} Pa·s)

	n	Tg (°C)	STDEV
Melt-1a	2	557	2
Melt-1b	13	528	15
All samples	15	532	17

6.6 Bubble behaviour in the Krafla magma

Volatile distribution maps from this project have identified three different groups (Chapter 5 section 5.5).

- The first group shows that the volatile distribution is constant towards a bubble. This suggests that the melt is at equilibrium (i.e. no change in pressure and/or temperature) (Chapter 3 section 3.9.3).
- The second group have shown H_2O_t and OH distribution decreases towards a bubble but the H_2O_m increases. This suggests initially the melt was depleted in OH and total water close to the bubble due to diffusion towards the bubble and bubble nucleation and growth. However the increasing H_2O_m indicates that a decrease in temperature may have driven some water resorption and enriched the melt in H_2O_m. As a result both, the original OH distribution is preserved and the resorbed H_2O_m also preserved representing the new melt condition (Chapter 3 section 3.9.3).
- The third group have shown the distribution of magmatic volatile (including H_2O_m and CO_2) increases towards the bubble. Suggesting that the bubble is undergoing resorption, indicating that there is an increase in pressure and decrease in temperature (Chapter 3 section 3.9.3).

Different groups can also occur in the same sample and in the same bubble suggesting that the melt is preserved in a state of locally variable disequilibrium and bubbles were behaving heterogeneously. All of the glass cuttings showed higher concentration of OH than H_2O_m this suggests that throughout time the melt quenches relatively rapidly (McIntosh et al. 2014) freezing in the state of disequilibrium. This relatively rapid quench is also supported by the preservation of highly elongate shaped bubbles, which preserves shearing in the magma present at the time of quenching. However, we emphasize that the spatial variation in volatiles is very small and is close to the error of the measurements.

Possible reasons why maybe the spatial variation in volatile distribution is relatively small could be:

1. In thick samples the Far-field (average concentration of volatile distribution with no influence on bubbles and crystals) concentration overwhelms the area affected by the bubbles (Fig 6.11). Thicker samples also means that the beam light is more likely to go through areas which may have effected area

2. Bubbles may also be too small. Small bubbles (find average bubble size) effect small area than the larger bubbles and perhaps wasn't detectable.

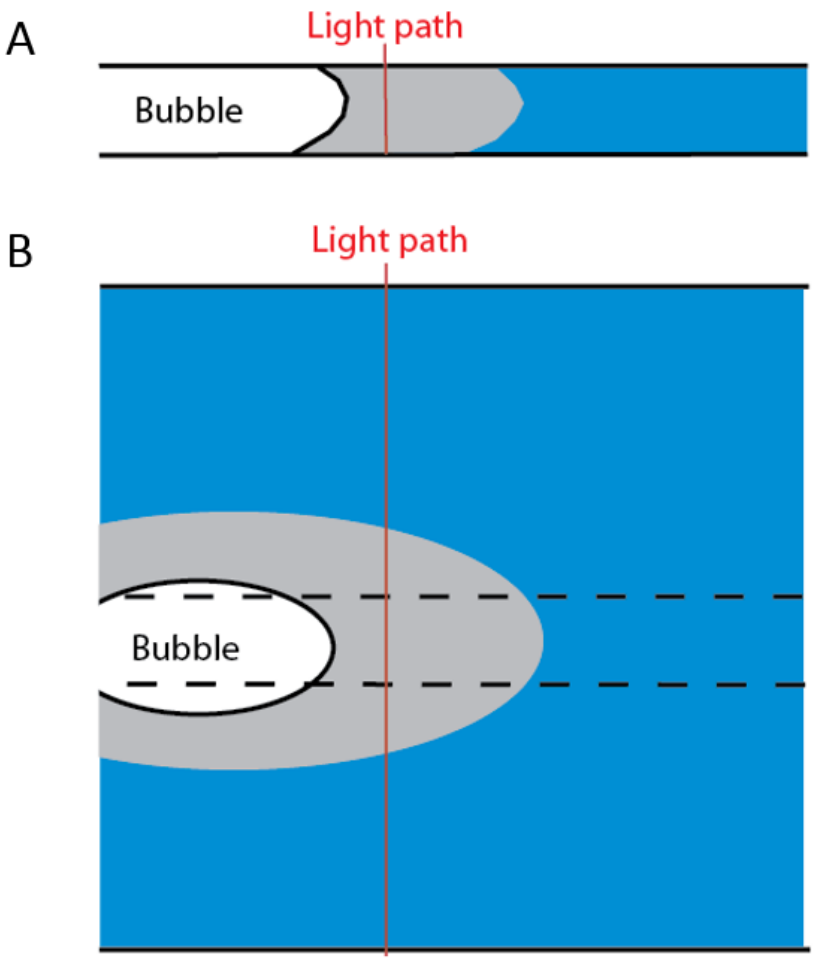

Figure 6.11: Schematic diagram showing how sample thickness can influence recorded volatile measurements. In thin samples (A) where the light sensor can directly measure near the edges of bubbles (grey region) there is little influence from the far-field (blue region) bulk volatile concentration. In thicker samples where the bubble and near regions are fully encased by the far-field (B), measured volatile concentrations can be skewed by the surrounding far-field bulk concentration.

6.7 Magmatic response

6.7.1 Initial response (15:00 – 17:00)

Fig 6.12 illustrates the initial magmatic response from the intercepted drill. Evidence of depressurisation is present in the earlier recovered Melt-1a glass cuttings. These include high abundance of bubbles in Melt-1a (Zierenberg et al. 2013; Saubin et al.

2017). However, this magmatic response was short in duration as at ~17:00 the abundance of bubble rich Melt-1a decreased and the recovered glass cuttings became dense (Saubin et al. 2017). This suggests that depressurisation from the drilling only affected the magma for a short interval before returning back into equilibrium. The short depressurisation period suggest that the drill only affected a small area of the magma and thus the depressurisation of the melt was not great enough or long enough in induce an eruption. Another reason why eruption did not occur is that the melt viscosity was too high to allow significant magma chamber scale bubble nucleation and growth sufficient enough to induce an eruption. It is also worth considering that the pressure in drill hole is variable (Sabin et al. 2017), but also controlled by the drillers who intentionally try to minimise large pressurisation or depressurisation events. This additional control by the drillers may have prevented an eruption if magmas had been suddenly decompressed to atmospheric conditions.

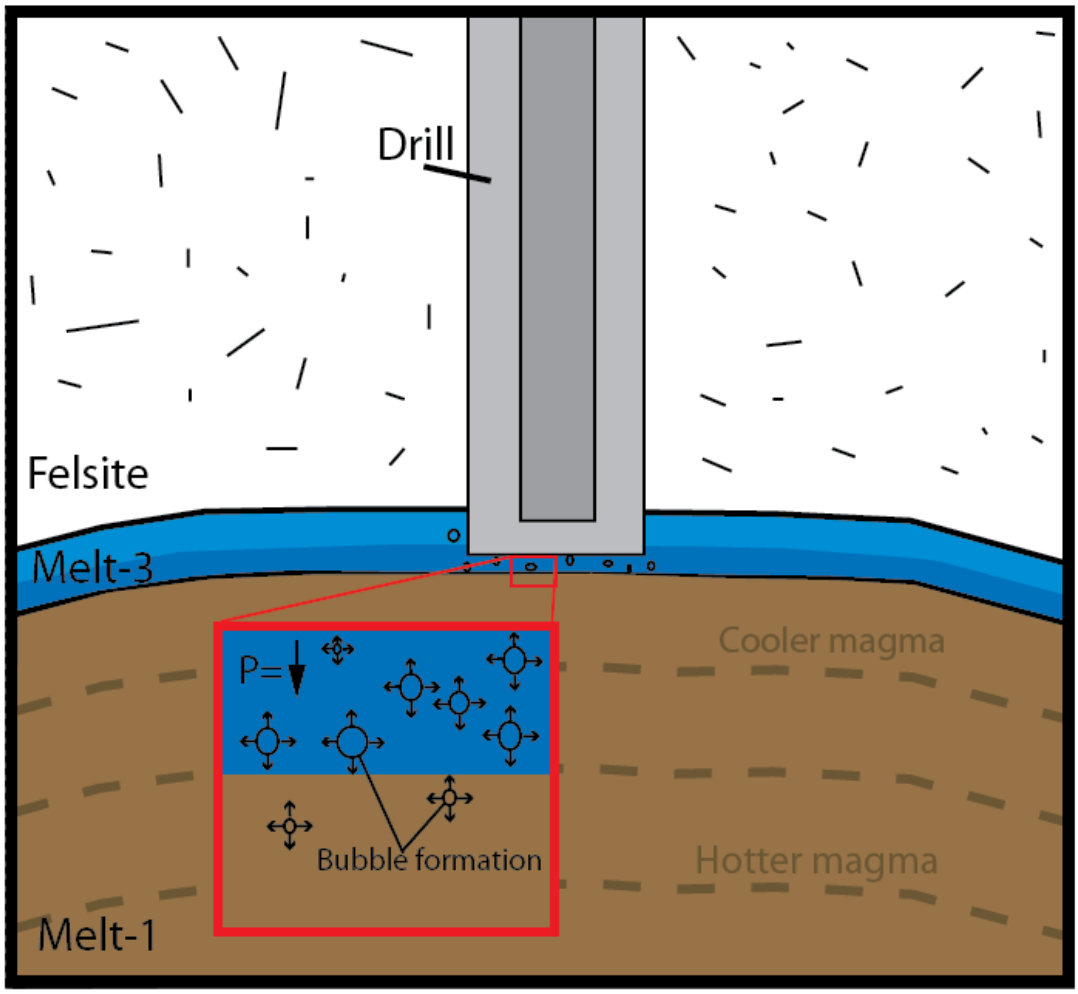

Figure 6.12: Schematic illustration of the initial response of the magma interception. As a response to depressurisation from the drill, bubble formation occurred in Melt-1a (Melt-3)

6.7.2 Later response (>17:00)

Figure 6.13 illustrates the later magmatic response. An increase in the quenching temperature (Fig 6.6 and Fig. 6.7) and corresponding decrease in viscosity (Fig 3.10) from both models from Nowak and Behren (2001) and Ihinger et al. (1999) indicated hotter magma rising up the borehole. The H_2O-CO_2 saturation pressures models also show a small increase in pressure (difference of ~15 MPa assuming temperature is 600 °C or difference of ~20 MPa assuming temperature is 900 °C) indicating that either the drill didn't penetrate deep within the magma or that the magma did not rise far to meet the drill (a few metres or tens of meters). The lack of bubbles in these Melt-1b samples

indicate that either this melt rapidly quenched before vesiculation was possible or that the melt was understaurated.

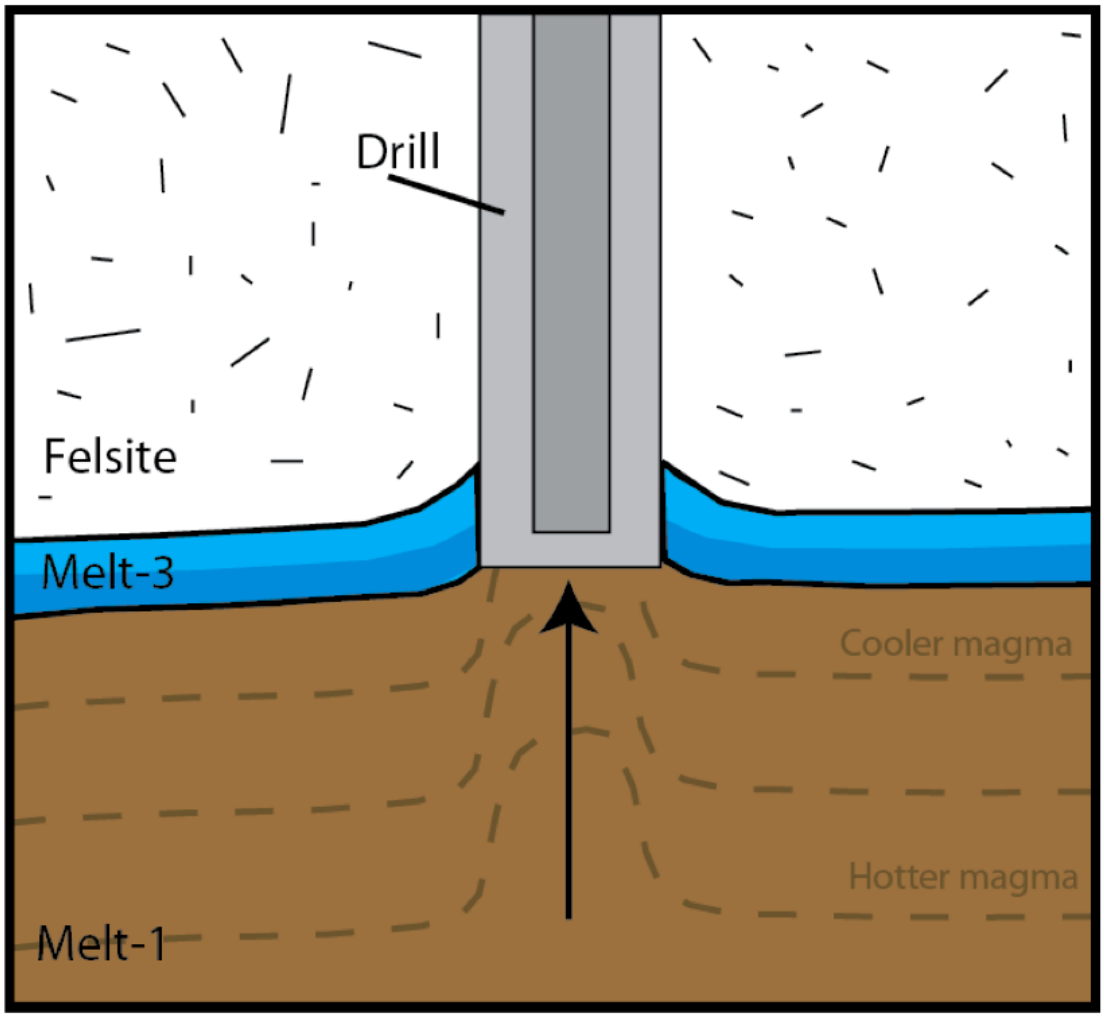

Figure 6.13: Schematic drawing of relatively hot magma rising in the later response to the intersection of the magma body.

6.8 Summary and future research directions

The major element results from this project have indicated that Melt-1a is caused by mixing of the magma body (similar to Melt-1 defined by Zierenberg et al. 2013) and the melt created in the surrounding felsite (similar to Melt-3 defined by Zierenberg et al. 2013). The bubbles in the first returned melt indicate that decompression induced by drilling was relatively localised due to the quick transition back to equilibrium (ie no bubble formation). The increase in temperature and corresponding decrease in viscosity between 16:45 to 20:39, indicates that a hotter magma (Melt-1b) was tapped.

Saturation pressures do not vary significantly suggesting that the melt did not come from very different depths. The low temperatures and viscosities and decompression magnitude described here explain why there was no eruption initiated with this event. The results of this project has indicated an on-going need to investigate further the magmatic response of sudden depressurisation, e.g. if failure of the valves in the drill hole allowed sudden depressurization of the melt. The following outlines potential future work that is required on the Krafla glass cuttings or studies of similar nature:

- Collecting and processing more data especially on the clear glass (boundary melt between the magma body and the surrounding felsite).
- Investigate whether the recovery time of the glass cuttings accurately represents that of the glass at the time of quenching. Due to the nature of the extraction process, it is hard to determine the true timing of glass quenching to the time at which it was recovered from the drill. This variable is important to constrain for similar studies as it can provide further insight into volatile migration during rapid depressurisation events.
- Investigation on how, or if, the previous two intersections of the magma by the drilling have affected the melt prior to the third intersection, it is subsequent to this intersection that the time-series of samples were collected.
- Further studies on whether different bottom hole assemblies (BHA) and size of the drill bit can affect how the intersected magma body responds to the intersection.
- More work on mapping the magmatic volatile distribution around bubbles. From this project the volatile distribution transects have shown both resorption and growth behaviour, however, there are no systematic trends with quench time and sample texture. This could be due to the limited data. A future study of volatile distribution around the bubbles would include looking at different bubble shapes (stretched and round bubbles). As performed in this project, FTIR can be used to measure volatile distribution study, but in addition, a secondary ion mass spectrometry (SIMS) calibrated backscatter scanning electron microscopy (BSEM) (Humphreys et al. 2008; McIntosh et al. 2014) could also be used to investigate H_2O distribution around bubbles.

- Investigation on what causes the doublet peak (CO_2) observed in the thin sample from SR-FTIR analysis (Chapter 4 section 4.2.4.1.1). Understanding how the doublet peak may or may not be related to measurement methods will provide a more accurate measurement of CO_2 and therefore, more precise estimates on the H_2O-CO_2 saturation pressure.

Chapter 7: Conclusion

The unexpected magma drilling of the IDDP-1 drill project has provided research opportunities for investigating subsurface magma and future geothermal studies. The aim of this project was to understand how the Krafla melt responded to being intercepted by the IDDP-1 drilling project. Major element data from EPMA analysis have shown that prior to drilling there was a complex melt boundary around the magma body which was a result of the melting and mixing of the surrounding felsite with the magma body. Magmatic volatile analyses from FTIR have shown that each melt type has a distinct volatile signature. Melt 1a (interpreted to represent the magma) is typically slightly higher in H_2O_t and H_2O_m, while Melt 1b (interpreted to represent the assimilation of the felsite and magma) is higher in CO_2. Volatiles in Melt 1b changes over time, with slight increases in the concentration of total H_2O, and a significant increase in CO_2 and OH/H_2O_m. High OH/H_2Om indicates that the melt has rapidly quickly. Bubbles in the first returned melt (Melt-1a) indicate that decompression induced by drilling was relatively slow and local. The increase in quench temperature and decrease of viscosity indicates that hotter magma (Melt-1b) either was progressively tapped or rose into the borehole. The low variation of H_2O-CO_2 saturation pressure over time suggests that either the drill did not penetrate far into the magma or the magma did not rise far into the borehole. Table 7.1 summarises the objectives and their answers for this project.

Table 7.1: Summary of project objectives and the associated answers

Objective	Answer	
1. Determine any changes in magmatic volatile concentration through time	Overall the H_2O_t concentration for the clear glass cuttings (mixing of the felsite and magma) are lower than those of the brown glass cuttings (magma). No significant changes in the concentration of H_2O_t over time. In all glass cutting the concentration of OH is higher than the concentration of H_2O_m. OH/H_2O_m of the brown glass will increases. CO_2 concentrations in the brown glass increases over time. No systematic trend in the clear glass.	**Chapter 5**
2. Map the distribution of H_2O species and CO_2 around bubbles in the samples IDDP-1 glass cuttings	Volatile distributions around bubbles have shown three different groups were observed. 1. No change in volatile concentration towards the bubble. Indicating the melt was in equilibrium 2. H_2O_t and OH concentrations decrease towards the bubble and H_2O_m increases over time. Indicating initial bubble growth then the melt experienced a decrease in temperature causing the bubble to resorb. 3. H_2O speciation and CO_2 concentration increase towards the bubble suggesting bubble resorption There were no systematic changes between time, glass textures and glass thickness. This indicates that the melt condition was heterogeneous	
3 Determine the magmatic degassing history of the Krafla magma body in response to a sudden loss of pressure as a result of interception by the drilling	Evidence of depressurisation in the earlier clear glass cuttings includes a high abundance of bubbles. However, this magmatic response was short lived. This suggest that depressurisation from the drilling only affected the magma for a short interval.	**Chapter 6**
4. Use the degassing history to asses quench timing and changes in magmatic viscosity.	The increase in OH/H_2O_m and CO_2 over time suggests that the quench temperature increased with time and viscosity decreased with time. This indicates hotter magma rising. The H_2O-CO_2 saturation pressure model also shows a small increase in pressure, suggesting that either the drill didn't penetrate deep within the magma or that the magma did not rise far.	
5. why didn't the Krafla magma erupt while it was being drilled	Overall, the effect from the drilling is small. The short depressurisation period suggest that the drill only afftected a small area of the magma and therefore depressuration of the melt was not great enough to induce an eruption.	

References

Anovitz LM, Cole DR, Fayek M 2008. Mechanisms of rhyolitic glass hydration below the glass transition. American Mineralogist 93(7): 1166-1178.

Baker DR, Alletti M 2012. Fluid saturation and volatile partitioning between melts and hydrous fluids in crustal magmatic systems: The contribution of experimental measurements and solubility models. Earth-Science Reviews 114(3): 298-324.

Bartholomew RF, Butler BL, Hoover HL, Wu CK 1980. Infrared spectra of a water-containing glass. Journal of the American Ceramic Society 63(9-10): 481-485.

Behrens H, Tamic N, Holtz F 2004. Determination of the molar absorption coefficient for the infrared absorption band of CO2 in rhyolitic glasses. American Mineralogist 89(2-3): 301-306.

Blank JG, Stolper EM, Carroll MR 1993. Solubilities of carbon dioxide and water in rhyolitic melt at 850°C and 750 bars. Earth and Planetary Science Letters 119(1): 27-36.

Bottinga Y, Weill DF 1972. The viscosity of magmatic silicate liquids; a model calculation. American Journal of Science 272(5): 438-475.

Carey RJ, Manga M, Degruyter W, Gonnermann H, Swanson D, Houghton B, Orr T, Patrick M 2013. Convection in a volcanic conduit recorded by bubbles. Geology 41(4): 395-398.

Della Ventura G, Bellatreccia F, Marcelli A, Cestelli Guidi M, Piccinini M, Cavallo A, Piochi M 2010. Application of micro-FTIR imaging in the Earth sciences. Analytical and Bioanalytical Chemistry 397(6): 2039-2049.

Devereux S 2012. Drilling technology in nontechnical language. 2nd;2; ed. Tulsa, Okla, PennWell Corp.

Dingwell DB 2006. Transport Properties of Magmas: Diffusion and Rheology. Elements 2(5): 281-286.

Dingwell DB, Webb SL 1989. Structural relaxation in silicate melts and non-Newtonian melt rheology in geologic processes. Physics and Chemistry of Minerals 16(5): 508-516.

DiPippo R 2008. Geothermal power plants: principles, applications, case studies and environmental impact. 2nd;2; ed. Oxford;Boston;, Butterworth-Heinemann.

Dixon JE, Stolper EM, Holloway JR 1995. An experimental study of water and carbon dioxide solubilities in mid ocean ridge basaltic liquids .1. Calibration and solubility models. JOURNAL OF PETROLOGY 36(6): 1607-1631.

Dowdle WL, Cobb WM 1975. Static formation temperature from well logs-an empirical method. JPT, Journal of Petroleum Technology 27: 1326-1330.

Einarsson P 1978. S-wave shadows in the Krafla Caldera in NE-Iceland, evidence for a magma chamber in the crust. Bulletin Volcanologique 41(3): 187-195.

Elders WA, Fridleifsson GÓ, Zierenberg RA, Pope EC, Mortensen AK, Gudmundsson Á, Lowenstern JB, Marks NE, Owens L, Bird DK and others 2011. Origin of a rhyolite that intruded a geothermal well while drilling at the Krafla volcano, Iceland. Geology 39(3): 231-234.

Elders WA, Frioleifsson GO, Pálsson B 2014. Iceland deep drilling project: The first well, IDDP-1, drilled into magma. Geothermics 49: 1.

Fine F, Stolper EM 1985. The speciation of carbon dioxide in sodium aluminosilicate glasses. Contrib Mineral. Petrol 91:105-121

Fridleifsson GO, Armannsson H, Gudmundsson A, Arnason K, Mortensen AK, B, Einarsson GM 2014. Site selection for the well IDDP-1 at Krafla. GEOTHERMICS 49: 9-15.

Fridleifsson GO, Elders WA, Albertsson A 2014. The concept of the Iceland deep drilling project. GEOTHERMICS 49: 2-8.

Gardner JE, Hilton M, Carroll MR 1999. Experimental constraints on degassing of magma: isothermal bubble growth during continuous decompression from high pressure. Earth and Planetary Science Letters 168(1-2): 201-218.

Giordano D, Nichols ARL, Dingwell DB 2005. Glass transition temperatures of natural hydrous melts: a relationship with shear viscosity and implications for the welding process. Journal of Volcanology and Geothermal Research 142(1): 105-118.

Glassley WE 2015. Geothermal energy: renewable energy and the environment. Second ed. Boca Raton, CRC Press/Taylor & Francis.

Guðmundsson A´ (1983) The geology of the Krafla Suðurhl´ıðar field, in ravens congregation on the status of the Krafla geothermal power station, 2–3 March 1983, Krafla power station, Akureyri, Iceland, pp 77–85 (in Icelandic)

Hess KU, Dingwell DD 1996. Viscosities of hydrous leucogranitic melts: A non-Arrhenian model. American Mineralogist 81(9): 1297-1300.

Hólmgeirsson S, Guðmundsson Á, Pálsson B, Bóasson HA, Ingason K, Þórhallsson S 2010. Drilling operations of he first Iceland deep drilling well (IDDP). In: Proceedings of the world geothermal congress. Bali Indonesia, 25–29 April 2010, pp 1–10

Huenges E 2010. Geothermal energy systems: exploration, development, and utilization. Weinheim, Wiley-VCH.

Hui H, Zhang Y, Xu Z, Behrens H 2008. Pressure dependence of the speciation of dissolved water in rhyolitic melts. Geochimica et Cosmochimica Acta 72(13): 3229-3240.

Humphreys MCS, Menand T, Blundy JD, Klimm K 2008. Magma ascent rates in explosive eruptions: Constraints from H2O diffusion in melt inclusions. Earth and Planetary Science Letters 270(1-2): 25-40.

Ihinger PD, Hervig RL, McMillan PF, Zhang Y, Stolper EM 1994. Analytical methods for volatiles in glasses. Reviews in Mineralogy and Geochemistry 30, 67-121.

Ihinger PD, Zhang Y, Stolper EM 1999. The speciation of dissolved water in rhyolitic melt. Geochimica et Cosmochimica Acta 63(21): 3567-3578.

Jarosewich E, Nelen JA, Norberg JA (1980) Reference samples for electron microprobe analysis. Geostandards Newsletter 4:43-47.

Jonasson K 1994. Rhyolite volcanism in the Krafla Central volcano, northeast Iceland. Bullentin of Volcanology 56(6-7): 516-528.

Kennedy BM, Holohan EP, Stix J, Gravley DM, Davidson JRJ, Cole JW 2018. Magma plumbing beneath collapse caldera volcanic systems. Earth-Science Reviews 177: 404-424.

Lange RA 1994. The effect of H2O, CO2 and F on the density and viscosity of silicate melts. Chantilly, Mineralogical Soc. Pp. 331-369.

Lange RA 1997. A revised model for the density and thermal expansivity of K2O-Na2O-CaO-MgO-Al2O3-SiO2 liquids from 700 to 1900 K: extension to crustal magmatic temperatures. Contributions to Mineralogy and Petrology 130(1): 1-11.

Lange RA, Carmichael ISE 1987. Densities of Na2O-K2O-MgO-MgO-FeO-Fe2O3-Al3O3-TiO2-SiO2 liquids: New measurements and derived partial molar properties. Geochimica et Cosmochimica Acta 51(11): 2931-2946.

Le Bas MJ, Streckeisen AL 1991. The IUGS systematics of igneous rocks. Journal of the Geological Society 148(5): 825-833.

Liu Y, Zhang Y, Behrens H 2005. Solubility of H2O in rhyolitic melts at low pressures and a new empirical model for mixed H2O-CO2 solubility in rhyolitic melts. Journal of Volcanology and Geothermal Research 143(1-3): 219-235.

Lowenstern JB 2001. Carbon dioxide in magmas and implications for hydrothermal systems. Mineralium Deposita 36(6): 490-502.

Mangan, M. & Sisson, T., 2000. Delayed , disequilibrium degassing in rhyolite magma : decompression experiments and implications for explosive volcanism. *Earth and Planetary Science Letters*, 183, pp.441-455.

McIntosh IM, Llewellin EW, Humphreys MCS, Nichols ARL, Burgisser A, Schipper CI, Larsen JF 2014. Distribution of dissolved water in magmatic glass records growth and resorption of bubbles. Earth and Planetary Science Letters 401: 1-11.

McIntosh IM, Nichols ARL, Tani K, Llewellin EW 2017. Accounting for the species-dependence of the 3500 cm−1 H2Ot infrared molar absorptivity coefficient: Implications for hydrated volcanic glasses. American Mineralogist 102(8): 1677-1689.

Miller LM, Smith RJ 2005. Synchrotrons versus globars, point-detectors versus focal plane arrays: Selecting the best source and detector for specific infrared microspectroscopy and imaging applications. Vibrational Spectroscopy 38(1): 237-240.

Miwa T, Toramaru A 2013. Conduit process in vulcanian eruptions at Sakurajima volcano, Japan: Inference from comparison of volcanic ash with pressure wave and seismic data. Bulletin of Volcanology 75(1): 1-13.

Morizet Y, Nichols ARL, Kohn SC, Brooker RA, Dingwell DB 2007. The influence of H2O and CO2 on the glass transition temperature: insights into the effects of volatiles on magma viscosity. European Journal of Mineralogy 19(5): 657-669.

Morizet Y, Paris M, Sifre D, Di Carlo I, Ory S, Gaillard F 2017. Towards the reconciliation of viscosity change and CO 2 -induced polymerization in silicate melts. Chemical Geology 458: 38-47.

Mortensen AK, Gro¨ nvold K, Gudmundsson A´ , Steingr´ımsson BS, Egilson Þ (2010) Quenched silicic glass from well K-39 in Krafla, North-Eastern Iceland. In: Proceedings of the world geothermal congress 2010, Bali, Indonesia, 25–29 April 2010, Paper 1284, pp 1–6

Mortensen AK, Egilson P, Gautason B, Arnadottir S, Gudmundsson A 2014. Stratigraphy, alteration mineralogy, permeability and temperature conditions of well IDDP-1, Krafla, NE-Iceland. GEOTHERMICS 49: 31-41.

Mourtada-Bonnefoi, C.C. & Laporte, D., 2004. Kinetics of bubble nucleation in a rhyolitic melt: an experimental study of the effect of ascent rate. *Earth and Planetary Science Letters*, 218(3-4), pp.521-537.

Nakamoto K 1978. Infrared and Raman spectra of inorganic and coordination compounds. 6th ed. Oxford;Hoboken, N.J;, Wiley.

Newman S, Lowenstern JB 2002. VOLATILECALC: A silicate melt-H2O-CO2 solution model written in Visual Basic for excel. Computers and Geosciences 28(5): 597-604.

Newman S, Stolper EM, Epstein S 1986. Measurement of water in rhyolitic glasses; calibration of an infrared spectroscopic technique. American Mineralogist 71(11-12): 1527-1541.

Nichols ARL, Wysoczanski RJ 2007. Using micro-FTIR spectroscopy to measure volatile contents in small and unexposed inclusions hosted in olivine crystals. Chemical Geology 242(3): 371-384.

Nishikida K, Nishio E, Hannah RW 1996. Selected Applications of Modern FT-IR Techniques. Gordon and Breach. 200 pp.

Nowak M, Behrens H 2001. Water in rhyolitic magmas: getting a grip on a slippery problem. Earth and Planetary Science Letters 184(2): 515-522.

Ochs Iii FA, Lange RA 1997. The partial molar volume, thermal expansivity, and compressibility of H2O in NaAlSi3O8 liquid: new measurements and an internally consistent model. Contributions to Mineralogy and Petrology 129(2): 155-165.

Pálsson B, Holmgeirsson S, Gudmundsson A, Boasson HA, Ingason K, Sverrisson H, Thorhallsson S 2014. Drilling of the well IDDP-1. GEOTHERMICS 49: 23-30.

Potts PJ, Mineralogical S 1995. Microprobe techniques in the earth sciences. 1st ed. London, Chapman & Hall.

Proussevitch AA, Sahagian DL 1996. Dynamics of coupled diffusive and decompressive bubble growth in magmatic systems. JOURNAL OF GEOPHYSICAL RESEARCH-SOLID EARTH 101(B8): 17447-17455.

Reed SJB 2005. Electron microprobe analysis and scanning electron microscopy in geology. 2nd ed. Cambridge, Cambridge University Press.

Rust AC, Cashman KV, Wallace PJ 2004. Magma degassing buffered by vapor flow through brecciated conduit margins. GEOLOGY 32(4): 349-352.

Sæmundsson K (1991) Geology of the Krafla system. In: Gardarsson A, Einarsson A´ (eds) Na´ttu´ra My´vatns Hid´Islenska Na´ttu´ruf- raedife´lag, Raykjav´ık, pp 25–95 (in Icelandic)

Saubin E, Kennedy BM, Tuffen H, Villeneuve M, Watson T, Nichols ARL, Schipper I, Cole JW, Mortensen A, Zierenberg R 2017. Reaction of rhyolitic magma to its interception by the IDDP-1 well, Krafla, 2009. American Geophysical Union conference 2017, Abstract

Schoize H 1960. Zur Frage der Unterscheidung zwischen H2O-Molekeln und OH-Gruppen in Gläsern und Mineralen. Die Naturwissenschaften 47(10): 226-227.

Shaw HR 1974. Diffusion of H2O in granitic liquids, I: experimental data; II: mass transfer in magma chambers. In A. W. Hofmann et al., eds. *Geochemical Transport and Kinetics*. Washington: Carnegie Institute of Washington, pp. 139-170.

Silver LA, Ihinger PD, Stolper E 1990. The influence of bulk composition on the speciation of water in silicate glasses. Contributions to Mineralogy and Petrology 104(2): 142-162.

Sparks RSJ 1978. The dynamics of bubble formation and growth in magmas: A review and analysis. Journal of Volcanology and Geothermal Research 3(1): 1-37.

Stevenson RJ, Briggs RM, Hodder APW 1994. Physical volcanology and emplacement history of the Ben-Lomind rhyolite lava flow, Taupo Volcanic center, New Zealand. New Zealand Journal of Geology and Geophysics 37(3): 345-358.

Stolper E 1982. Water in silicate glasses: An infrared spectroscopic study. Contributions to Mineralogy and Petrology 81(1): 1-17.

Stolper E 1989. Temperature dependence of the speciation of water in rhyolitic melts and glasses. American Mineralogist 74(11-12): 1247-1257.

Sun WD, Binns RA, Fan AC, Kamenetsky VS, Wysoczanski R, Wei GJ, Hu YH, Arculus RJ 2007. Chlorine in submarine volcanic glasses from the eastern manus basin. Geochimica et Cosmochimica Acta 71(6): 1542-1552.

Tamic N, Behrens H, Holtz F 2001. The solubility of H2O and CO2 in rhyolitic melts in equilibrium with a mixed CO2-H2O fluid phase. Chemical Geology 174(1-3): 333-347.

Teplow W, Marsh B, Hulen J, Spielman P, Kaleikini M, Fitch D, Rickard W 2008. Dacite melt at the Puna Geothermal Venture Wellfield, big island of Hawaii. Pp. 876-881.

Trewick L, Tuffen H, Owen J, Kennedy B, Eichelberger J, Zierenberg R 2016. Vesiculation of rhyolite magma in the ICCP-1 borehole at Krafla, Iceland. Geophysical Research Abstracts, 18.

von Aulock FW, Kennedy BM, Schipper CI, Castro JM, Martin DE, Oze C, Watkins JM, Wallace PJ, Puskar L, Begue F and others 2014. Advances in Fourier transform infrared spectroscopy of natural glasses: From sample preparation to data analysis. LITHOS 206(1): 52-64.

Watkins JM, Manga M, DePaolo DJ 2012. Bubble geobarometry: A record of pressure changes, degassing, and regassing at Mono Craters, California. Geology 40(8): 699-702.

Wysoczanski R, Tani K 2006. Spectroscopic FTIR imaging of water species in silicic volcanic glasses and melt inclusions: An example from the Izu-Bonin arc. Journal of Volcanology and Geothermal Research 156(3): 302-314.

Yoshimura S, Nakamura M 2008. Diffusive dehydration and bubble resorption during open-system degassing of rhyolitic melts. Journal of Volcanology and Geothermal Research 178(1): 72-80.

Yoshimura S, Nakamura M 2010. Chemically driven growth and resorption of bubbles in a multivolatile magmatic system. Chemical Geology 276(1): 18-28.

Zhang, Y. & Ni, H. 2010. Diffusion of H, C, and O Components in Silicate Melts Youxue Zhang & D. J. Cherniak, eds. *Reviews in Mineralogy and Geochemistry*, 72(1), pp.171-225.

Zhang Y, Stolper EM 1991. Water diffusion in a basaltic melt. Nature 351(6324): 306-309.

Zhang, Youxue et al. 2007. SILICATE MELT PROPERTIES AND VOLCANIC ERUPTIONS. *Reviews of Geophysics*, (2006), pp.1-27.

Zierenberg RA, Schiffman P, Barfod GH, Lesher CE, Marks NE, Lowenstern JB, Mortensen AK, Pope EC, Bird DK, Reed MH and others 2013. Composition and origin of rhyolite melt intersected by drilling in the Krafla geothermal field, Iceland. Contributions to Mineralogy and Petrology 165(2): 327-347.

Appendix 1: Standards testing for EPMA

Table A1.1: Table of expected values for VG-568 standard and the obtained values from the EPMA for this project.

VG-568	Expected value	STDEV	n	EPMA value	STDEV	n
Na_2O	3.74	0.34	50	3.36	0.12	10
MgO	0.04	0.02	50	0.03	0.01	10
Al_2O_3	12.14	0.17	50	12.28	0.1	10
SiO_2	76.77	0.42	50	77.35	0.2	10
K_2O	4.97	0.09	50	4.84	0.13	10
CaO	0.42	0.03	50	0.46	0.02	10
TiO_2	0.08	0.05	50	0.06	0.01	10
MnO	0.03	0.02	50	0.02	0.02	10
FeO	1.11	0.09	50	1.16	0.07	10

Table A1.2: Table of expected values for VGA-99 standard and the obtained values from the EPMA for this project.

VG-A99	Expected value	STDEV	n	EPMA value	STDEV	n
Na_2O	2.70	0.04	13	2.45	0.07	10
MgO	5.10	0.08	13	4.92	0.07	10
Al_2O_3	12.49	0.13	13	12.45	0.09	10
SiO_2	51.00	0.27	13	51.01	0.1	10
K_2O	0.86	0.05	13	0.85	0.02	10
CaO	9.21	0.11	13	9.1	0.12	10
TiO_2	4.10	0.03	13	3.99	0.03	10
MnO	0.20	0.02	13	0.2	0.02	10
FeO	13.24	0.1	13	13.56	0.15	10

Reference:

Jochum KP, Nohl U. Herwig K, Lammel E, Stoll B, Hofmann AW 2005. GeoRem: A new geochemical database for reference materials and isotopic standards. Geostandards and Geoanalytical research 29(3): 333-338.

Appendix 2: Volatile distribution transects

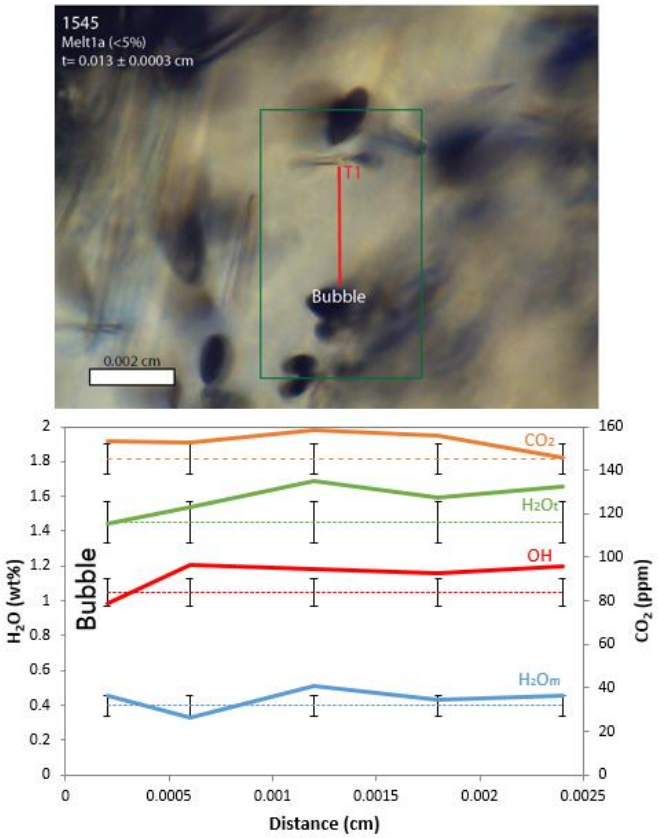

Figure A2.2: H_2O and CO_2 transects in sample 1545

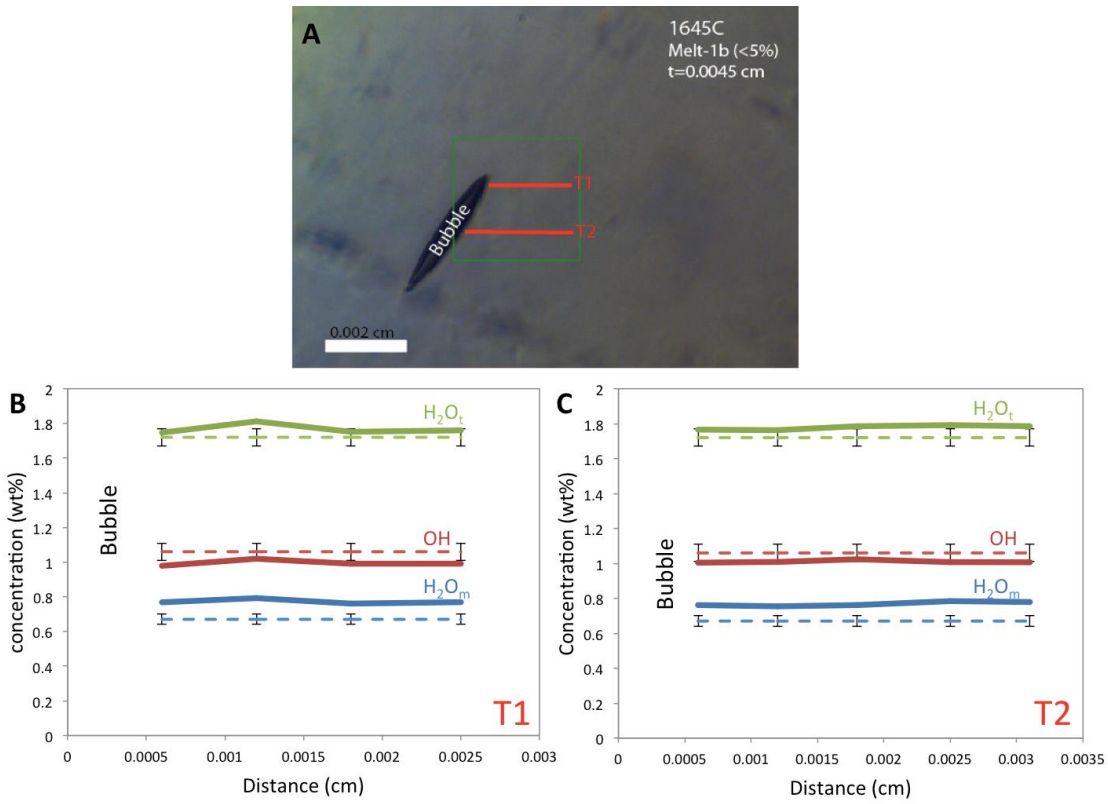

Figure A2.2: H_2O transects in sample 16:45C

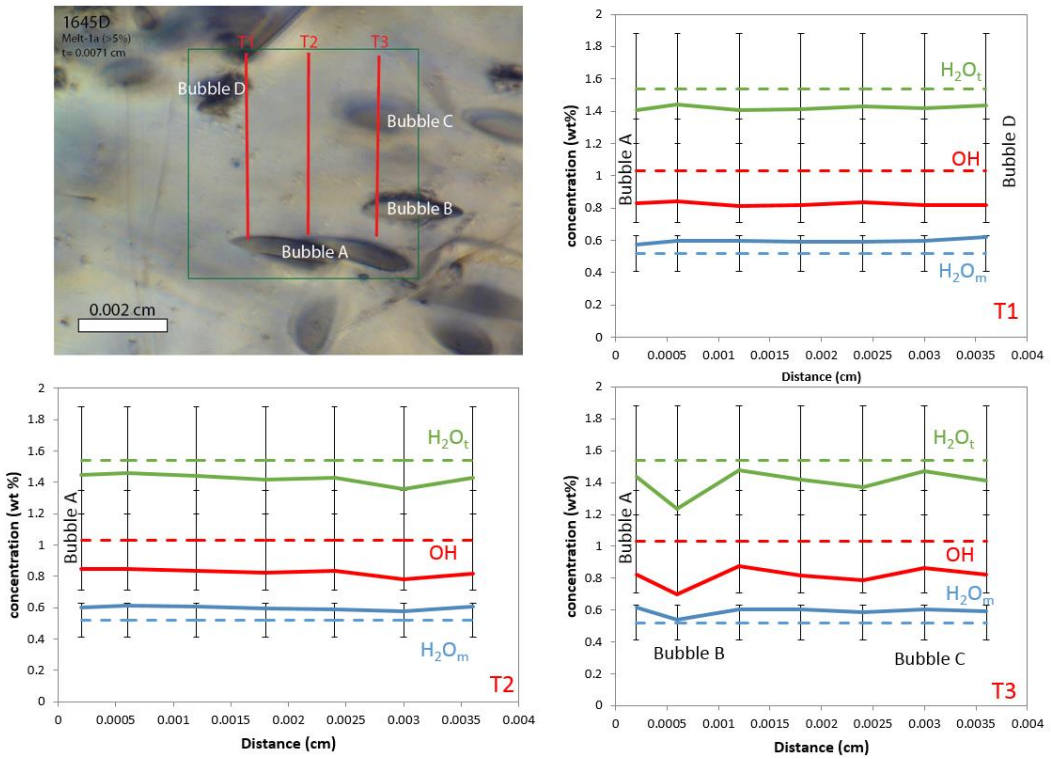

Figure A2.3: H_2O transects in sample 1645D

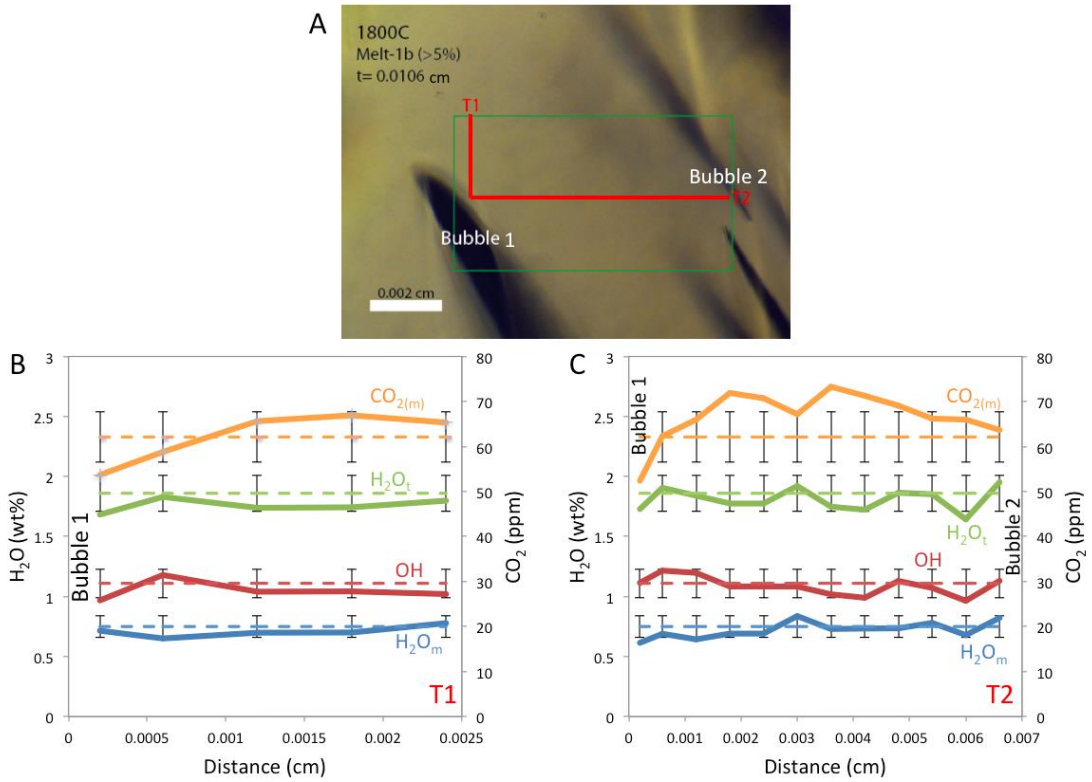

Figure A2.4: H_2O and CO_2 transects in sample 1800C

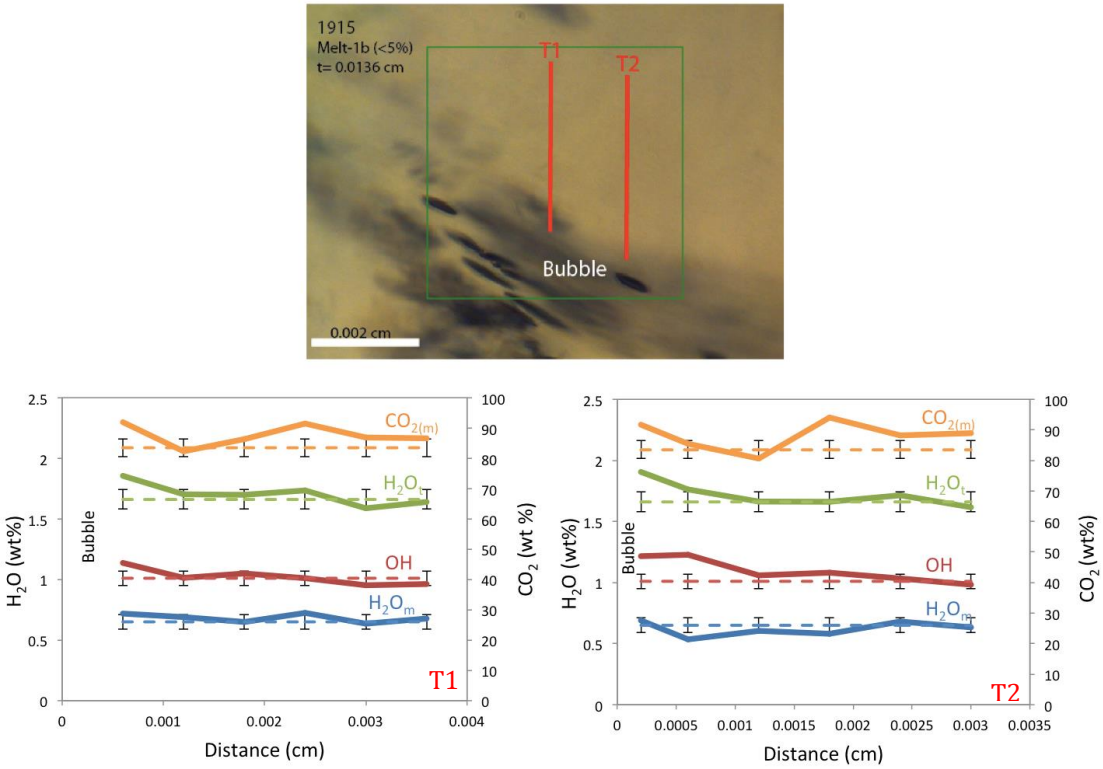

Figure A2.5: H_2O and CO_2 transects in sample 1915

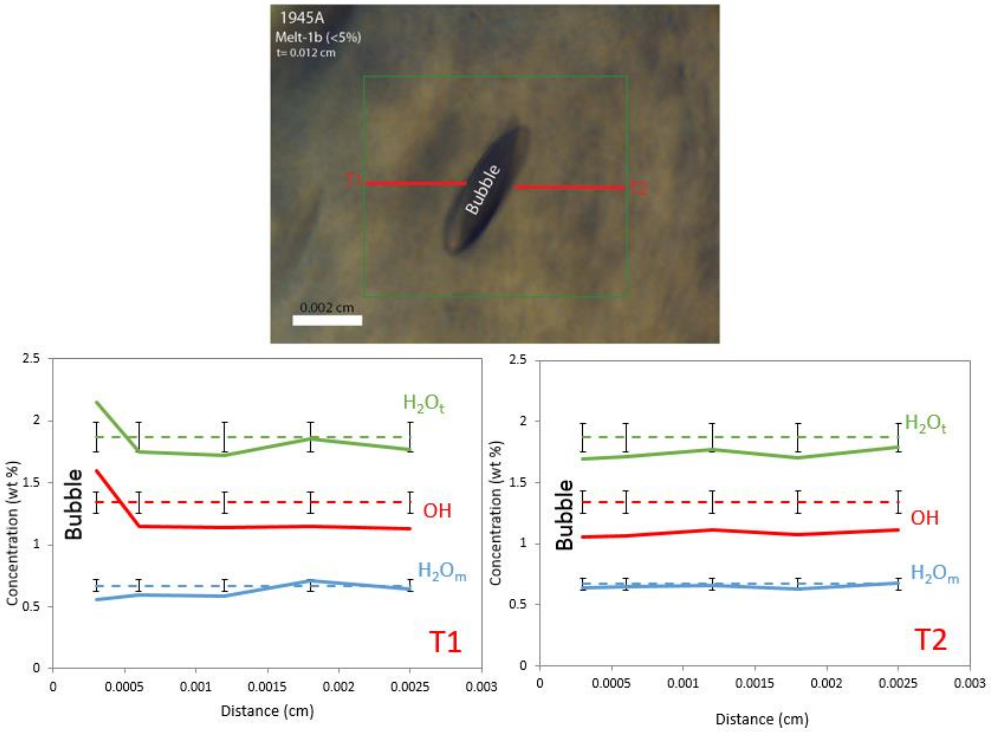

Figure A2.6: H_2O transects in sample 1945A